Department of Physics and Astronomy

University of Heidelberg

Master thesis

in Physics

submitted by

Svenja Reith

born in Gelnhausen

2014

Spatio-temporal slope measurement
of short wind waves
under the influence of surface films
at the Heidelberg Aeolotron

This Master thesis has been carried out by Svenja Reith at the

Institute of Environmental Physics in Heidelberg

under the supervision of

Prof. Dr. Bernd Jähne

Abstract:

A novel, high resolution Imaging Slope Gauge (ISG) at the Heidelberg Aeolotron is presented. The instrument allows measurements of the two-dimensional slope of short wind-driven water waves at unprecedented temporal and spatial resolution. Wave number spectra are measured up to k = 13 000 rad/m with a temporal resolution of more than 1500 Hz. The high sampling frequency eliminates aliasing up to wave numbers of about k = 2660 rad/m. A new non-linear calibration and data processing work flow has been implemented to convert raw camera images into wave slope in the range of ±0.96. The average statistical measurement error is estimated to be $\Delta s_{\mathrm{rms}} = 0.018$, a significant improvement compared to previous Color Imaging Slope Gauge setups.

Spectrally resolved measurements of the influence of various surface-active materials (surfactants) on small-scale waves are reported. The wave damping effects of different substances are analyzed. It is shown that, except for low wind speeds, gas transfer velocities across the air-sea boundary layer can be parametrized with the mean square slope of the waves, independent of the specific type of surfactant that is used.

Zusammenfassung:

Ein neues hochauflösendes bildgebendes Messinstrument (Imaging Slope Gauge) am Heidelberger Aeolotron wird beschrieben. Das Instrument ermöglicht Messungen der Neigung von kurzen winderzeugten Wasserwellen mit bisher unerreichter zeitlicher und räumlicher Auflösung. Wellenzahlspektren werden bis zu Wellenzahlen von k = 13 000 rad/m und mit einer zeitlichen Auflösung von mehr als 1500 Hz gemessen. Die hohe zeitliche Aufnahmefrequenz verhindert Aliasing bis hin zu Wellenzahlen von k = 2660 rad/m. Eine neue nichtlineare Kalibrierungs- und Auswerteroutine wurde implementiert um Kamera-Rohbilder in Wellenneigung im Bereich ±0.96 umzurechnen. Der mittlere statistische Messfehler beträgt $\Delta s_{\mathrm{rms}} = 0.018$, eine deutliche Verbesserung gegenüber älteren Color Imaging Slope Gauge Aufbauten.

Spektral aufgelöste Messungen des Einflusses von unterschiedlichen oberflächenaktiven Substanzen (Surfactants) auf kleinskalige Wellen werden präsentiert. Die Wellendämpfungseffekte verschiedener oberflächenaktiver Substanzen werden analysiert. Es zeigt sich, dass die Gasaustausch-Transfergeschwindigkeiten durch die Grenzschicht zwischen Luft und Wasser durch oberflächenaktive Substanzen (außer für sehr niedrige Windgeschwindigkeiten) durch die mittlere quadratische Neigung parametrisiert werden können, unabhängig von der verwendeten oberflächenaktiven Substanz.

Contents

I Background 9

1

Introduction

The Ocean, Air-Sea Gas Exchange, and the Importance of Waves

Not only has the ocean exerted a strong fascination on people for ages but it is also a giant reservoir with major relevance as an ecosystem as well as for climatic processes. It is important to examine the processes of *heat, gas and momentum exchange* between the ocean and the atmosphere in order to understand the climate system as well as climate change. Furthermore, at least heat and momentum exchange contribute to the driving forces of large scale oceanic circulation and influence temperature and humidity in the atmosphere and thus modify the atmospheric circulation and the hydrological cycle [IPCC, 2013].

Climate change is a topic of special concern for humanity. Regarding this, the ocean is of particular importance as a net sink for anthropogenic carbon dioxide (CO_2) emissions. The oceanic reservoir of DIC (dissolved inorganic carbon) is more than 50 times higher that the atmospheric one (see Sabine et al. [2004] and Figure 1.1). At the same time, the oceans currently take up CO_2 at a rate of about $7\,\mathrm{Gt\ CO_2\ yr^{-1}}$ ($\hat{=}$ $2\,\mathrm{Gt\ C\ yr^{-1}}$; Caldeira and Akai [2013]).

Regional air-sea fluxes of CO_2 are largely unknown [Donelan and Wanninkhof, 2002]. Wanninkhof and McGillis [1999] proposed parametrizations of the gas exchange velocity with wind speed and, with that, found a yearly carbon intake of the ocean between 1.4 and $2.2\,\mathrm{Gt\ C\ yr^{-1}}$. Many other parametrizations linking transfer velocities to wind speed have evolved over the past years which state different functional relations, including piecewise linear [Liss and Merlivat, 1986], quadratic [Wanninkhof, 1992; Ho et al., 2006; Takahashi et al., 2009] and other polynomial [Nightingale et al., 2000] relations. The model of Wanninkhof and McGillis [1999] states a cubic relation.

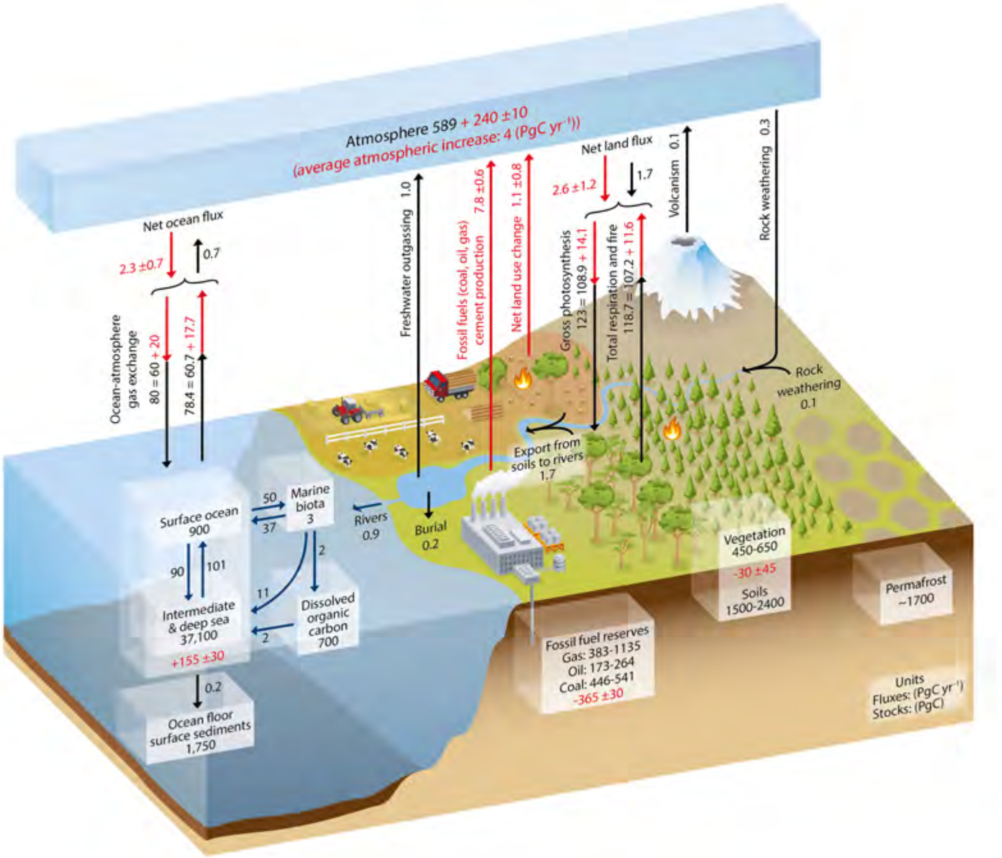

Figure 1.1.: The global carbon reservoirs and fluxes. Image taken from Ciais et al. [2013].

Yet the wind does not influence gas transfer velocities directly. There is evidence from laboratory as well as field studies that (wind-induced) waves, especially those with wavelengths between millimetres and decimetres, have a major impact on gas transfer velocities [Jähne, 1985; Frew et al., 2004]. The largest resistance to air-sea gas transfer of sparingly soluble gases like CO_2 lies in the *aqueous mass boundary layer* at the air-water interface where turbulence processes are suppressed [Jähne and Haußecker, 1998]. *Semi-empirical parametrizations* linking the gas transfer velocity with wind speed, such as the one proposed by Liss and Merlivat [1986] and Wanninkhof and McGillis [1999], are widely used. The reason for this are the difficulties of directly measuring *near-surface turbulence* which is attributed to be the quantity which controls gas transfer velocities [Lamont and Scott, 1970; Coantic, 1986]. The most important processes influencing near-surface turbulence and thus transfer velocities are *microscale wave breaking*[1] [Banner and Phillips, 1974] and

---

[1] The term *microscale wave breaking* describes the breaking of steep wind-driven gravity waves with decimeter wavelengths without entraining air [Zappa et al., 2001].

Langmuir circulations[2] [Melville et al., 1998; Frew et al., 2004; Tsai et al., 2013]. It was shown by Zappa et al. [2004] that at moderate wind speeds, microscale wave breaking is the cause for up to 75 % of the overall gas transfer. Langmuir circulations appear to be important for gas exchange processes especially during initial wave growth [Veron and Melville, 2001a]. Furthermore, the presence of *surface active substances (surfactants)* leads to lower transfer velocities and gas exchange rates [Broecker et al., 1978; Jähne et al., 1987; Frew et al., 2004] due to their damping effect on waves [Alpers, 1989; Bock and Mann, 1989].

In general, a physics based parametrization of gas transfer velocities is desirable. This has led to the search for alternative parametrizations of gas exchange processes. The parameter *mean square slope*[3] of the water surface σ^2 has proven to be a promising candidate [Jähne et al., 1984b; Bock et al., 1999; Frew et al., 2007; Kiefhaber, 2014]. Alternative candidates which have been proposed are the turbulent kinetic energy (TKE) dissipation [Lamont and Scott, 1970; Kitaigorodskii, 1984; Zappa et al., 2007] and the divergence of the flow field at the surface [McKenna and McGillis, 2004; Banerjee, 2007; Asher et al., 2012].

This thesis focuses on mean square slope. It has been shown to correlate well with microscale breaking effects [Zappa et al., 2004] and gas transfer velocities. Several measurements of mean square slope have been conducted in the field [Cox and Munk, 1954b; Zappa et al., 2012] and in the laboratory [Wu, 1971; Jähne et al., 1984a; Jähne and Riemer, 1990; Hwang, 1997; Bock et al., 1999]. The common objective of the studies presented here is to achieve a better understanding of the physical foundations of the link between gas transfer and water waves. As one step towards this goal, laboratory measurements of water wave surface slope will be presented in this thesis.

Wave Slope Imaging Techniques

A variety of imaging techniques for measuring water wave slopes has evolved over the past decades. Two basic groups of techniques can be distinguished. The first one is the group of *height measurements* which includes *stereo methods* with two cameras [Laas, 1905; Kohlschütter, 1906; Laas, 1906, 1921; Schuhmacher, 1939; Waas and Jähne, 1992; Hilsenstein, 2004]. The second group comprises *optical slope measurement methods* which are based on the *reflection* or the *refraction* of light at the inclined air-water interface.

The first successful application of reflection-based methods was made by Cox and Munk [1954b] who measured water surface slope from photographs of sun glitter. Stilwell [1969] made qualitative measurements of water wave surface slopes on the open ocean using the diffuse light scattered in the sky as a light source with infinite

---

[2] *Small-scale Langmuir circulations* occur due to nonlinear interactions between waves and the shear current [McWilliams et al., 1997; Veron and Melville, 2001b; Teixeira and Belcher, 2002] and appear as helices whose axis is almost aligned with the wind direction [Caulliez, 1998].

[3] Mean square slope is a measure for the surface roughness of the wave field.

extent. Other methods include the Reflective Stereo Slope Gauge (RSSG) [Schooley, 1954; Kiefhaber, 2010]. Recently, polarimetric slope imaging was developed by Zappa et al. [2008] which allows for the measurement of water wave surface slope from the polarisation of the reflected light.

Refraction-based methods reach back to the measurements of Cox [1958]. Another development is the Laser Slope Gauge (LSG) [Hughes et al., 1977]. Modern methods use CCD or CMOS cameras to measure slopes in two dimensions. These include the imaging slope gauge (ISG; Keller and Gotwols [1983]; Jähne and Waas [1989]; Jähne and Riemer [1990]) and its successor, the color imaging slope gauge (CISG; Zhang and Cox [1994]; Balschbach [2000]).

Objectives of this Thesis

Although a lot of progress has been made concerning water wave slope measurements and imaging techniques some open questions remain. These include the influence of salinity and chemical and biological surfactants on the wave field as well as the interactions between the wind and the wave field, and the processes of wind input and energy dissipation. Recently, an increasing amount of studies sets the focus on the connection between surfactants and air-sea interaction processes [Gade et al., 2006]. The present study makes an effort to shed light on the question which differences in the wave field are observable depending on surfactant type and concentration. For this purpose an imaging slope gauge (ISG) was used.

The objective of this study was to put the ISG in operation at a wind/wave facility, the Heidelberg Aeolotron and to conduct some first water wave slope measurements with different kinds of natural and synthetic surfactants. This includes the improvement of the ISG setup and evaluation method at the Heidelberg Aeolotron as well as its application for spatiotemporal measurements of the properties of water waves. For calibration of the instrument, a method based on a lens float calibration target [Balschbach, 2000; Rocholz, 2008] has been adapted.

From the technical side of view it was possible to increase the brightness of the ISG illumination source which allows for measurements with smaller aperture and hence with improved image quality in terms of depth of field. Using the new high speed camera which is installed as part of the ISG setup it is now possible to record both components of water surface slope with an effective frame rate of more than 1500 Hz. In contrast to the CISG previously used by Rocholz [2008] the combination of these technical improvements now allows for not only measuring the 2D wave number vector, but also for the measurement of the frequencies of waves with wave numbers up to 2660 rad/m[4] without aliasing effects.

Within the scope of this thesis, experiments with different types of surfactants have been conducted and evaluated. ISG data was recorded during a measurement

---

[4] Note that according to Apel [1994] waves with wave numbers larger than 6000 rad/m do not occur at all.

campaign in May 2013 where, among others, active thermography measurements were conducted and transfer velocities for N_2O and friction velocities were determined. The evaluation of the ISG data comprises a spectral description of the wave field using omnidirectional saturation spectra $B(k)$ as well as a description with statistical parameters. For that, the dependency of mean square slope on wind speed and surfactant concentration is analysed, especially for nature-like surfactants. Furthermore, it is examined whether mean square slope is a better parameter for gas transfer velocities in the presence of waves than friction velocity is.

For November 2014, a measurement campaign with sea water and natural surfactants is planned at the Aeolotron. This work serves as a preparatory study for the planned campaign.

Part I.

Background

2
Theory of water waves

A detailed description of the basic equations of water wave physics starting at the continuity equation and the Navier-Stokes equation is omitted here as it is given in many textbooks on fluid mechanics such as Kundu [2008]. Instead, this chapter will present a short classification of water waves, briefly describe the generation of waves by wind, and give a spectral description of the wave field. In the final section, the influence of surface films on surface water waves is summarized.

2.1 Gravity waves and Capillary waves

Water waves can be classified according to their restoring forces. *Gravity waves* are displacements of the water surface which are restored by gravity. The term gravity wave describes waves with wavelengths between centimeters and several hundred meters and is applied to waves at the water surface or internal waves[1] alike. In contrast, *capillary waves* are restored by surface tension and thus restricted to domains of high curvature, that is very short wavelengths. *Gravity-capillary waves* populate the transition region in between gravity waves and capillary waves.

For linear gravity-capillary waves with wave number k, the surface elevation $\eta(\vec{x}, t)$ is

$$\eta(\vec{x}, t)_{\text{grav}} = a \cos\theta(\vec{x}, t) \tag{2.1}$$

---

[1] *Internal water waves* are waves within the water body which are for example observable from density fluctuations.

and the corresponding phase speed c is given by

$$c_{\text{grav}} = \sqrt{\frac{g}{k} + \frac{\sigma k}{\rho}} \tag{2.2}$$

with the surface tension coefficient σ and the density ρ of the fluid.

Linear capillary waves are described by

$$\eta(x)_{\text{cap}} = h \sin(2\pi \cdot \frac{x}{\lambda}). \tag{2.3}$$

Their phase speed is

$$c_{\text{cap}} = \sqrt{\frac{2\pi \cdot \sigma}{\rho \cdot \lambda}}. \tag{2.4}$$

The instantaneous height profile η of pure nonlinear gravity waves of wavelength λ and wave number k has been approximated by Stokes [1849]:

$$\eta_{\text{stokes}} \approx -a \cos(kx) + \frac{1}{2} k a^2 \cos(2kx) - \frac{3}{8} k^2 a^2 \cos(3kx) \tag{2.5}$$

with $a = \frac{\pi H}{k \lambda}$ and wave height H. The corresponding phase speed is given by

$$c_{\text{stokes}} = \sqrt{\frac{g}{k}(1 + a^2 k^2)}. \tag{2.6}$$

The steepness of the wave is described by $a^2 k^2$.

An exact solution for pure nonlinear capillary waves has been given by Crapper [1957] and yields a surface profile similar to an inverted Stokes wave. Their phase speed is given by

$$c_{\text{crapper}} = \sqrt{\frac{k\sigma}{\rho} \left(1 + \frac{a^2 k^2}{16}\right)^{-\frac{1}{4}}}. \tag{2.7}$$

These waves are called *Crapper waves* and occur as *parasitic capillaries* on the leeward side of gravity waves. Crapper waves have sharp troughs and flat crests whereas Stokes waves have sharp crests and flat troughs.

2.2 Wave Generation by Wind

2.2.1 Drag Modelling

Ocean water waves propagating along the sea surface can transport momentum in horizontal direction. Any variation in the properties of these waves leads to a horizontal gradient of the momentum flux which can be modelled as a force per unit area acting on the boundary. This force is called radiation stress. A frequently used approach is to parametrize the radiation stress with the wind speed at a specific height above the water surface which is a quantity that is rather easy to measure. This approach is referred to as the bulk aerodynamic method of estimating surface stress [Jones and Toba, 2001].

Wind blowing over a water surface creates a shear stress τ at the water surface by friction. Assuming water to be a Newtonian fluid the shear stress τ defined as the force of friction F per area A is given by Newton's law of friction as

$$\frac{F}{A} =: \tau = \eta \frac{\partial u}{\partial z} \tag{2.8}$$

with the strongly temperature-dependent material constant η – the dynamic viscosity –, velocity u and depth z. The ratio $\frac{\partial u}{\partial z}$ is the local shear velocity. In the literature the shear stress is often related to the shear velocity or *friction velocity* $u_\star$ via density ρ:

$$u_\star^2 := \frac{\tau}{\rho} \tag{2.9}$$

The shear velocity can be seen as a measure of momentum transfer in the turbulent wind field over the boundary layer. The water-sided shear velocity $u_{\star,water}$ is related to the air-sided shear velocity $u_{\star,air}$ via density:

$$u_{\star,water} = \sqrt{\frac{\rho_{air}}{\rho_{water}}} \cdot u_{\star,air} \tag{2.10}$$

2.2.2 Theories of Wave Generation by Phillips and Miles

According to Kinsman [1965] energy can be transferred from the wind to the water by tangential stresses or by pressure fluctuations. When the wind starts to blow (low wind speeds) momentum is transferred via friction at the water surface resulting in tangential shear stress which produces laminar flow. With increasing wind speed the laminar flow becomes unstable and waves begin to form.

In contrast to that description the models of Phillips [1957, 1958, 1977]; Miles [1957] interpret resonant interactions between pressure fluctuations on the surface due to turbulence in the wind on the one hand and water waves on the other hand as the source of energy transfer from the wind to the waves. Both models are well explained in Kinsman [1965]. Janssen [2004] gives an historical overview of the rather complicated topic of wind driven wave generation.

The first work on wind driven wave generation was made by Jeffreys [1925, 1926] who believed that a pressure difference occurring on the lee side of existing waves was doing work on the water ("sheltering hypothesis"). This hypothesis was discarded because laboratory measurements proved that the occurring pressure differences are too small to explain measured wave growth rates.

Phillips [1957] and Miles [1957] developed two separate theories of wind driven wave generation due to a resonance phenomenon at the same time.

Phillips' theory on wave generation by wind is based on resonant interactions between the pressure field of the wind on the one hand and the waves on the other hand. Thus the model of Phillips includes turbulent pressure fluctuations as the source of resonant forcing of surface waves, resulting in a linearly growing wave spectrum in time. The problem of Phillips' model is that the effect has proven ineffective because it is of the order of the square of the density ratio of air and water. Also it does not include any feedback mechanism which makes it applicable for the first stage of wave growth only because there the wave growth is linear. Later, Miles [1959a,b] included partial feedback into Phillips' theory resulting in exponential wave growth.

In the same year as Phillips, Miles [1957] published the so-called "quasi-laminar approach" which is based on free surface waves resonantly interacting with pressure fluctuations due to the waves. In contrast to the model of Phillips, Miles' theory results in an effect that exhibits exponential growth and is of the order of the air-water density ratio. However, Miles' model was highly debated because it neglects the role of turbulence phenomena in the air and other nonlinear effects like the interaction between mean flow and waves. Also, Miles' theory is not in good agreement with field experiments, for example of Dobson [1970]; Snyder et al. [1981].

2.3 Spectral Description of the Wave Field

The wave field of wind driven water waves consists of a multitude of waves, each having its own amplitude, phase velocity and wavelength. Thus it is common practice to use a spectral description of the wave field.

2.3.1 Spectra

Fourier Decomposition

The first conceptual work on spectra was made by Joseph Fourier (1768 - 1830), who demonstrated that any function $\zeta(t) \in \mathcal{L}^2(\mathbb{R}/2\pi)$[2] can be rewritten as an infinite series[3] of sine and cosine functions with harmonic wave frequencies:

$$\zeta(t) = \frac{a_0}{2} + \sum_{n=1}^{\infty}(a_n \cos(2\pi n f t) + b_n \sin(2\pi n f t)) \tag{2.11}$$

with coefficients

$$a_n = \frac{2}{T}\int_{-T/2}^{T/2} \zeta(t)\cos(2\pi n f t)\mathrm{d}t, \qquad (n = 0, 1, 2, \dots)$$

and

$$b_n = \frac{2}{T}\int_{-T/2}^{T/2} \zeta(t)\sin(2\pi n f t)\mathrm{d}t, \qquad (n = 0, 1, 2, \dots)$$

Here $f := \frac{1}{T}$ denotes the fundamental frequency and a_0 represents the mean value of $\zeta(t)$ over the interval $-\frac{T}{2} < t < \frac{T}{2}$. This decomposition of the function ζ nowadays is called a Fourier series.

Wave Energy Density Spectrum

Phillips [1977] defines the wave energy density spectrum $X(\vec{k}, \omega)$ as the Fourier transform of the autocorrelation of the water surface displacement:

$$X(\vec{k}, \omega, \vec{x}, t_0) = \frac{1}{(2\pi)^3} \cdot \int_{-\infty}^{+\infty}\int_{-\infty}^{+\infty} \rho(\vec{x}, \vec{r}, t_0, t) \cdot \exp(-\mathrm{i}(\vec{k}\vec{r} - \omega t))\, \mathrm{d}\vec{r}\, \mathrm{d}t \tag{2.12}$$

$\vec{k}$ describes the wave vector, ω is the frequency, $\vec{x}$ and $\vec{r}$ denote twodimensional spatial vectors and t_0 and t are temporal coordinates. The displacement $\zeta(\vec{r}, t)$ of the water surface relative to the mean free surface level has an expectation value of

---

[2] $\mathcal{L}^2(\mathbb{R}/2\pi)$ is the space of 2π periodic functions from $\mathbb{R}$ to $\mathbb{C}$ with $\mathcal{L}^2(\mathbb{R}/2\pi) := \left\{\zeta : \mathbb{R}/2\pi \to \mathbb{C} : \zeta \text{ measurable}, \int_{-\pi}^{\pi} |\zeta(t)|^2\, dt < \infty\right\}$

[3] over the interval $-\frac{T}{2} < t < \frac{T}{2}$

zero and is included into Equation 2.12 via its autocorrelation function

$$\begin{aligned}\rho(\vec{x},\vec{r},t_0,t) &= \overline{\zeta(\vec{x},t_0)\zeta(\vec{x}+\vec{r},t_0+t)}\\ &= \lim_{T\to\infty}\lim_{X\to\infty}\lim_{Y\to\infty}\frac{1}{8TXY}\int\limits_{-T}^{T}\int\limits_{-X}^{X}\int\limits_{-Y}^{Y}\zeta(\vec{x},t_0)\zeta(\vec{x}+\vec{r},t_0+t)\,\mathrm{d}\vec{x}\,\mathrm{d}t_0 \qquad (2.13)\end{aligned}$$

In reverse, the autocorrelation of the surface displacement can be rewritten in terms of the wave energy density spectrum via an inverse Fourier transform:

$$\rho(\vec{x},\vec{r},t_0,t) = \int\limits_{-\infty}^{+\infty}\int\limits_{-\infty}^{+\infty} X(\vec{k},\omega)\cdot\exp(\mathrm{i}(\vec{k}\vec{r}-\omega t))\,\mathrm{d}\vec{k}d\omega \qquad (2.14)$$

Assuming a homogenous and stationary wave field $X(\vec{k},\omega,\vec{x},t_0) = X(\vec{k},\omega)$ the integration of the wave energy density spectrum over all frequencies and wave numbers yields the mean squared wave height:

$$\int\limits_{-\infty}^{+\infty}\int\limits_{-\infty}^{+\infty} X(\vec{k},\omega)\,\mathrm{d}\vec{k}d\omega = \overline{\zeta^2} \qquad (2.15)$$

which can be deduced by setting $\vec{r} = 0$ and $t = 0$ in Equation 2.12 and Equation 2.13.

The wave energy density spectrum denotes the distribution of wave energy among different wave frequencies (or wave-lengths). Multiplication of Equation 2.15 with $\frac{1}{2}\rho g$ yields the mean potential energy, leading to the interpretation of $X(\vec{k},\omega)$ as the mean energy of a gravity wave with wave vector $\vec{k}$ and wavelength ω.

Reduced Spectra: Wave number Energy Spectrum, Frequency Energy Spectrum

Reduced spectra are obtained from the wave energy density spectrum $X(\vec{k},\omega)$ by integration. Integration over the wave number vector yields the frequency energy spectrum

$$\Phi(\vec{k}) = \int\limits_{-\infty}^{+\infty} X(\vec{k},\omega)\,\mathrm{d}\vec{k} \qquad (2.16)$$

whereas integration over all frequencies yields the wave number energy spectrum

$$\Psi(\vec{k}) = \int\limits_{-\infty}^{+\infty} X(\vec{k},\omega)\,\mathrm{d}\omega \qquad (2.17)$$

Integrating the wave number energy spectrum over the components of the wave number vector separately (i.e. a onedimensional projection on the respective wave number axis) leads to onedimensional transverse wave number spectra:

$$\Psi(k_x) = \int_{-\infty}^{+\infty} \Psi(k_x, k_y)\,\mathrm{d}k_y \tag{2.18a}$$

$$\Psi(k_y) = \int_{-\infty}^{+\infty} \Psi(k_x, k_y)\,\mathrm{d}k_x \tag{2.18b}$$

Rewriting $\Psi(\vec{k})$ as $\Psi(k, \theta)$ with $k = |\vec{k}|$ and $\theta = \arctan \frac{k_y}{k_x}$ allows for calculating the omnidirectional spectrum by integrating over all directions of propagation:

$$\Psi(k) = \int_{-\pi}^{+\pi} \Psi(k, \theta)\,\mathrm{d}\theta \tag{2.19}$$

Similarly, the unidirectional wave number spectrum is obtained with different integration limits and a scaling with $\frac{1}{\pi}$:

$$\tilde{\Psi}(k) = \frac{1}{\pi} \int_{-\frac{\pi}{2}}^{+\frac{\pi}{2}} \Psi(k, \theta)\,\mathrm{d}\theta \tag{2.20}$$

Similar definitions follow from the frequency spectrum. Typically, frequency spectra can be obtained from measurements with capacitive wave wires which determine the surface elevation at one point in space. With imaging techniques it is possible to determine wave number spectra even for low temporal resolution. With sufficiently high temporal resolution, the full energy density spectrum can be obtained.

Power Spectra and Slope Spectra

The definitions given above can be made with surface displacement ζ or with surface slope s. In the following derivation, let $\hat{\zeta}(\vec{k}) = \frac{1}{(2\pi)^3} \int \zeta(\vec{x}, t) \exp(-\mathrm{i}\vec{k}\vec{x})\,\mathrm{d}\vec{x}$ be the Fourier transform of the surface displacement and $\hat{s}$ be the Fourier transform of the surface slope. The squared absolute value of the Fourier transform of surface displacement and surface slope define the power spectra of displacement $F(\vec{k}) = |\hat{\zeta}|^2$ and slope $S(\vec{k}) = |\hat{s}(\vec{k})|^2$, respectively.

The total slope wave number power spectrum $S(\vec{k})$ can be decomposed into the alongwind component and the crosswind component:

$$S(\vec{k}) = S_x(\vec{k}) + S_y(\vec{k}) \tag{2.21}$$

Due to slope being the derivative of surface height[4] the inherent properties of the

---

[4] $s_x(\vec{x}) = \frac{\partial}{\partial x}\zeta(\vec{x}),\ s_y(\vec{x}) = \frac{\partial}{\partial y}\zeta(\vec{x})$

Fourier transform yield the following relations:

$$\hat{s}_x = -\mathrm{i}k_x\hat{\zeta} \tag{2.22a}$$

$$\hat{s}_y = -\mathrm{i}k_y\hat{\zeta} \tag{2.22b}$$

$$|\hat{s}_x|^2 + |\hat{s}_y|^2 = k^2|\hat{\zeta}|^2 \tag{2.22c}$$

With a sufficient amount of statistically independent images of the water surface displacement at different points in time $\zeta_i(\vec{x}) = \zeta(\vec{x}, t = t_i)$ the wave number energy spectrum can be obtained from the mean of the power spectra of displacement $F_i(\vec{k})$ and vice versa:

$$\Psi(\vec{k}) \approx F(\vec{k}) = \frac{1}{N}\sum_{i=1}^{N} F_i(\vec{k}) = \frac{1}{N}\sum_{i=1}^{N} |\hat{\zeta}_i(\vec{k})|^2 = \frac{1}{N}\sum_{i=1}^{N} k^{-2}|\hat{s}_x|^2 + |\hat{s}_y|^2 = k^{-2}S(\vec{k}) \tag{2.23}$$

Saturation Spectrum / Wave Spectrum Models

For the analysis of small scale water waves, the wave number energy spectrum as defined in Equation 2.17 is commonly rewritten as the dimensionless saturation spectrum which is defined as

$$B(\vec{k}) = k^4\Psi(\vec{k}) = k^2S(\vec{k}) \tag{2.24}$$

The main advantage of this notation is the reduced range of the spectrum which is useful especially for plotting purposes. Other names for the saturation spectrum are the degree of saturation or the curvature spectrum. The latter term is comprehensible because the second derivative of the surface elevation (i.e. the curvature) is $k^4\Psi(\vec{k})$. The term degree of saturation was invented by Phillips [1958] who conducted research on the fundamental form of wave spectra. Phillips introduced the saturation range model based on a stationary wave field with the assumption that the energy input from the wind and the dissipation by breaking waves compensate each other. This leads to a saturation of the wave field and an upper limit for the wave number. This upper limit is assumed to be independent of the wind induced energy input and thus determined by the restoring capillary and gravity forces only. With the additional assumption that B depends on the direction of the wave number vector relative to the wind (given by the angle θ) only, Phillips used dimensional arguments to deduce that for gravity waves the wave number energy spectrum is of the form

$$\Psi(\vec{k}) = \beta f(\theta) \cdot k^{-4} \tag{2.25}$$

Here $f(\theta)$ is an angular spreading function which describes the directionality of the waves and is not specified in further detail. β is a proportionality constant which may differ for the gravity regime and the capillary regime.

Many authors developed models in order to predict the shape of the saturation spectrum for gravity waves. Kitaigorodskii [1983] and Phillips [1985] both found a $k^{\frac{1}{2}}$ dependency of the saturation spectrum, but for different regimes of the wave number:

$$\Psi(\vec{k}) \propto u_\star k^{-\frac{7}{2}} \qquad\qquad B(\vec{k}) \propto f(\theta) u_\star k^{\frac{1}{2}} \tag{2.26}$$

The model of Phillips[5] is based on a local equilibrium of the spectral flux and includes non-linear interactions between waves as well as different mechanisms of dissipation due to the breaking of waves, turbulent diffusion, and viscous dissipation. The energy input is assumed to stem from the turbulent wind field.

In contrast, Zakharov and Filonenko [1967]; Kitaigorodskii [1983]; Pushkarev et al. [2003]; Dyachenko et al. [2004] developed a model which contains analogies to the turbulence model of Kolmogorov [1941]. This is why it is called the weak turbulence model. The underlying assumption of this approach is that the energy input occurs at small wave numbers (i.e. large wavelengths) and after that the energy is transferred by nonlinear interactions until it is dissipated at large wave numbers.

2.3.2 Slope Probability distribution

The slope probability distribution $\rho(\vec{s})$ is a probability density function for water wave surface slope. It also allows for a statistical analysis of the wave field. One can calculate the probability $P(\vec{s}, \vec{\delta})$ of measuring a value $\vec{s} = (s_x, s_y)^T$ inside the interval $I(\vec{s}, \vec{\delta}) = \{(s'_x, s'_y) | s_x - \delta_x < s'_x \leq s_x + \delta_x \text{ and } s_y - \delta_y < s'_y \leq s_y + \delta_y\}$ when performing a single measurement from the slope probability distribution:

$$P(\vec{s}, \vec{\delta}) = \int\limits_{s'_x - \delta_x}^{s'_x + \delta_x} \int\limits_{s'_y - \delta_y}^{s'_y + \delta_y} \rho(\vec{s}\,') \, \mathrm{d}s'_x \, \mathrm{d}s'_y \tag{2.27}$$

In order to meet the definition of a probability density function the slope probability distribution is normalised to 1:

$$\int \int \rho(\vec{s}\,') \, \mathrm{d}s'_x \, \mathrm{d}s'_y = 1 \tag{2.28}$$

---

[5] valid for large wave numbers in the gravity wave regime

2.4 Mean Square Slope

Mean square slope is another parameter which is frequently used to describe the wave field. Jähne et al. [1987] showed that it correlates well with the transfer velocity k for air sea gas interaction which is one of the main reasons this parameter is of interest for the scientific community. For a stationary wave field fulfilling the principle of superposition the central limit theorem of statistics leads to $P(\vec{s})$ being a Gaussian distribution:

$$P(\vec{s}) = \rho_{\text{Gauß}} = \frac{1}{2\pi\sigma_x\sigma_y} \cdot \exp\left(-\frac{s_x^2}{2\sigma_x^2} - \frac{s_y^2}{2\sigma_y^2}\right) \tag{2.29}$$

with zero mean:

$$\langle x \rangle = \frac{1}{2\pi\sigma_x\sigma_y} \int\int \exp\left(-\frac{s_x^2}{2\sigma_x^2} - \frac{s_y^2}{2\sigma_y^2}\right) \mathrm{d}x\,\mathrm{d}y \tag{2.30}$$

Then the sum of the two variances σ_x and σ_y yields mean square slope s^2:

$$\langle s^2 \rangle = \langle s_x^2 \rangle + \langle s_y^2 \rangle = \sigma_x^2 + \sigma_y^2 = \sigma^2 \tag{2.31}$$

A rotation of the coordinate system such that one axis is aligned with the wind direction has been established. Then the components of slope and of the variance are called the upwind component σ_u^2 or s_u along this axis and the crosswind component σ_c^2 or s_c along the perpendicular axis. The larger the ratio $\frac{\sigma_c^2}{\sigma_u^2}$ of the two components of the variance is, the more isotropic is the wave field.

Wind driven water waves are a little more complicated than this simple model. First, nonlinear interactions of the water waves lead to a violation of the principle of superposition. Second, parasitic capillary waves exhibit a preference for the downwind side of gravity waves which results in an asymmetry of the probability distribution. Third, due to physical constraints, the steepness of waves is limited. These limitations can be modelled by the inclusion of additional parameters. Cox and Munk [1954b] introduced the Gram-Charlier distribution to do this modelling for the twodimensional case:

$$\begin{aligned} P_{\text{gc}}(\eta, \xi) = & \frac{1}{2\pi\sigma_c\sigma_u} \cdot \exp\left(-\frac{\eta^2 + \xi^2}{2}\right) \\ & \cdot [1 - \frac{1}{2}C_{21}(\xi^2 - 1)\eta - \frac{1}{6}C_{03}(\eta^3 - 3\eta) + \frac{1}{24}C_{40}(\xi^4 - 6\xi^2 + 3) \\ & + \frac{1}{4}C_{22}(\xi^2 - 1)(\eta^2 - 1) + \frac{1}{24}C_{04}(\eta^4 - 6\xi^2 + 3) + \ldots] \end{aligned} \tag{2.32}$$

which they found to be sufficient for slopes up to $\eta = \xi = 2.5$ [6]. The coefficients C_{21} and C_{03} describe the skewness of the distribution which represents the asymmetry of the distribution and the coefficients C_{40}, C_{22} and C_{04} describe the peakedness which is a measure of the deviation of the steepness of the distribution compared to the Gaussian distribution. All these coefficients have to be evaluated from the data. In Kiefhaber [2014], a brief overview of different methods for determining mean square slope is given.

2.5 Waves and Air-Sea Gas Exchange

Water waves are an important parameter for the exchange processes of heat, trace gases and momentum between the ocean and the atmosphere. Over the last years, the search for a physically based model of air-sea gas exchange which includes the effects of the wave field arose. This section serves as a brief summary of air-sea gas exchange and the influence of water waves.

2.5.1 Transport Mechanisms

Turbulent and molecular motion are the two fundamental mechanisms of mass transport in fluids[7]. Both can be described by Reynolds decomposition similar to Fick's law for diffusion, but with a turbulent diffusion coefficient $K(z)$ in addition to the molecular diffusion constant D. Assuming homogeneity in the horizontal directions x and y, the flux j_c of a trace gas is given by the concentration gradient

$$j_c = -(D + K(z)) \bigtriangledown c = -(D + K(z)) \frac{\partial c}{\partial z}. \tag{2.33}$$

Molecular diffusion dominates in the boundary layers at the air-water interface which have a typical thickness of less than a millimetre whereas turbulent transport is more efficient on large scales. Close to the interface, the size of turbulent eddies shrinks as the eddies cannot penetrate the interface. The turbulent diffusion coefficient $K(z)$ is significantly reduced close to the interface.

---

[6] Note that η and ξ denote normalized slope components $\eta = \frac{s_c}{\sigma_c}$ and $\xi = \frac{s_u}{\sigma_u}$

[7] Among others, the term *fluid* refers to air and water.

Transfer Velocity

The rate of air-sea gas transfer can be described macroscopically by integration[8] of Equation 2.33:

$$c(z_2) - c(z_1) = -j_c \int_{z_1}^{z_2} (D + K(z))^{-1} \, \mathrm{d}z := j_c R = \frac{j_c}{k}. \tag{2.34}$$

This defines the *transfer velocity* k and its inverse, the *transfer resistance* R, which contain the turbulent structures in the boundary layer.

2.5.2 Measuring and Modelling Gas Exchange

Direct measurements of gas concentration profiles in the boundary layers are highly demanding, especially in the presence of waves, because of the small thickness of the layers in combination with the large amplitude of the motion at the water surface. Various models have been proposed to describe the transfer velocity k [Lamont and Scott, 1970; Deacon, 1977; Coantic, 1986]. The model of Jähne et al. [1987] expresses k by the water-side friction velocity $u_\star$, the Schmidt number $Sc = \frac{\nu}{D}$ with the kinematic viscosity ν, the dimensionless Schmidt number exponent n and a dimensionless scaling parameter β to describe the strength of near-surface turbulence:

$$k = \frac{1}{\beta} u_\star \mathrm{Sc}^{-n}. \tag{2.35}$$

Both β and n depend on the wave field but the exact dependency is still unknown. Jähne et al. [1979] give a Schmidt number exponent of $\frac{1}{2}$ for a rough, wavy water surface and Deacon [1977] proposed a value of $\frac{2}{3}$ for a smooth water surface. A gradual transition between these limiting cases was found by Nielsen [2004]; Krall [2013] for which the *facet model* Jähne and Bock [2002] accounts. A similar model was reported by Zappa et al. [2001, 2004].

Evidence exists that wind speed alone is not sufficient to parametrize transfer velocities [Wanninkhof et al., 2009]. Jähne et al. [1987] suggest the mean square slope σ^2 of the waves as a parameter which has empirically proven to correlate well with gas transfer velocities Bock et al. [1999]; Kiefhaber [2014]. Yet a fundamental link between gas exchange and mean square slope is missing whereas it exists for parameters such as the surface divergence or turbulent kinetic energy dissipation (TKE). Nevertheless, mean square slope has the significant advantage that it can be measured on small and large scales with comparably low effort.

---

[8] The integration is valid as presented when mass sources or sinks are absent because j_c is constant due to mass conservation.

2.6 Surface Films

Surface films, also called surfactants[9] are a species of molecules which enrich at the surface of a liquid (e.g. for thermodynamic reasons). Surfactants influence surface tension: adding surfactants to a liquid lowers the liquids surface tension and modifies the free surface boundary condition in the tangential direction. Here the visco-elasticity plays an important role: the surface film is pushed together and pulled apart due to the orbital movement in a wave. This process dissipates energy transferred from the wind field. This in turn suppresses capillary waves and capillary-gravity waves (Gade et al. [2006]; Mitsuyasu and Bock [2001]). Alpers [1989] explained that not only capillary waves, but also short gravity waves are damped by surface films due to the Marangoni effect. In the following sections the most important properties of surface active agents will be described. Their classification into different subtypes will be explained and those used for experiments for this thesis will be explained in further detail.

2.6.1 Surfactants

Surfactants usually are amphiphilic substances. Thus they consist of at least two parts; the polar (hydrophilic) head determining the properties of the molecule and the hydrophobic tail consisting of a – possibly branched or aromatic – hydrocarbon chain. Therefore, surfactants consist of a component that is soluble in water and one that is insoluble in water but soluble in oil and other unpolar solvent. Also some oligomers and polymers act like surfactants.

Due to their hydrophobic parts surfactants tend to form clusters in the water body (called micelles, see Figure 2.1) as soon as a material dependent concentration, the so called "critical micelle concentration (CMC)" is reached. Below the CMC surfactants form a monomolecular layer at the water surface in order to minimize the contact between the hydrophobic tails of the molecules and the surrounding water molecules.

The hydrocarbon tail of surfactants often contains an even number of carbon atoms and strongly influences the surface packing of the surfactant. An amide bond improves surface packing (van Os [1997]) and planar ring structures such as sterols provide good packing (Holmberg [2001]). Double bonds in the hydrocarbon tail are more hydrophilic (Holmberg [2001]), thus increasing the CMC (Myers [2005]). Large, stiff tails (sterol ethoxylates) lead to a long time in order to reach an equilibrium state of surface tension (Holmberg [2001]).

Typically surfactants are enriched at the water surface and reduce the free energy at the surface and thus also the surface tension γ which can be described by the

---

[9] **surf**ace **act**ive **a**ge**nts**

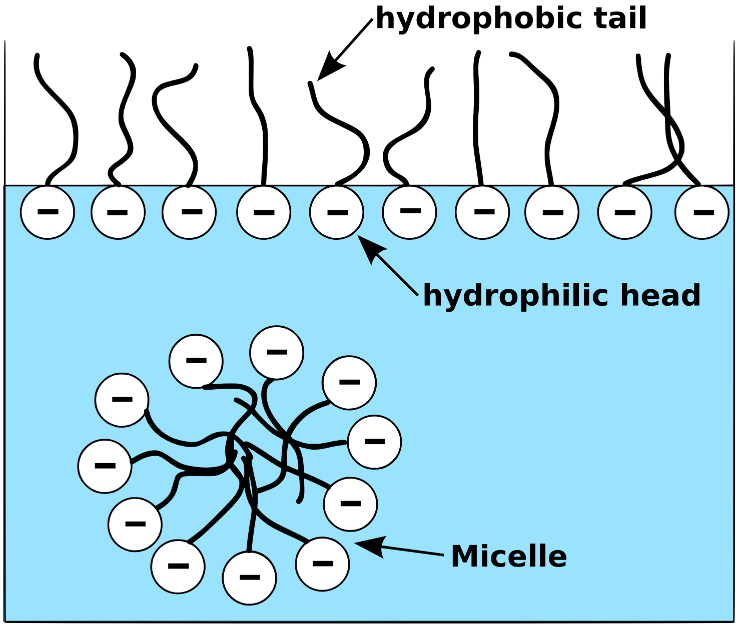

Figure 2.1.: Surfactants sticking to the air-water interface. As soon as the critical micelle concentration (CMC) is reached, micelles are formed. Image taken from Krall [2013], modified after Stapf [2010].

Gibbs isotherm (Equation 2.36)

$$-d\gamma = \sum_i \Gamma_i d\mu_i \tag{2.36}$$

where Γ_i is the surface excess of component i and μ_i is the chemical potential of component i. Important effects of surfactants – apart from lowering the surface tension and wave damping – include foam stabilization, emulsification, dispersion (immersion wetting) and the enhancement of wetting.

In the oceans surfactants are of major importance for biological organisms and perform many different tasks such as the transport across cellular membranes or building lipid bilayer membranes. Most naturally occurring oceanic surfactants are produced by phytoplankton during photosynthesis. They also occur as byproducts when dead organisms are degraded by microorganisms. Amongst others, the amount of surfactants found at the ocean surface varies due to hydrodynamics at the interface as well as the availability of nutrients to surfactant-producing organisms (Wurl et al. [2011]; Cunliffe et al. [2013]).

Micelles

Micelles formed by surfactants are highly soluble, polar clusters which exhibit small surface activity. They may consist of different types of surfactants and can be regarded as a reservoir for dissolved surfactants. Their relaxation times are in the order of ms (Shah [1998]). The critical micelle concentration (CMC) at which micelles start to form is determined by the charge of the polar head group, the length of the hydrocarbon chain, the number of double bonds in the hydrocarbon chain and is influenced by cosolutes such as salts or alcohols, temperature and pressure (Farn [2008]). When the CMC is reached, surfactant solubility often increases enormously because excess molecules are transported into the water body to form micelles.

2.6.2 Classification of Surfactants

Surfactants can be grouped into soluble and insoluble species. Soluble surfactants adsorbed to the surface have a relatively higher concentration than in the bulk of the liquid whereas insoluble surfactants adsorbed to the surface have rearranged such that the forces occurring between the molecules are minimal. Surfactants can be classified according to the charge of their polar head group into anionic, cationic, non-ionic and zwitterionic surfactants. An overview over different classes of surfactants is given in Nagel [2013]; here the most important properties are repeated. A more detailed description of the classification of surfactants and their chemical properties is given in Tsujii [1998].

Anionic surfactants Anionic surfactants span the largest class of surfactants and are those which are most commonly used. Their polar head group is composed of a carboxyl, sulfate, sulfonate or phosphate group. In water, they dissociate into an anion and a cation, which often is an alkaline metal. Anionic surfactants are generally sensitive to water hardness. Sulfates are rapidly hydrolysed by acids, whereas the other types of anionic surfactants are stable unless under extreme conditions.

Cationic surfactants Cationic surfactants are mostly composed of permanently charged quaternary ammonium cations (NR_4^+) or amines (NH_2R_1, NHR_2,NR_3). Amines only act as surfactants in protonised state, i.e. for low to neutral pH values whereas quaternium amonium is insensitive to pH. Other types of cationic surfactants include phosphonium, sulfonium & sulfoxonium, but they are rarely used due to their high costs. Cationic surfactants exhibit high water toxicity because they are hydrolytically stable. Since most materials are negatively charged when they are surrounded by an aquaeous medium the positively charged head group of cationic surfactants is attracted, leading to a strong adsorption of the cationic surfactant to most surfaces.

Nonionic surfactants Nonionic surfactants consist of polyether or polyhydroxyl head groups. They are insensitive to water hardness and their physiochemical properties are not affected by electrolytes; in return they exhibit temperature-dependent behaviour: with increasing temperature the solubility of nonionic surfactants in water decreases (Atwood and Steed [2004]). A major drawback of nonionic surfactants is their high skin-irritating potential.

Zwitterionic surfactants Finally, zwitterionic surfactants which are the smallest and most expansive group of surfactants contain two charged groups of different sign. The positively charged group is composed of ammonium whereas the negatively charged group varies, but is commonly a carboxylate. Zwitterionic surfactants contain a subgroup named amphoteric surfactants which can react as an acid as well as a base. Zwitterionic surfactants are generally stable in acid and alkaline surroundings and are insensitive to hard water. Moreover they exhibit excellent dermatological properties.

2.6.3 Surfactants used for this thesis

Naturally occurring surfactants exhibit a large variation of weight and chemical composition. For this work the influence of surfactants on water wave surface slope was investigated. Therefore, five different kinds of surfactants were used. Their chemical structure is depicted in Figure 2.2.

Natural surface films

During the first type of experiments surfactants were chosen to mimic natural surface films. The chemical composition of the sea surface microlayer was analysed by Tepić et al. [2009]; Gašparović et al. [2007]; Ćosović and Vojvodić [1998] and others who found polysaccharides, lipids and fatty acids to be the main components. A mixture of the following four surfactants was used to reproduce natural conditions:

Dextran Dextran is a soluble surfactant which is naturally produced by synthesis of sucrose by various species of bacteria. Dextran is a branched glucan containing a mixture of different polysaccharides[10] with a molecular weight of 10 000 u to 50 000 000 u. Tepić et al. [2009] demonstrate the usability of dextran as a model substance for the influence of polysaccharides on air-sea gas exchange.

---

[10] Polysaccharides consist of glucose molecules with the molecular formula $(C_6H_{10}O_5)_n$.

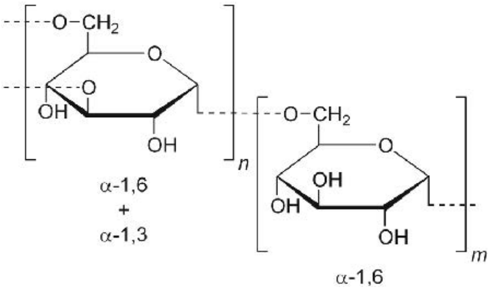

(a) Dextran

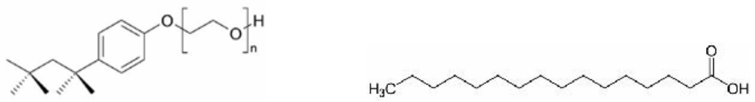

(b) Triton X-100 **(c)** Palmitic Acid (PA)

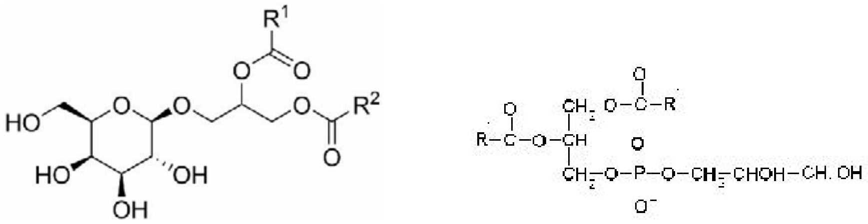

(d) Mono-Galactosyl-Diacylglycerol (MGDG) **(e)** Phosphatidylglycerol (PG)

Figure 2.2.: Chemical structure of the surfactants used for the experiments in this thesis. R^1 and R^2 denote organic radicals. Image taken from Nagel [2014]

Mono-Galactosyl-Diacylglycerol (MGDG) Mono-Galactosyl-Diacylglycerol is an insoluble surfactant that is produced by algae and is contained in the membranes of chloroplasts. It belongs to the chemical class of glycolipids which are lipids with attached carbohydrates and has a neutral headgroup. MGDG is one of the most common glycolipids in plant cells.

Phosphatidylglycerol (PG) Phosphatidylglycerol is an insoluble surfactant which occurs in the cell membranes of bacteria, algae and other marine organisms. Chemically it belongs to the class of glycerophospholipids and is used as a model substance for lipids.

Palmitic Acid (PA) Palmitic Acid ($CH_3(CH_2)_{14}COOH$, hexadecanoic acid in IUPAC nomenclature) is an insoluble surfactant which is naturally produced by marine organisms during the synthesis of fatty acids. It is used as a model substance for fatty acids. PA has a molar mass of 256.42 g/mol and a density of 0.8527 g/cm^3 at 62 °C (Lide [2005]). The solubility of PA in water is about 0.04 mg/l at 25 °C (Robb [1966]).

Synthetic surfactant

Because of its well-known properties and comparability to older studies one part of the experiments were conducted with synthetic surface active substance Triton X-100.

Triton X-100 Triton X-100 ($C_{14}H_{22}O(C_2H_4O)_n$[11], scientific name polyethylene glycol p-(1,1,3,3-tetramethylbutyl)-phenyl ether) belongs to the class of nonionic surfactants. It is soluble and synthetically produced. Its molecular mass is 647 g/mol and its density is 1.07 g/cm^3. The critical micelle concentration is at 0.22 mol/l–0.24 mol/l and its viscosity is 2.4 g/(cm s) at 25 °C (Sigma Aldrich [1999]).

2.6.4 The sea-surface microlayer

The sea surface microlayer (SML) is the boundary layer interface at the oceanic water surface with a thickness of a few tens to hundreds of micrometers. The sea surface microlayer is characterized by its distinctive physico-chemical properties which differ from those of the subsurface water below. The SML consists of a highly hydrated loose gel of tangled macromolecules and colloids at the air-water interface (Cunliffe et al. [2013]) and includes surfactants. As such, it is remarkably stable: even under conditions with high turbulence it covers most of the water surface and it remains stable up to a wind speed of at least 10 m/s (Wurl et al. [2011]; Carlson [1983]; Kuznetsova et al. [2004]; Reinthaler et al. [2008]). After mixing the water the SML is rapidly reformed at timescales of typically less than 1 min (Cunliffe et al. [2013]). An important effect influencing the SML is the so-called bubble scavenging: the formation of the SML is enhanced by rising bubble plumes (Zhou et al. [1998]; Wallace and Duce [1978]). It has been found that the SML plays a fundamental role in air-sea gas exchange processes and is linked to the production of aerosols. The bacterioneuston which contributes to the SML has been shown to contribute to the air-sea gas exchange for at least some types of gas (Cunliffe et al. [2013]).

---

[11] On average, n=9.5.

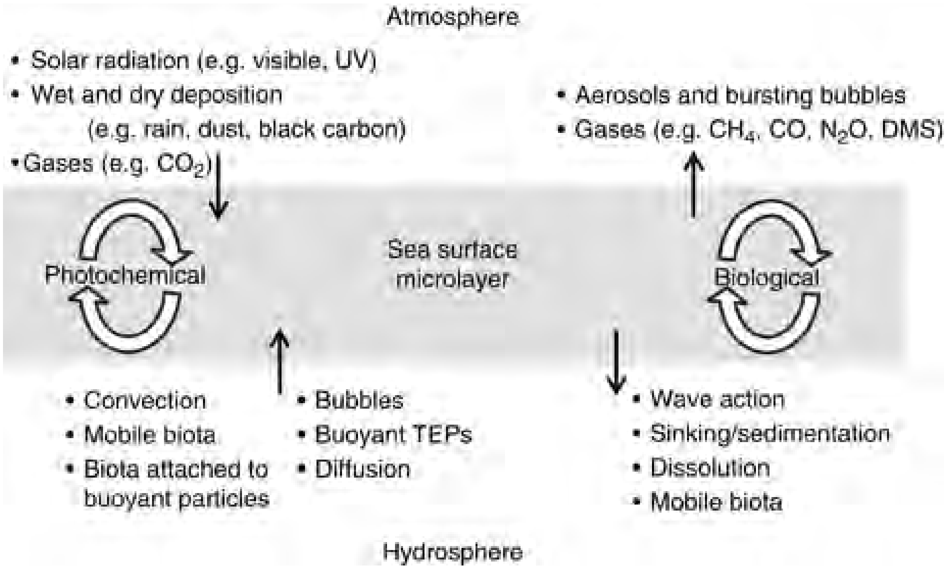

Figure 2.3.: Interactions involving the Sea Surface Microlayer. Image taken from Cunliffe et al. [2011].

2.6.5 Effects of surfactants on water waves and air-sea gas transfer

Several authors (Levich [1962]; Hansen and Mann [1964]; Lucassen-Reynders and Lucassen [1970]) gave an explanation of the damping of capillary ripples by surface films. Today it is believed that during the propagation of the small waves local changes of the hydrodynamic boundary conditions occur, i.e. the water surface is locally compressed and dilated. This in turn leads to local changes of surface tension which can be described by a complex-valued viscoelastic modulus. Bock and Mann [1989] gave a corrected dispersion relation for surface waves in the presence of surfactants which was later verified by several laboratory experiments.

Today it is believed that wind-driven water waves are damped by surfactants due to one or more of the following mechanisms:

- A finite viscoelastic modulus is created by the surfactant which leads to a change in the dispersion relation of the waves. This in turn increases energy dissipation.
- A change of the surface roughness of the water due to the surfactant leads to a decrease of the energy-flux from the wind to the water waves.
- The modifications of the wave field, which occur because of the presence of a surfactant, change the effect of the nonlinear interactions of the waves leading to faster dissipation of energy.

The generation of water waves by wind is also changed in the presence of surfactants as the energy input by wind shear as well as energy transfer and energy dissipation in the wave field are modified. When surfactants are present a critical wind speed has to be exceeded in order to generate waves. Scott [1972] demonstrated that this is not true for a clean water surface whereas Mitsuyasu and Bock [2001] show that highly concentrated surfactants suppress the generation of water waves by wind up to a critical wind speed but at very high wind speeds their effect vanishes. In general, the effect of surfactants on the wave field and near-surface turbulence is larger for low wind speeds which is explained by a rupture of the surface film at higher wind speeds leading to a mixing of the surfactants with the bulk water.

Also, the wind profile changes in the presence of surfactants due to the induced change of surface roughness.

Concerning air-sea gas exchange, Liss and Slinn [1983] showed that gas molecules are not directly obstructed in passing the interface by the surfactant molecules. Nevertheless surfactants reduce air-sea gas transfer by up to 50 % (Frew et al. [1990]) or even 60 % for low to medium wind speeds (Krall [2013]).

2.6.6 Marangoni effect

Marangoni waves are predominantly longitudinal waves occurring in the boundary layer which have been experimentally detected by Lucassen [1968a,b]. They are visible as oscillations of the air-water interface whose wavelengths depend on surface tension [Lombardini et al., 1982]. Marangoni waves occur due to instabilities of the air-water interface which are evoked by surface tension gradients (e.g. stemming from surface films). A tangential force generated by these gradients acts as restoring force.

Viscoelastic surface films influence the flow patterns in the boundary layer because they modify the boundary conditions of the surface. In the presence of surface films, Marangoni waves are important because of their interactions with transversal gravity-capillary waves which cause local compression and dilation of the surface film. These in turn lead to surface tension gradients which excite Marangoni waves. Nonlinear wave-wave interactions result in a transfer of energy from longer waves to an energy sink in the Marangoni region. Marangoni waves are strongly damped on the scale of one wavelength [Alpers, 1989]. This effect is associated with strong velocity gradients in the boundary layer which leads to an enhancement of viscous dissipation. Thus, the Marangoni effect leads to strong damping of short gravity waves. Surface films with higher elasticity lead to stronger wave damping.

3

Foundations in Signal Processing

The process of wave imaging transforms the continuous wave signal into a discrete (digital) dataset represented by intensity values at given pixel positions. Discrete signals have to be treated slightly differently than continuous signals. The most important concepts of signal processing of discrete data which are necessary for the evaluation of ISG raw data are presented in the following sections. These include the discrete Fourier transform (DFT), the theory of aliasing, spectral analysis and digital filtering using window functions.

3.1 Discrete Fourier Transform (DFT)

The discrete Fourier transform (DFT) is a transform which converts a finite and equally spaced signal into a finite combination of complex sinusoids which represent a discrete and periodic frequency spectrum. Thus, the DFT converts the sampled function from its original domain (spatial or temporal) to the frequency domain.

For application in image processing, the 2D-DFT is of special interest. For a signal $S = (s_{m,n})$ of size (M, N) it is defined as

Definition 3.1 (2D Discrete Fourier Transform (2D-DFT))

$$\hat{s}_{k,l} = \sum_{m=0}^{M-1} \sum_{n=0}^{N-1} s_{m,n} \cdot \mathrm{e}^{-2\pi\mathrm{i}\cdot\frac{mk}{M}} \mathrm{e}^{-2\pi\mathrm{i}\cdot\frac{nl}{N}} \tag{3.1}$$

where $k = 0, \ldots, M-1$ *and* $l = 0, \ldots, N-1.$

The inverse transform is given by

Definition 3.2 (2D Inverse Discrete Fourier Transform (2D-IDFT))

$$s_{m,n} = \frac{1}{MN} \sum_{k=0}^{M-1} \sum_{l=0}^{N-1} \hat{s}_{k,l} \cdot e^{2\pi \mathrm{i} \cdot \frac{mk}{M}} e^{2\pi \mathrm{i} \cdot \frac{nl}{N}} \tag{3.2}$$

where $m = 0, \ldots, M-1$ *and* $n = 0, \ldots, N-1$.

For two-dimensional images, the indices k and l are often called *wave numbers*. The extension of the DFT to three dimensions is obvious and is not given here explicitly. Often, the third dimension is time which becomes an (angular) frequency ω in Fourier space.

Important properties of the DFT are completeness, orthogonality and periodicity:

Completeness

The DFT is an invertible and linear transformation $\mathcal{F}\colon \mathbb{C}^M \to \mathbb{C}^M$. Here $\mathbb{C}$ denotes the set of complex numbers. This means that the DFT maps any M-dimensional complex vector onto another M-dimensional complex vector for any $M > 0$. Concurrently, the inverse mapping IDFT coexists for every M-dimensional complex vector.

Orthogonality

The vectors $e_k = \left[\exp(\frac{2\pi i}{M} km) \mid m = 0, 1, \ldots, M-1\right]^T$ form an orthogonal basis over the set of M-dimensional complex vectors:

$$e_k^T e_{k'}^\star = \sum_{m=0}^{M-1} \left(\exp(\frac{2\pi i}{M} km)\right) \cdot \left(\exp(\frac{2\pi i}{M}(-k')m)\right) = \sum_{m=0}^{M-1} \exp(\frac{2\pi i}{M}(k-k')m) = M\,\delta_{kk'}$$

where $\circ^T$ denotes transposition, $\circ^\star$ denotes complex conjugation and $\delta_{kk'}$ denotes the Kronecker delta.

Periodicity

The periodicity can be shown directly from the definition:

$$\begin{aligned}
\hat{s}_{k+M,l} &\coloneqq \sum_{m=0}^{M-1} \sum_{n=0}^{N-1} s_{m,n} \cdot \mathrm{e}^{-2\pi \mathrm{i} \cdot \frac{m(k+M)}{M}} \mathrm{e}^{-2\pi \mathrm{i} \cdot \frac{nl}{N}} \\
&= \sum_{m=0}^{M-1} \sum_{n=0}^{N-1} s_{m,n} \cdot \mathrm{e}^{-2\pi \mathrm{i} \cdot \frac{mk}{M}} \underbrace{e^{-2\pi i M}}_{1} \mathrm{e}^{-2\pi \mathrm{i} \cdot \frac{nl}{N}} \\
&= \sum_{m=0}^{M-1} \sum_{n=0}^{N-1} s_{m,n} \cdot \mathrm{e}^{-2\pi \mathrm{i} \cdot \frac{mk}{M}} \mathrm{e}^{-2\pi \mathrm{i} \cdot \frac{nl}{N}} = \hat{s}_{k,l}.
\end{aligned}$$

Plancherel Theorem and Parseval's Theorem

The Plancherel theorem and Parseval's theorem are two results from harmonic analysis which relate a function in its natural domain to its Fourier spectrum. Let $\hat{F}_k$ and $\hat{G}_k$ be the (1D)-DFTs of f_n and g_n, respectively. The Plancherel theorem states:

Definition 3.3 (Plancherel Theorem)

$$\sum_{n=0}^{N-1} f_n g_n^* = \frac{1}{N} \sum_{k=0}^{N-1} \hat{F}_k \hat{G}_k^* \tag{3.3}$$

where the star denotes complex conjugation.

A special case of the Plancherel theorem is Parseval's theorem. It reads:

Definition 3.4 (Parseval's Theorem)

$$\sum_{n=0}^{N-1} |f_n|^2 = \frac{1}{N} \sum_{k=0}^{N-1} |\hat{F}_k|^2 \tag{3.4}$$

3.1.1 The Alias Effect, Digital Filtering and the Nyquist-Shannon Sampling Theorem

Usually the discrete signal is created by discretizing a continuous signal. The term *sampling* describes the process of converting a function of continuous time or space into a numeric sequence such as a function of discrete time or space. The samples of a function $f(t)$ are commonly denoted by $f[n] := f(nT)$ for integer values of n.

The spectra obtained from the DFT will be the correct discrete representation of the spectra of the underlying signal when the Nyquist–Shannon sampling theorem is not violated. The Nyquist–Shannon sampling theorem provides a connection between continuous and discrete signals:

Definition 3.5 (Nyquist-Shannon Sampling Theorem)
If a function f contains no frequencies higher than B, it is completely determined by giving its ordinates at a series of points spaced $\frac{1}{2 \cdot B}$ seconds apart (Shannon [1949]).

This means that the sampling frequency f_s has to be more than twice the maximum frequency B of the original band-limited signal[1] in order to avoid a loss of information during sampling. The frequency $f_{\text{Nyquist}} := \frac{1}{2} f_{\text{sampling}}$ is then called the *Nyquist frequency*. The term *Nyquist rate* describes the minimum sampling rate $f_{\text{sampling}} := 2B$ that satifies the Nyquist–Shannon sampling theorem for a given signal. Thus, the Nyquist rate can be interpreted as a property of the continuous signal, whereas the Nyquist frequency is seen as a property of the discrete system.

---

[1] A bandlimited signal is a signal which exhibits a zero power spectrum for frequencies $\nu > B$.

Sampling with a higher frequency than the Nyquist rate does not lead to any gain of information. When the sampling frequency is too low or the original signal is not band-limited then the reconstruction of the signal leads to non-linear imperfections which are called *aliasing* and cannot be reconstructed. When the sampling frequency is pre-determined, for example by the sampling method, the continuous function f is usually filtered before sampling in order to to eliminate high frequencies and avoid aliasing effects. An appropriate filter type is a lowpass filter which is referred to as an *anti-aliasing filter* in this context.

If the Nyquist–Shannon sampling theorem is not satisfied, the frequency components above f_{Nyquist} of the sampled signal cannot be distinguished from lower-frequency components mirrored at the sampling frequency which are then called *aliases*.

The Nyquist–Shannon sampling theorem is applicable to functions of time, where the term "frequency" has its original meaning, but also to functions of other domains, such as space (e.g. for a digital image). In the latter case, the units of measure of the frequencies has to be adapted accordingly.

3.2 Spectral analysis

The term *spectral analysis* refers to the process of identifying frequency components in data. Most often, spectral analysis is used to determine the frequency content of an analog (continuous) time signal $f(t)$. A frequently used strategy to perform spectral analysis is to sample the analog signal in a first step, then truncate the discretized data $f[n]$[2] with a window function (see section 3.3), and finally compute the DFT of the filtered data. The DFT $\hat{F}(k)$ of a signal $f(x)$ is complex-valued but the frequency spectrum is represented by the absolute value of the DFT.

3.3 Windowing

The main assumption of the discrete Fourier transform is that the input signal is finite and periodic. For many physical signals, such as images, the periodicity condition is not fulfilled. For such signals, a method to overcome this limitation is to assume a periodic extension of the signal. This leads to yet another problem: the spectrum is modified artificially, which is undesirable when one is interested in the "real", physical spectrum. Applying a *window function* to the signal before performing the DFT reduces this effect, although it cannot be avoided completely.

A window function is defined as follows:

---

[2] The discretized dataset usually consists of a finite set of uniformly spaced time-samples of the signal $f(t)$.

Definition 3.6 (Window Function)
In a narrow sense, a window function is a function which is exactly zero at the beginning and at the end of a data block (e.g. at the borders of an image) and outside the data blocks' domain. A broader definition allows the function to not assume identically zero in the data blocks' domain. In that case it is required that the product of the window multiplied by its argument is square integrable, and that the function approaches zero sufficiently fast (Cattani and Rushchitsky [2007]).

Depending on the exact shape of the window function, it affects the spectrum in a slightly different way. In general it is desired that the *frequency response*, i.e. the Fourier transform of the window function exhibits low amplitudes at side lobes. The window function is chosen with respect to the width of the central lobe as a trade-off between resolving frequencies (*high resolution window functions*[3]) or resolving the correct amplitudes in Fourier space (*high dynamic range window functions*[4]).

3.3.1 Hann Window

The Hann window is a window function named after Julius von Hann. It is also known as the Hanning window, von Hann window or raised cosine window and it is defined by

$$w(n) = \frac{1}{2}\left[1 - \cos\left(\frac{2\pi n}{N}\right)\right], \tag{3.5}$$

with $n = 0, \ldots, N-1$. One of the most important applications of the Hann window is the filtering of a signal prior to conversion to the frequency domain by performing a Fourier transform. The advantage of the Hann window compared to other window functions is the good frequency resolution and low spectral leakage. The drawback is the slightly reduced amplitude accuracy.

3.3.2 Spectral leakage and energy loss due to windowing

Due to the limited size and the non-periodicity of a typical signal a phenomenon called *spectral leakage* occurs after the DFT. All frequencies and wave numbers which do not occur in the basis of the DFT are not periodic in the image window. This results in discontinuities when the signal is periodically extended which in turn lead to the occurence of frequencies in the spectrum, which are not part of the original signal. Metaphorically speaking the "energy" of these frequencies is distributed onto the adjacent frequencies during the DFT, resulting in a leakage of energy to "wrong" frequencies. This effect is reducing by windowing.

In general, applying a window function to a signal leads to a reduction of the total power carried by the signal. This can be corrected by a normalization factor f which is multiplied with the spectrum, resulting in a correction of the amplitudes in

---

[3] small width of the main lobe leading to better frequency selectivity

[4] large width of the main lobe leading to the desired small side lobe amplitudes.

Fourier space. In this section, a general form of f is derived as well as the specific f for a Hann window in one and two dimensions.

According to Parseval's theorem (see definition 3.4) the energy density[5] E of a discrete signal S of length N in the spatial domain equals its energy density $\tilde{E}$ in the Fourier domain

$$E := \sum_{n=0}^{N-1} |S[n]|^2 = \frac{1}{N} \sum_{k=0}^{N-1} |\hat{S}[k]|^2 =: \tilde{E}. \tag{3.6}$$

This means that it is possible to apply a window to the signal in the spatial domain and to correct the amplitudes in the Fourier domain afterwards.

Assume a signal S with finite extent which is (pixelwise, denoted by $\star$[6]) multiplied by a window function W. Let $\langle \circ \rangle$ denote the ensemble average and $\bar{\circ}$ denote the time average (or the spatial average for spatial signals).

Assuming the ensemble average of the signal to be homogeneous, the ensemble average of the windowed signal is given by

$$\langle W \star S \rangle = \frac{1}{L} \int W \,\mathrm{d}x \cdot \langle S \rangle \tag{3.7}$$

with $\bar{W} = \frac{1}{L} \int W \,\mathrm{d}x$.

Since the squared signal is of interest for the energy density:

$$\langle W \star S^2 \rangle = \frac{1}{L} \int W \,\mathrm{d}x \cdot \langle S^2 \rangle \tag{3.8}$$

Now substitute $W = \tilde{W}^2$.

$$\langle \tilde{W}^2 \star S^2 \rangle = \frac{1}{L} \int \tilde{W}^2 \,\mathrm{d}x \cdot \langle S^2 \rangle \tag{3.9}$$

$$\parallel$$

$$\langle (\tilde{W} \star S)^2 \rangle = \frac{1}{L} \int \tilde{W}^2 \,\mathrm{d}x \cdot \langle S^2 \rangle \tag{3.10}$$

For a 1D-Hann window $\tilde{W} = w(x) = 0.5 \left(1 - \cos\left(\frac{2\pi \cdot x}{L}\right)\right)$ the term $\frac{1}{L} \int \tilde{W}^2 \,\mathrm{d}x$ in

---

[5] Technically, the terms *energy*, *energy density* and *power* have to be taken with care. In the language of signal processing, the signal S usually is a function of time which results in $\langle S^2 \rangle$ describing a *power* spectrum which is a function of frequency ω and has the dimension of $\frac{\text{energy}}{\text{time}}$. For application on images, the signal S is a spatial signal. Thus $\langle S^2 \rangle$ describes the *energy density* spectrum as a function of wave number $\vec{k}$. The corresponding dimension is $\frac{\text{energy}}{\text{area}}$.

[6] For two matrices A, B of the same dimension $m \times n$ the Hadamard product or pixelwise product $A \star B$ is the matrix of the same dimension as the operands with elements given by $(A \star B)_{i,j} = (A)_{i,j} \cdot (B)_{i,j}$.

Equation 3.10 can be evaluated as

$$\begin{aligned} f_{Hann1D} &:= \frac{1}{L}\int_0^L \tilde{W}^2\,\mathrm{d}x = \frac{1}{L}\int_0^L \left(\frac{1}{4}\left(1-\cos(\frac{2\pi}{L}\cdot x)\right)^2\right)\mathrm{d}x \\ &= \frac{1}{4L}\int_0^L \left(1 - 2\cdot\cos(\frac{2\pi}{L}x) + \cos^2(\frac{2\pi}{L}x)\right)\mathrm{d}x \\ &= \frac{1}{4L} = \left[x - \frac{2L}{2\pi}\sin(\frac{2\pi}{L}x) + \frac{x}{2} + \frac{L}{8\pi}\cdot\sin(2\cdot\frac{2\pi}{L}x)\right]_0^L \\ &= \frac{3}{8} \end{aligned} \tag{3.11}$$

For a 2D-Hann window $\tilde{W} = w(x){\cdot}w(y) = 0.5\,\left(1-\cos\left(\frac{2\pi\cdot x}{L_x}\right)\right){\cdot}0.5\,\left(1-\cos\left(\frac{2\pi\cdot y}{L_y}\right)\right)$ a similar calculation results in

$$f_{Hann2D} := \frac{1}{L_x\cdot L_y}\int_{(0,0)}^{(L_x,L_y)} \tilde{W}^2\,\mathrm{d}x\,\mathrm{d}y = \left(\frac{3}{8}\right)^2 = \frac{9}{64} \tag{3.12}$$

Then the correctly normalized signal is given by $\langle S^2\rangle = \frac{64}{9}\langle(\tilde{W}\star S)^2\rangle$ and for a 3D-Hann window and 3D signal it is $\langle S^2\rangle = \frac{512}{27}\langle(\tilde{W}\star S)^2\rangle$.

Part II.

Methods

4

The Imaging Slope Gauge (ISG) as a technique to measure water wave surface slopes

This chapter outlines the most important techniques which are used to measure water wave surface slopes. An overview of the existing techniques available for measuring the geometrical properties of water waves is given in Figure 4.1. Furthermore this chapter explains the underlying foundations as well as the limitations of the different methods. Finally, the characteristic features of the Imaging Slope Gauge are described in more detail.

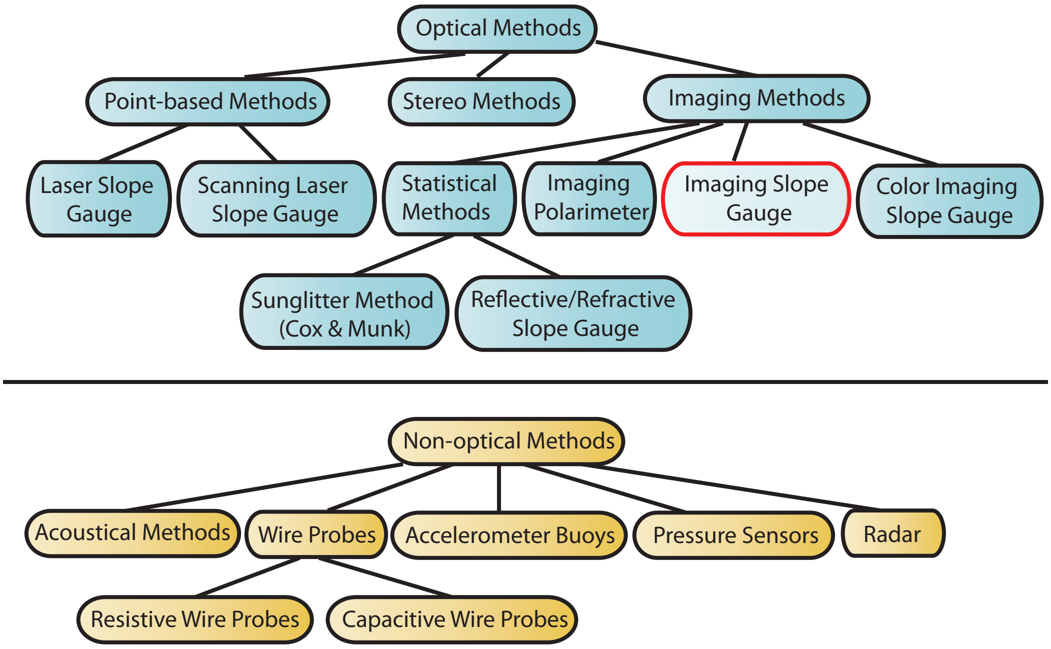

Figure 4.1.: Overview of a selection of the existing techniques for measuring geometrical properties of the sea surface. Adapted from Lauer [1998].

4.1 Slope measurements vs. height measurements

When measuring geometrical properties of water waves two main approaches can be distinguished: *slope measurements* and *height measurements*. Both techniques are in principal equivalent because it is possible to obtain height information from slope measurements via integration at the cost of the mean surface elevation. This is feasible because water wave surface slopes are the gradient of surface elevation. A short description of this equivalence is given in Jähne and Schultz [1992].

One important difference between the two approaches is due to the fact that water wave surface slope measurements require the acquisition of two slope components at the same time whereas height measurements - as surface elevation is a scalar quantity - do not. This makes water wave surface slope measurements technically more demanding. On the other hand the wave height displays a rather large variation depending on wave length whereas the variability of wave slopes is almost constant for a broad range of wave lengths (Jähne and Schultz [1992]). This is the main reason why this thesis is focused on water wave surface slope measurements.

In principle, two different types of techniques for measuring water wave surface slopes and heights are available, *optical methods* and *non-optical methods*. Non-optical techniques include measurements of the wave amplitude using capacitive or resistive wire probes, pressure sensors or accelerometer buoys. Conventional *stereophotogrammetric methods* (Laas [1905, 1906]; Kohlschütter [1906]; Laas [1921]; Schuhmacher [1939]) are an example for optical techniques used for height measurements. It has been shown that they exhibit insufficient height resolution for small waves (see Fuß [2004]).

4.2 Methods for water wave surface slope measurements

In this chapter, the focus lies on optical techniques for measuring water wave surface slopes as most non-optical methods interact with the wave field and are not suitable for measuring capillary waves due to this limitation. Optical methods for measuring water wave surface slopes are based on the principle of either refraction (Cox [1958]; Hughes et al. [1977]; Jähne and Riemer [1990]; Zhang and Cox [1994]) or reflection (Cox and Munk [1954a,b]; Stilwell [1969]).

Jähne et al. [1994] gives a detailed review of the advantages and disadvantages of the different optical techniques for measuring water wave surface slopes. Their areas of application can be summarized as follows:

Reflection-based methods are particularly useful for field measurements. Methods such as the Stilwell technique (Stilwell [1969]) require a homogeneous illumination of the sky, suffer from a large degree of nonlinearity between intensity and water wave surface slope.

Refraction-based methods can resolve small structures on the water surface and are applicable over a broad range of wave lengths with a rather small degree of nonlinearity.

4.2.1 Reflection-based Methods

Reflection-based methods including Stilwell photography (Stilwell [1969]) are particularly suitable for field measurements since no equipment has to be submerged into the water. Thus, the wave field remains undisturbed. However, as mentioned before, Jähne et al. [1994] have demonstrated that these techniques perform satisfactorily for a rather narrow slope range only.

Reflection-based methods found on the fact that the water surface reflects light according to the reflection condition: the viewing angle α relative to the surface normal equals the angle of incidence β of a light ray. This is illustrated in Figure 4.2a. From the positions of all reflexes in a series of images the slope distribution of the surface can then be determined.

Sun Glitter Method by Cox and Munk Cox and Munk [1954a,b] are known for the first successful application of this principle in order to acquire statistical water wave surface slope data in field measurements. The glitter of the sun on the sea surface is photographed from a plane. When the reflection condition is fulfilled a reflex is visible on the photo. Since the reflex condition varies depending on the position in the image a slope can be assigned to each position. From this, a distribution of the sun glitter can be obtained which allows for the computation of the water wave surface slope distribution. A theoretical study of the patterns of the specular reflexes which are observed on a randomly moving surface was performed by Longuet-Higgins [1960].

Stilwell Method The Stilwell method which is named after Stilwell [1969] is an extension of the method of Cox and Munk [1954a,b]. It makes use of the diffuse scattered light of the sky which acts as a light source with infinite extent. With the assumptions of a quasi-uniform radiance of the sky and an optimal geometry of the imaging system Barber [1949]; Stilwell [1969] showed that the optical spectrum of an image of the water surface is linearly related to the water wave surface slope spectrum[1]. This model has been extended to second order by Kasevich [1975] which allows to describe the quality of the linearity.

Limitations Measurement techniques based on reflection are theoretically limited to slopes between ±1 due to the doubling of angles by reflection (reflex condition)[2] (Jähne and Schultz [1992]).

Another important limitation of reflection-based techniques - apart from the restriction to a narrow range of slopes - is the low reflectivity of the water surface for small angles of incidence[3] as well as the disturbances introduced by light that penetrates the surface and experiences backscattering[4].

Jähne et al. [1994] also showed that the nonlinearities between measured intensities and water wave surface slopes are significantly larger for reflection-based techniques than for refraction-based methods. Reflection-based techniques are highly demanding in terms of the required size of the light source. Thus they are not easily usable with artificial light sources which is another reason why techniques based on refraction are preferred for laboratory measurements.

---

[1] for small wave slopes.

[2] Practically, this would require a light source of infinite extent.

[3] The reflectivity of a smooth water surface is less than 5 % for angles of incidence smaller than 50° [Bigg, 2003]

[4] so-called upwelling light

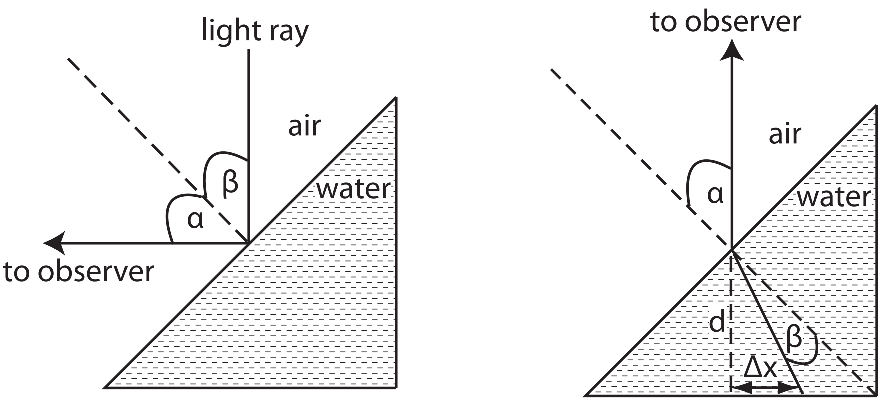

(a) Reflection of light at the water surface

(b) Refraction of light at the water surface

Figure 4.2.: Comparison of light reflection (4.2a) and refraction (4.2b) at the water surface. The reflection condition for 4.2a is $\alpha = \beta$ whereas the refraction condition for 4.2b given by Snell's law reads $n_a \cdot \sin\alpha = n_w \cdot \sin\beta$ with refractive indices for air (n_a) and water (n_w), respectively. In the case of refraction it is possible to determine the slope of the surface from the measured deflection $\Delta x = d \cdot \tan(\alpha - \beta)$.

4.2.2 Refraction-based Methods

Refraction-based methods are particularly useful for water wave surface slope imaging because they are capable of measuring large slopes and exhibit a large degree of linearity over a large range of slopes.

The fundamental principle of refraction based techniques is the deflection of light at the air-water interface according to Snell's law: A light ray which enters an interface (here: air-water interface) with an angle of incidence α relative to the surface normal is refracted at the interface such that

$$n_a \cdot \sin\alpha = n_w \cdot \sin\beta \tag{4.1}$$

with an angle of refraction β and refractive indices for air (n_a) and water (n_w), respectively (see Figure 4.2b). If the variations of water height are negligible ($h \approx$ const.), the deflection $\Delta x = d \cdot \tan(\alpha - \beta)$ of the light ray at the bottom of the water body can be used to determine water wave surface slope.

Method of Cox The first application of refraction for water wave surface slope measurements was described by Cox [1958] who placed a glass wedge filled with ink below a wave tank and illuminated it uniformly from below. Seen from above this results in a logarithmic decrease of brightness in one direction. Using a photometer, the brightness of a point on the water surface can be measured and be related to the corresponding component of water wave surface slope.

For this technique the main source of error is due to the neglect of large height variations for higher wind speeds which result in an error in the slope data. Apart from that the measured intensity depends on curvature and slope as well. Nevertheless the method served as a starting point for further development. Wu [1977] extended this technique such that it is capable of measuring the curvature distribution of water waves. Wright and Keller [1971] extended the method of Cox to an imaging technique that is capable of measuring one component of water wave surface slope in a confined area.

Laser Slope Gauge Another frequently used technique that can be used for water wave surface slope measurements at a single point is the Laser Slope Gauge (LSG). It consists of a laser beam which is refracted at the air-water interface according to Snell's law depending on the surface slope. It is detected using a position-sensitive optical receiver. This method can only yield a slope value for one point of the surface. Among others, Prettyman and Cermak [1969]; Long and Huang [1976] have applied this technique.

Later the method has been extended by scanning the laser beam across the surface in one or two dimensions – the so called Scanning Laser Slope Gauge (SLSG) Bock and Hara [1995, 1992b,a]; Hwang [1995].

4.3 Concepts of the Imaging Slope Gauge (ISG)

The Imaging Slope Gauge (ISG) is a refraction-based method for measuring water wave surface slopes. It was used for the measurements which were conducted for this thesis. The specific setup that was used for the measurements is depicted in Figure 5.4 and explained in section 5.2. Here, only the general concept of the ISG is illustrated.

Historically, the Imaging Slope Gauge was first mentioned by Wright and Keller [1971][5] and described by Keller and Gotwols [1983]. Zhang and Cox [1994] used a Color Imaging Slope Gauge (CISG) to measure water wave surface slope from the deflection of refracted light. A 2d-color scheme was installed as light source which encodes both slope components as a specific color value. Balschbach [2000] used a similar method to determine various statistical and geometrical properties of water waves. His experimental setup consists of a color CCD camera which is focused

---

[5] Although the system presented was not referred to as Imaging Slope Gauge in the original article.

on the mean water height and an illuminated color gradient below a fresnel lens which itself is installed below the water tank which ensures a unique relationship between color and water wave surface slope. For field measurements (e.g. [Klinke, 1996]), Jähne et al. [1994] demonstrate that it is preferrable to submerge the light source and install the camera on the air side because this setup ensures smaller nonlinearities. Jähne and Schultz [1992] describe the calibration and explore the accuracy of different ISG setups.

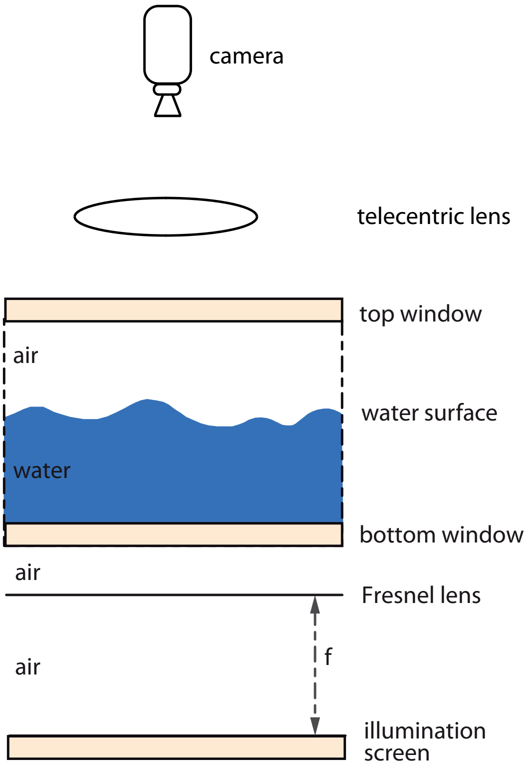

Figure 4.3.: 1D simplified view of an ISG setup. Image modified after Kiefhaber et al. [2014].

The ISG at the Heidelberg Aeolotron is based on a so-called *telecentric illumination* in combination with *object-space telecentric optics*. Figure 4.3 depicts the basic components of an ISG setup. A camera is placed on top of the water surface such that the aperture is positioned in the focal point of a large "telecentric lens" which itself is placed in between the camera and the water surface. This guarantees that only those light rays which leave the water surface parallel to the optical axis are refracted onto the image sensor of the camera and that all rays which enter the telecentric lens parallel to the optical axis are correctly focused onto the sensor of the camera. The optical axis is oriented perpendicular to the flat water surface. This way the large lens in combination with the camera aperture yield object-space telecentricity which implies a constant magnification factor independent of object distance. The setup is aligned such that the mean water surface is positioned in the second focal plane of the large lens. Underneath the bottom window of the wind/wave facility, a large Fresnel lens is placed in the air space between the bottom window and the illumination source installed at the very bottom. For an ideal setup, the distance between the Fresnel lens and the illumination source equals the focal length of the Fresnel lens. The Fresnel lens guarantees telecentric illumination, i.e. that all rays that leave the lens under an angle δ relative to the optical axis have the same point of origin on the illumination screen.

Thus, the setup provides a unique relation between the point of origin of the light rays which enter the camera for each pixel and the corresponding water surface slope $\tan\alpha$. This relation is independent of the position on the water surface and of the height of the waves. As shown in Jähne et al. [1994], the relation is almost linear. Yet it remains to identify the point of origin of the light that enters the camera aperture.

When measuring one slope component only it is sufficient to have an intensity gradient in the direction in which slope is supposed to be measured. For two dimensions the idea of the color imaging slope gauge (CISG) described in the previous section is to use an RGB camera and a color-coded light scheme. Then two of the color gradients can be used for position coding and the third color channel can be applied for normalization as well as the correction of disturbing effects such as those induced by lens curvature. A significant disadvantage of this method is the chromatic aberration of the telecentric lens which leads to misalignments of the different color components (see [Kiefhaber, 2014]).

Another approach, which is used for this thesis, is applicable with a high speed monochrome camera and a programmable light source which is capable of switching between different states in short time. The underlying idea of this approach is to implement four different brightness gradients A, B, C, D in the alongwind directions x and -x as well as the crosswind directions y and -y (see Figure 4.4). Then normalized intensities I_x and I_y can be computed from two intensity gradients in opposite directions in x- and y-direction, respectively:

$$I_x = \frac{A - B}{A + B} \text{ and } I_y = \frac{C - D}{C + D} \tag{4.2}$$

The combination of both components (I_x, I_y) makes it possible to identify the origin of the light rays on the illumination source from the camera images uniquely. The usage of normalized intensities is referred to as *ratio imaging* and it has the significant advantage that small imperfections, for example in the bottom window and the light source, are automatically compensated.

Between 2009 and 2011 Roland Rocholz constructed a CISG setup at the Heidelberg Aeolotron. It was used during several experiments to conduct research on air-water gas exchange (Krall [2013], Kräuter [2011]). Based on this setup, the new ISG setup was constructed in 2013.

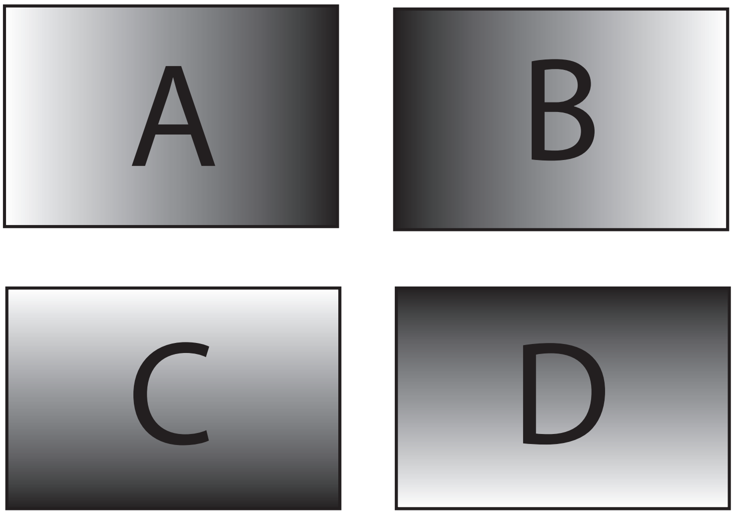

Figure 4.4.: Light source intensity gradients (A,B,C,D) for an ISG setup.

4.3.1 Advantages and Limitations of an ISG setup

For the approach using the brightness gradients A, B, C, D as described it is impossible to determine both slope components from one image which is the reason why a high speed camera in combination with fast electronics for the light source are necessary in order to reduce the time between two consecutive images to a minimum. The main advantage of this approach compared to a CISG setup is the possibility to avoid chromatic aberration. At the same time, the demand for homogeneity of the light source is reduced due to ratio imaging.

Since the ISG is a refraction-based technique either the camera or the light source have to be submerged into the water[6]. Although this has been tried in the field ([Klinke, 1996]) the ISG is mainly used in laboratory applications.

The footprint on the water surface is restricted by the size of the large telecentric lens because of the geometry of the light rays for the telecentric setup. The measurable slope range depends on the size of the light source and the optical components[7]. Wave height cannot be determined from ISG data directly, since slopes are measured. In simple terms, as slopes are the gradient of height, the reconstruction of wave height is possible by integration up to an additive factor. This leads to the requirement of additional instruments to measure the water height at one point at least. Yet the ISG is ideally suited to study small-scale waves and their dynamics in a laboratory setup.

---

[6] This is true at least for field measurements; it is avoidable in the lab depending on the construction of the wave channel.

[7] For the current data evaluation method at the Heidelberg Aeolotron it is in fact as well limited by the range of slope values available in the calibration target, see section 8.2.

4.3.2 Ray Geometry of the ISG Setup

In order to understand the ISG setup and to evaluate the data the relation between water surface slope and the position on the light source is described in this section.

Consider the trace of a light ray from the camera on top of the setup to the illumination source underneath the bottom of the wind/wave facility as it is shown in Figure 4.5. The light rays which are focused on the image sensor have been refracted at the water surface according to Snell's law (equation (4.1)). In order to leave the water surface under an angle α relative to the water surface normal (i.e. parallel to the optical axis) they have to pass the water under an angle γ relative to the optical axis. At the faces of the (thick) bottom window the ray is refracted twice, leading to a small displacement and a change of the angle.

As described in Rocholz [2008] a light ray that leaves the light source with the angle δ enters the camera if and only if

$$\vec{s} = \begin{pmatrix} s_x \\ s_y \end{pmatrix} = \begin{pmatrix} \cos\Phi \\ \sin\Phi \end{pmatrix} \cdot \frac{|\tan\delta|}{\sqrt{n_w^2 + (n_w^2 - 1)\tan^2\delta} - \sqrt{1 + \tan^2\delta}}, \tag{4.3}$$

where the water wave surface slope is given by $\vec{s}$, $n_w \approx 1.33$ is the refractive index of water and Φ denotes the polar angle of the light ray.
Denoting the deviation of the examined light ray from the origin on the light source which is given by the principal axis of the fresnel lens as

$$\begin{pmatrix} \Delta x \\ \Delta y \end{pmatrix} = \sqrt{(\Delta x)^2 + (\Delta y)^2} \cdot \begin{pmatrix} \cos\Phi \\ \sin\Phi \end{pmatrix}, \tag{4.4}$$

and using the definition of

$$|\tan\delta| = \frac{\sqrt{(\Delta x)^2 + (\Delta y)^2}}{f}, \tag{4.5}$$

with the focal length of the telecentric Fresnel lens f, the relation between water surface slope $\vec{s}$ and the position on the light source $(\Delta x, \Delta y)$ is obtained:

$$\vec{s} = \begin{pmatrix} s_x \\ s_y \end{pmatrix} = \begin{pmatrix} \Delta x \\ \Delta y \end{pmatrix} \cdot \frac{1}{\sqrt{f^2 n_w^2 + (n_w^2 - 1)((\Delta x)^2 + (\Delta y)^2)} - \sqrt{f^2 + ((\Delta x)^2 + (\Delta y)^2)}}. \tag{4.6}$$

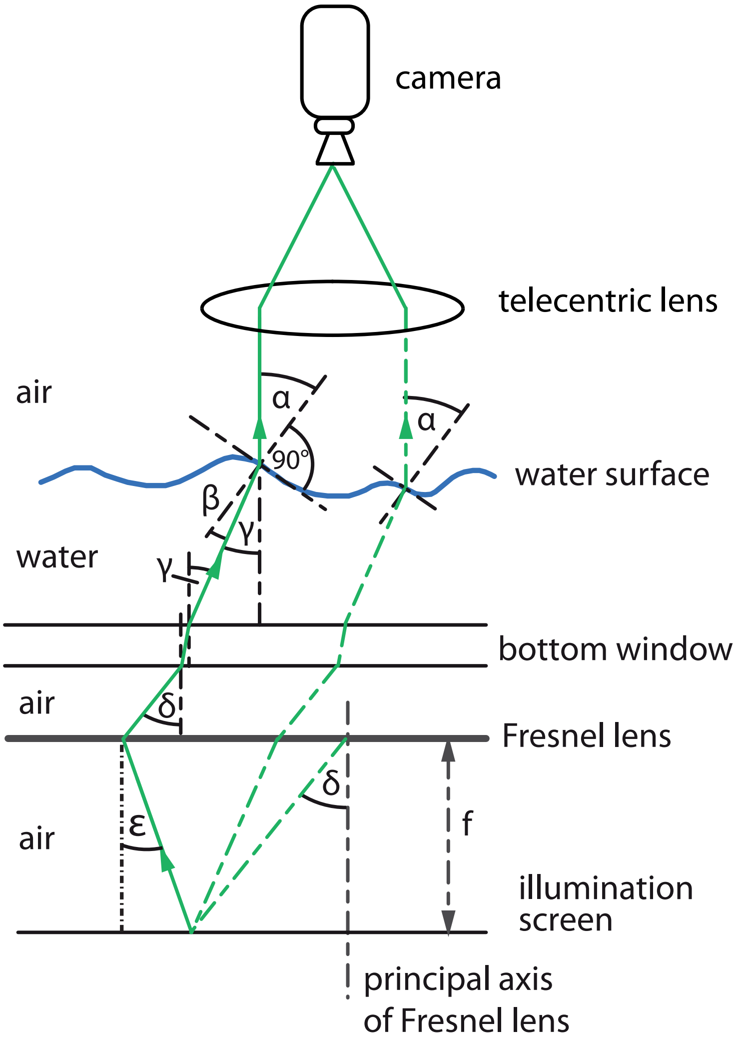

Figure 4.5.: 1D simplified view of the light ray geometry of the ISG setup. Image modified after Kiefhaber et al. [2014].

5

Experimental Setup

All experiments described in this thesis were conducted in the Heidelberg wind/wave facility "Aeolotron" which is characterized in section 5.1. After that, in section 5.2 the measurement setup of the Imaging Slope Gauge at the Aeolotron is specified. Then the technical details of the high speed camera (section 5.3) and the custom-made programmable and high-power LED light source (section 5.4) integrated into the setup are described. The double-sided telecentric imaging setup at the Aeolotron allows to sample waves up to high-frequency capillary waves. Due to the high-speed camera this can be done without noticeable aliasing. Finally, in section 5.6 the calibration targets used for the experiments are specified in detail.

5.1 The Heidelberg Wind/Wave Facility "Aeolotron"

The Aeolotron in Heidelberg is an annular wind/wave facility which was constructed for the analysis of air-water interaction processes (exchange of mass, momentum, and heat). The measurements performed here include measurements of the exchange of volatile substances as well as the application of imaging techniques for the analysis of the wave field or heat exchange. The Aeolotron has an inner diameter of ≈8.7 m and a mean circumference of 29.2 m at the inside wall. A photographic view into the flume of the facility is provided in figure 5.1. It consists of a ring shaped water flume of approximately 61 cm width and a height of 2.41 m and is parted into 16 segments. Since the first description in Jähne et al. [1999] it has been modified during several periods of construction work which includes a new design for wind generation. Two axial fans mounted onto the ceiling of the tank in sections 4 and 12 (Figure 5.3) are used to generate wind. Typical wind speeds during past experiments reach up to approximately 10 m/s (at the usual tank filling of 1.0 m, see Krall [2013]). In addition,

Figure 5.1.: The Aeolotron: Photographic View into the facility. The wind is blowing from right to left.
Photo: AEON Verlag & Studio, Hanau 2010.

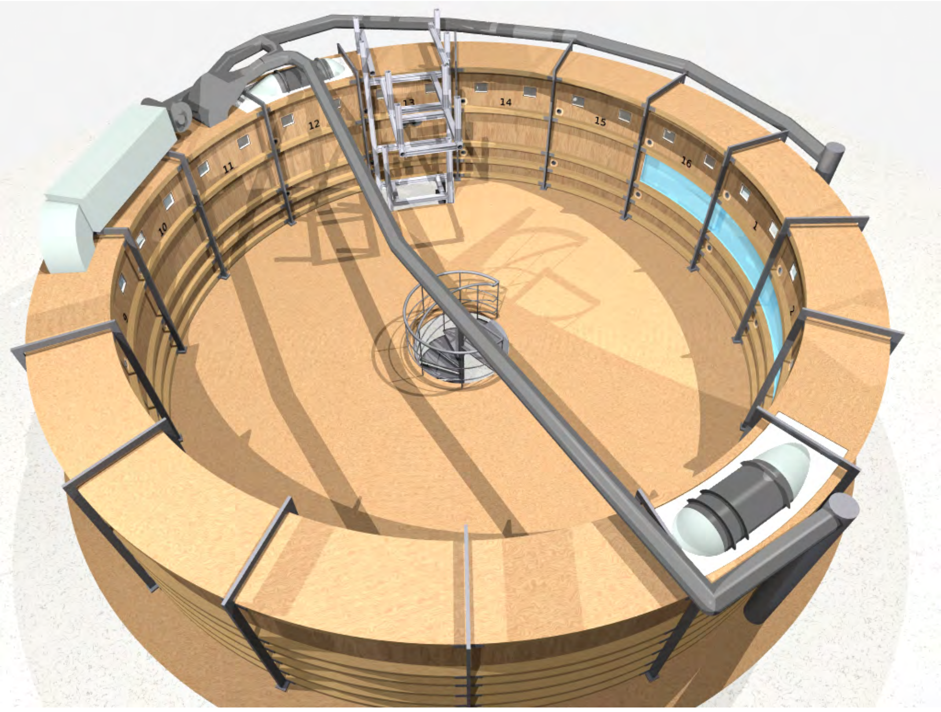

Figure 5.2.: Rendered view of the Aeolotron with new system for wind generation. Wind is generated such that the air is flowing counter-clockwise. The ISG is mounted at segment 13 which can be identified in the picture by the framework for the installation of optical setups in light grey. Image taken from Krall [2013].

the facility is equipped with a counter current pump. Figure 5.2 shows a rendered view of the facility with the new system for wind generation.

Experiments are typically conducted with deionized water at a water depth of about 1.0 m, which corresponds to a water volume of about 18.0 m^3. The air space then comprises about 24.4 m^3. The Aeolotron is thermally isolated and mostly gastight. Ambient parameters such as wind speed, temperatures in the water and in the air space and humidity can be measured at reference positions in segments 15 (wind speed measurements with a fan-anemometer; temperature measurements with two Pt-100 temperature sensors) and 2 and 13 (humidity sensors). In addition, the water height can be determined with a ruler.

In Krall [2013], the gas concentration measurement system is described. It contains two spectrometers one of which is used for direct air side concentration measurement. Furthermore, it consists of a pump installed in segment 6 which is connected to a membrane oxygenator for water side gas concentration measurement. The oxygenator is used to equilibrate the gas concentration in the water with an air parcel which can then be pumped into a FT-IR spectrometer for analysis via infrared spectroscopy. The sampling location for air side concentration measurements is in segment 2. From the gas concentration data, transfer velocities can be calculated.

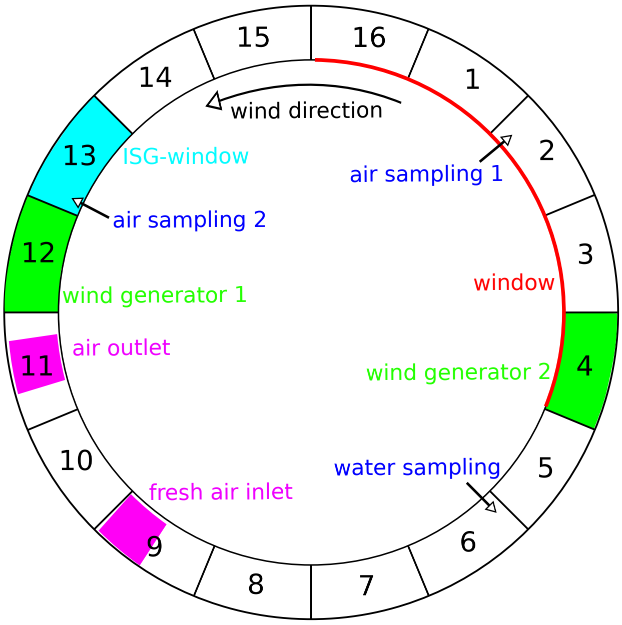

Figure 5.3.: Schematic view of the Aeolotron explaining the segment numbering scheme. The ISG window is installed in segment 13, segments 16 and 1-4 contain a large window which allows for direct visual access. The positions of the two wind generator fans, the sampling locations as well as the fresh air in- and outlets are shown as well. Image taken from Krall [2013].

A disadvantage of annularly shaped flumes are the inertial forces which occur when the water body is moving. They give rise to the formation of secondary flow, i.e. flow which is less strong than the primary flow in wind direction but which is oriented perpendicular to it. The secondary flow is superimposed on the primary flow and leads to changes of the properties of the total flow due to the geometry of the facility only (Bopp [2014]; Ilmberger [1981]). Another restriction which occurs due to the geometry of the flume is the reflection of waves at the walls which leads to conditions different to those on the open ocean.

However, another fact makes the conditions in the Aeolotron more similar to an open water situation like the ocean than the conditions in a linear wind-wave channel are. Due to the annular shape of the flume the fetch[1] is quasi unlimited and a stationary wave field can evolve. In contrast to linear facilities, the physical conditions are independent from the position of the measurement device due to the circular geometry of the flume. Furthermore, in contrast to linear facilities, there is no need for a wave absorber.

5.2 ISG

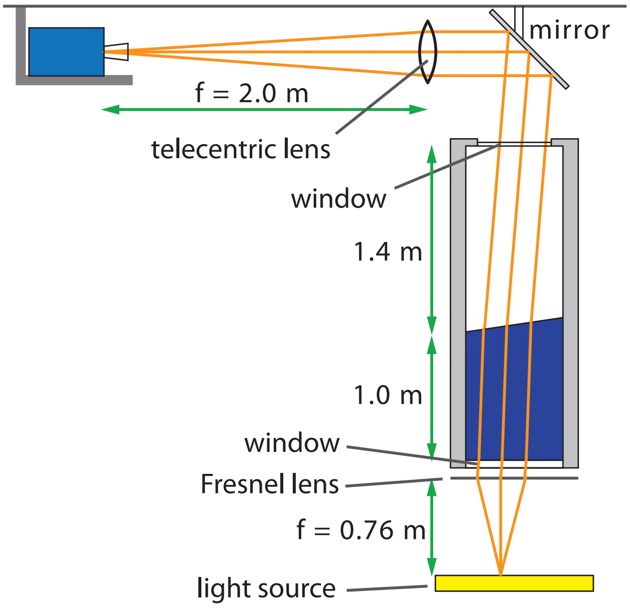

Figure 5.4.: Wave imaging setup at the Aeolotron. Image modified after Kiefhaber et al. [2014].

The imaging setup at the Heidelberg Aeolotron is depicted in figure 5.4. The water body is illuminated from below with a programmable light source (see section 5.4) through a window made from 4 layers of Lexan®polycarbonate sheets and high-impact acrylic[2] with a total thickness of 3.2 cm. In between the bottom window and

---

[1] The term *fetch* describes the length on which the wind acts on the water surface.

[2] Lexgard®RS-1250 laminate [General Electric Plastics]

the light source a large Fresnel lens with a focal length of $f_f = 0.762\,\mathrm{m}$ and a diameter of $d_f = 0.89\,\mathrm{m}$ is placed in order to ensure "telecentric illumination". The latter is defined by the following property: as the light source is positioned in the focal plane of the Fresnel lens all rays that leave the light source at a common position will be parallel to each other after passing the Fresnel lens. A tilted mirror is fixed above the top window of the facility. The mirror directs the light rays into a planoconvex lens made from BK7 with a diameter of $d = 0.32\,\mathrm{m}$ and a focal length of $f = 2\,\mathrm{m}$ (see Figure 5.5). Both the mean water surface and the aperture of the lens of a high speed camera (decribed in section 5.3) are placed in the focal planes of the planoconvex lens. This way an object space telecentricity is achieved which ensures that all light rays which are focused on the image sensor of the camera have been parallel to the optical axis before entering the "telecentric" lens. The setup is constructed such that the light rays which enter the camera leave the (flat) water surface normal to it. This is achieved by placing the aperture of the camera lens in the focal plane of the telecentric lens. By this means changes in the size of imaged structures due to varying distances to the image sensor because of the waves can be avoided. This is important because the height[3] of the waves at the Aeolotron can reach more than 60 cm at high wind speeds. The accuracy of the imaging system is explored in detail in section 8.3.

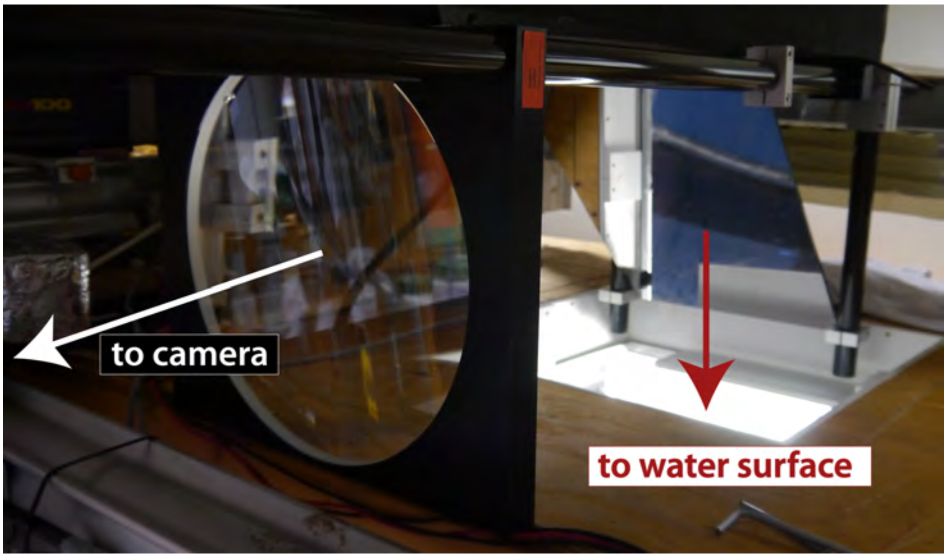

Figure 5.5.: Wave imaging setup at the Heidelberg Aeolotron: telecentric lens and tilted mirror.

---

[3] Height is meant here as the vertical distance between wave crest and wave trough.

5.3 Camera and Lenses

Figure 5.6.: pco.dimax camera used in the ISG setup.

In our setup a monochrome pco.dimax high speed CMOS camera (PCO AG) was used (figure 5.6). Data was acquired with a spatial resolution of 960 x 768 pixel at a frame rate of 6030 fps. The resulting effective frame rate for slope measurements is one fourth of this value, 1507.5 fps, because four raw images are required to compute a complete 2D wave slope image (see chapter 7). The measurements of 2014 were performed with f-number 8 and a Zeiss lens with f = 100 mm. This equals a footprint on the water surface of 227 × 182 mm corresponding to 0.24 mm per pixel.

For the 2013 measurements a Nikon lens with f = 105 mm was used with f-number 5.6. For the measurements with the Nikon lens the footprint on the water surface is 203 × 166mm which corresponds to a pixel size of 0.22 mm in object space. For each raw image, integration time is 140 µs. A summary of the most important technical data of the pco.dimax camera is given in Table 5.1.

Table 5.1.: Technical data of the pco.dimax high speed camera; taken from PCO.

sensor type	CMOS
full resolution (hor x ver)	2016 x 2016 pixel
pixel size (hor x ver)	11 µm x 11 µm
shutter mode	global
spectral range	290 nm . . . 1100 nm
quantum efficiency	50 % @ peak
maximum frame rate (full resolution)	1279 fps
frame rate (@ 960 x 768 pixel)	6030
exposure/shutter time	1.5 µs . . . 40 ms
dynamic range	12 bit
internal RAM	36 GB
data interface	GigE, USB2.0, CameraLink

5.4 Light Source

The custom-made programmable light source which is used for the experiments consists of a total of 1704 red high-power LEDs (Cree XLamp XP-E red) which have a peak wavelength at 630 nm and a maximum continuous current of 700 mA. For ISG application, they are operated in Flash mode as described below. They are positioned in 35 columns with 24 LEDs each in alongwind direction and 24 rows with 36 LEDs each in crosswind direction. For each row or column, the corresponding LEDs are placed at a distance of 2.1 cm and are wired in series. Figure 5.7a shows a photographic view of the light source with the LEDs. Custom electronics is used in order to control the LED currents between 0 mA and 1000 mA with a resolution of 12 bit separately for each row and column. Fast multiplexer units allow for a fast swapping between preprogrammed brightness gradients (A,B,C,D) as depicted in Figure 5.7c. Details of the electronics are given in Fahle [2013].

In order to create a homogeneous luminance gradient an acrylic diffusing screen is placed on top of the LEDs at a distance of 4 cm. Figure 5.7b shows the light source with the diffusing screen on top.

For the 2013 measurements the maximum LED current was 100 mA for both directions. For the 2014 measurements, the maximum LED current has been raised to 300 mA. This leads to higher light intensities which allows for measurements with smaller f-number.

For ISG measurements, the light source is programmed as follows: The four preprogrammed brightness gradients (A,B,C,D) are activated one after another with a frequency of $f_{ISG} = 6000\,\mathrm{Hz} \mathrel{\widehat{=}} \delta t = \frac{1}{f_{ISG}} = 0.167\,\mathrm{ms}$ (see Figure 5.8). This is referred to as a *subsequence* for the rest of this thesis. A variable number Q of these subsequences is activated with a temporal distance of $\delta T = 4 \cdot \delta t = 0.667\,\mathrm{ms}$, leading to $Q \cdot 4$ (temporally) equally spaced illumination gradients being activated after another and forming one ISG illumination *sequence*. P of these sequences are recorded with a frequency of $f_{Seq} = \frac{1}{\Delta T}$. The time during which each individual illumination gradient is active is given by $\Delta t = 0.140\,\mathrm{ms}$. Thus the duty cycle D' is calculated as follows: $D' = \frac{\Delta t}{\delta T} = \frac{0.140\,\mathrm{ms}}{0.667\,\mathrm{ms}} = 21\%$.

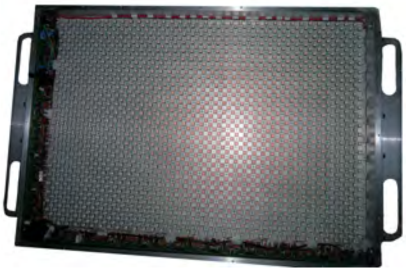

(a) Photograph of the light source without acrylic diffusion screen showing the LED rows and columns.

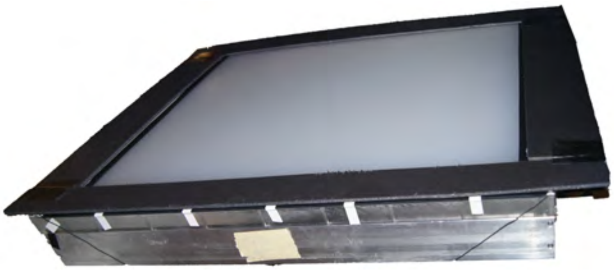

(b) Light source with acrylic diffusing screen.

(c) Schematic view of the light source. Image taken from Kiefhaber et al. [2014].

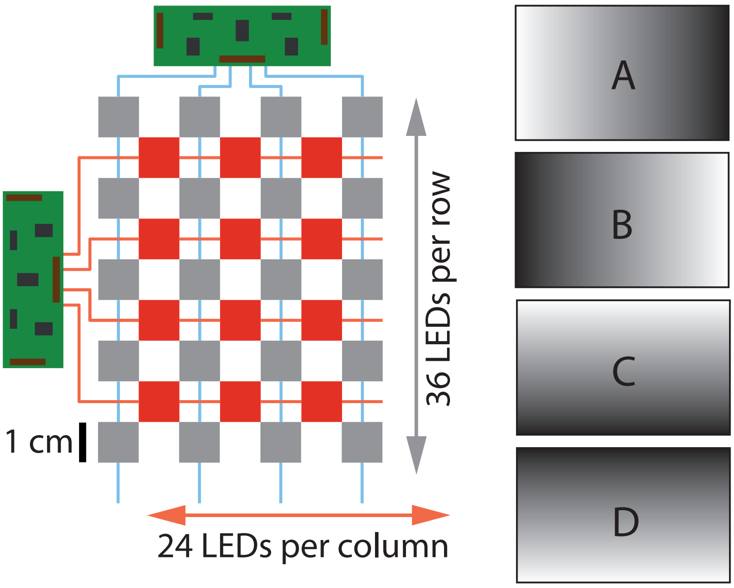

Figure 5.7.: The ISG light source which is used for illumination.

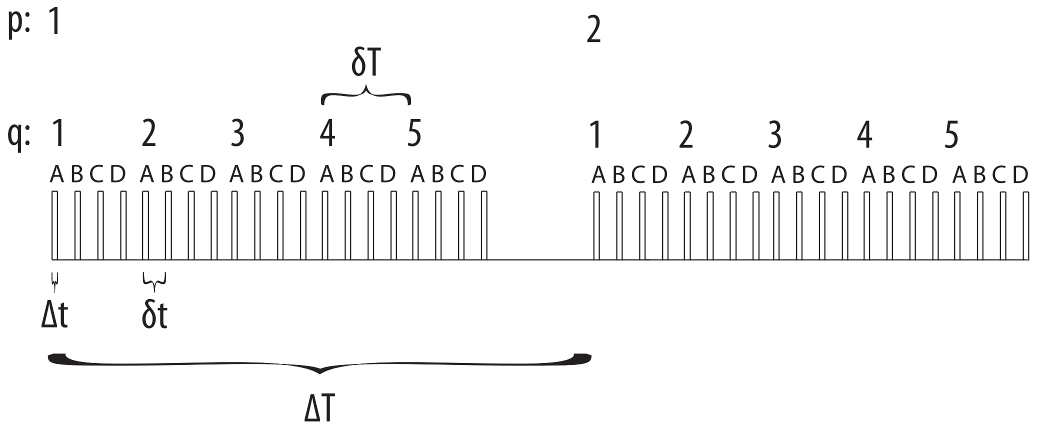

Figure 5.8.: Example for two consecutive ISG illumination sequences consisting of five subsequences each. With the nomenclature introduced in section 5.4 P=2 and Q=5 for this example. Each subsequence consists of each of the illumination brightness gradients A,B,C,D as depicted in Figure 5.7c. Each gradient is active for a time Δt, the time between the beginnings of two consecutive gradients is δt and the time between the beginnings of two consecutive sequences is ΔT.

5.5 Coupling of Light Source and Camera

The light source and the camera have to be coupled in order to obtain one camera image per illumination gradient. This is done in two different ways depending on the experiment. The first one is *internal triggering*. Here the camera is set to record images with a frequency of f_{ISG}. The camera trigger output signal is then used to trigger the light source electronics which is programmed to switch between the four illumination gradients consecutively. For the experiments conducted during this study, internal triggering was used to measure long image sequences (20000 raw images). The second method is *external triggering* where an external function generator is used to trigger camera, light source and possibly other measurement devices. External triggering was used for statistical measurements, where each sequence contains 20 raw images recorded with a frequency of f_{ISG}. The time interval between individual sequences is controlled by the external trigger signal.

5.6 Calibration targets

Several *calibration targets* are used for the experiments performed for this thesis. They are constructed such that they can float on the water surface and can be imaged with the ISG setup. A graphical overview of the targets is given in Figure 5.9 with schematic drawings of each target on the left hand side.

5.6.1 Lens float target

The lens float target consists of 24 planoconvex lenses made from BK7 glass[4] with a diameter of $d = 50\,\mathrm{mm}$ and a radius of curvature of $R = 51.68\,\mathrm{mm}$. The lenses are glued into the bottom of a float, leading to a small portion of the lenses being hidden. The "real" visible radius is analyzed in section 8.3.2. Figure 5.9a shows a schematic drawing of the lens float target; a photograph is given in the same figure. Figure 5.10 depicts a single lens floating on the water surface together with the corresponding ray geometry for a light ray entering from the water side. Because the lenses consist of a material with a different refractive index than that of water the light ray is refracted at the water-lens interface and at the lens-air interface. This leads to a change of the angle under which the light ray enters the air space compared to the case if the lens consisted of water with the same surface slope. Thus a function is required which translates lens surface slope – which is known from the lens' geometry – into the corresponding water surface slope. In the following chapters this function will be referred to as "water equivalent slope function" and its inverse as "inverse water equivalent slope function". It is nonlinear and can be described after Jähne [2004] as follows:

$$\vec{s} = \begin{pmatrix} s_x \\ s_y \end{pmatrix} \approx \frac{n_g - 1}{n_w - 1} \cdot \frac{\frac{\vec{x}}{R}}{\sqrt{1 - (\frac{x}{R})^2 - (\frac{y}{R})^2}} + \frac{[n_g \cdot (n_g - 1)^2 + n_w \cdot (n_w - 1)^2] \cdot (n_g - 1)}{2 \cdot n_g \cdot n_w \cdot (n_w - 1)^2} \cdot \left(\frac{\frac{\vec{x}}{R}}{\sqrt{1 - (\frac{x}{R})^2 - (\frac{y}{R})^2}} \right)^3 \tag{5.1}$$

Here $n_g \approx 1.515$ and $n_w \approx \frac{4}{3}$ denote the refractive indices of BK7 glass and water at the peak wavelength of the red LEDs at 625 nm, respectively. $\vec{r} = \begin{pmatrix} x \\ y \end{pmatrix}$ denotes the position on the lens relative to the centre of the lens surface.

Equation 5.1 is only an approximation of $\vec{s}(\vec{x})$ because it is calculated from a taylor expansion of the exact function up to third order. It shows that the x-component of water equivalent slope is not independent of the y-component of the position on the lens for higher slope values and vice versa. Therefore it has to be considered during the calibration process. Figure 5.11 visualizes the equivalent slope of the water surface

---

[4] BK7 glass has a refractive index of $n_g \approx 1.515$ at the peak wavelength of the red LEDs at 625 nm

(a) Lens float target with known slopes and sizes. Slopes are explained in Figure 5.10.

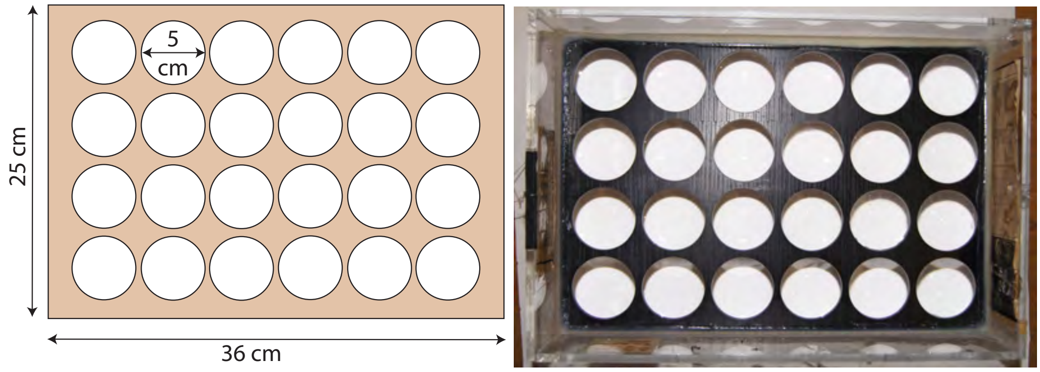

(b) Wavelet Target with known slopes. Schematic drawing modified after Rocholz [2008]. The numbers indicate the corresponding slope values.

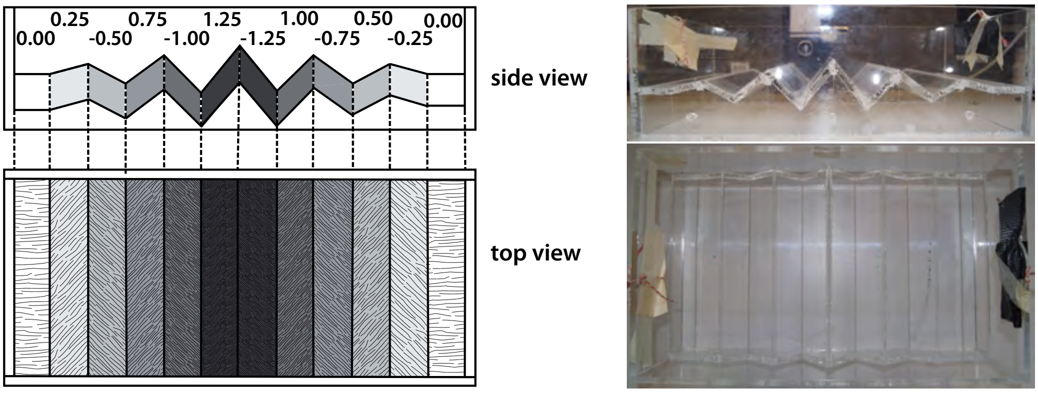

(c) Schematic drawing of a unit cell of the MTF target and photograph. Schematic drawing modified after Rocholz [2008]. The numbers indicate the hole diameter and the grid size and are given in mm.

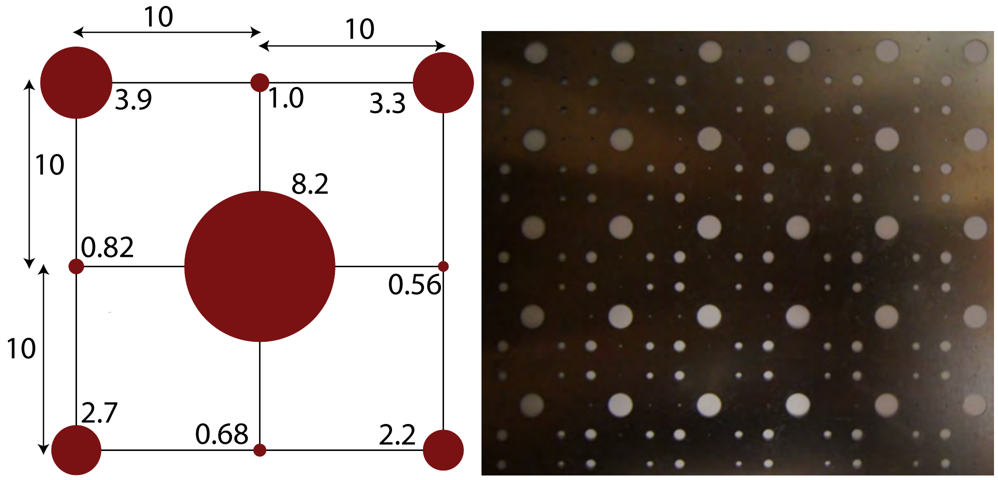

Figure 5.9.: Calibration Targets for accuracy testing. Left hand side: Schematic drawing. Right hand side: Photograph.

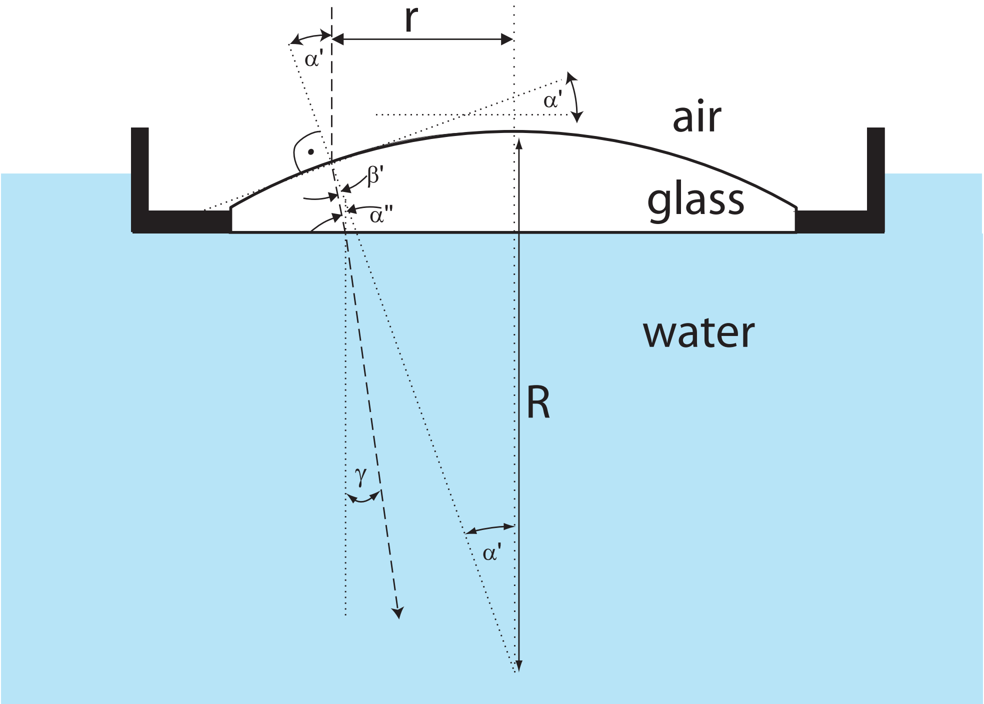

Figure 5.10.: Single lens of the lens float target with ray geometry. Image modified after Rocholz [2008].

as a function of the position on a lens float lens as calculated from Equation 5.1.

As the lenses can be considered spherical the relation between the slope at the surface of the lens $\vec{s}' = (s_x, s_y)^T$ and the position on the lens relative to the centre of the lens surface $\vec{r} = (x, y)^T$ is

$$\vec{s}' = \begin{pmatrix} \tan(\alpha'_x) \\ \tan(\alpha'_y) \end{pmatrix} = \frac{\vec{r}}{\sqrt{R^2 - |\vec{r}|^2}} \tag{5.2}$$

This can be plugged into Equation 5.1 to obtain the water equivalent slope function:

$$\vec{s} \approx \frac{n_g - 1}{n_w - 1} \cdot \vec{s}' + \frac{\left[n_g \cdot (n_g - 1)^2 + n_w \cdot (n_w - 1)^2\right] \cdot (n_g - 1)}{2 \cdot n_g \cdot n_w \cdot (n_w - 1)^2} \cdot \vec{s}'^3 \tag{5.3}$$

The lens float target is useful for calibration purposes because slope varies continuously in alongwind and crosswind direction. This way a single set of calibration images is sufficient to yield both components of the slope calibration function $f(x, y)$.

A fundamental assumption made during the calibration process with the lens float target is that the calibration function f is sufficiently homogeneous, i.e. within

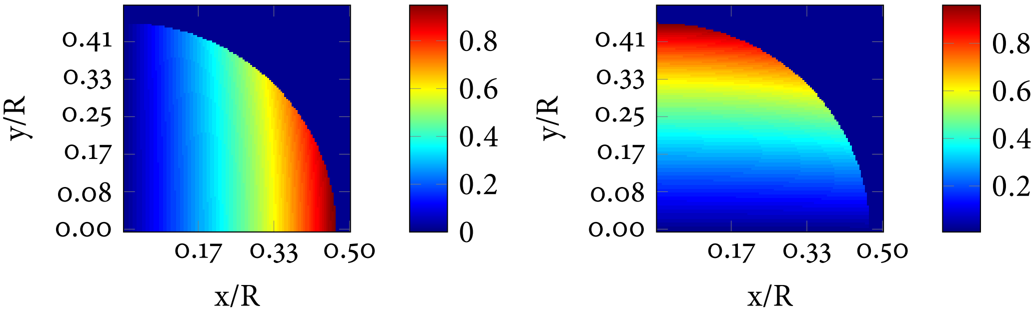

Figure 5.11.: Equivalent slope of the water surface in x direction (left) and in y direction (right) as a function of the position on a lens float lens (x,y) normalized with the radius of curvature R.

the spatial extent of a lens the position dependency of f is weak. This is true for a telecentric illumination which is set up correctly. A qualitative experimental analysis for the given setup is presented in section 8.5.

Experimental difficulties arise from the fact that the lens float target has to be perfectly balanced without any air bubbles trapped below. Secondly, the water body has to be completely at rest which requires some time of waiting. Furthermore, the centre of the lenses has to be determined precisely in order to ensure a correct calibration result from Equation 5.2. This is because the theoretical model for lens surface slope and an intensity ratio image of a lens are matched in order to obtain the calibration function (see section 7.1.2).

5.6.2 Wavelet target

The wavelet target is made from acrylic and consists of a total of 11 planes with different slope values in one horizontal direction. In the perpendicular horizontal direction its slope is constantly zero. The wavelet target is depicted in Figure 5.9b and a schematic drawing indicating the slope values of each plane is provided as well. The plexiglass planes have a finite thickness which causes a displacement of the light rays but no change of their inclination because the two bounding surfaces are parallel to each other. Because slope is changing in one direction only the wavelet target is harder to use for calibration purposes. For this work it is used for testing the calibration result only.

5.6.3 MTF target

The MTF target is a thin metal stencil containing a 10 mm ± 10 µm grid of holes with varying diameter. It was designed to measure the Modulation Transfer Function (MTF) of the camera system. For this thesis it is solely used for calculating the footprint of the camera on the water surface and for determining the scaling factor between image coordinates in pixels and real world coordinates in millimetres. An illustration of a unit cell of the MTF target with the individual hole diameters is given in figure 5.9c as well as a close-up photograph.

6

Measurement Campaigns in the Heidelberg Aeolotron

Two major measurement campaigns have been carried out at the Heidelberg Aeolotron for this thesis, one in 2013 with nature-like surface films and one in 2014 with clean water and Triton X-100. In addition, some separate small experiments have been conducted in order to characterize the ISG setup.

6.1 2013 Aeolotron Measurements

The experiments in spring 2013 have been conducted in cooperation with Klaus Schneider-Zapp, School of Marine Science and Technology, University of Newcastle, United Kingdom. This campaign was carried out in order to investigate the influence of naturally occurring surfactants on air-sea gas exchange.

The ISG was used to determine mean square slope values as well as to investigate wave number spectra.

Simultaneously, gas exchange measurements for N2O and C2HF5 were conducted similar to Krall [2013]. Using Fourier-Transformation-Infrared (FTIR) spectroscopy the gas concentration was measured in the air space and in the water space. Using a mass balance method, transfer velocities were determined in evasion measurements. Schmidt number exponents were determined from both gases. Active thermography measurements with scanned infrared laser lines were performed by Nagel [2014] is order to determine heat transfer. Friction velocities were measured similar to Bopp [2014].

The measurements have been conducted at seven different wind speeds. In table 6.1 the different conditions are summarized. Therein u_{ref} is the reference wind speed as it is measured in the Aeolotron (see section 6.3). The frequency f_{wind} describes the frequency which is set at the frequency converter which drives the wind generators.

The time of measurement varies between the conditions and ranges from about 30 minutes for the highest wind speed up to more than two hours for the lowest wind speed. On each day, measurements started with the lowest wind speed. After each condition, the wind was turned off for a short while for thermography measurements of the drift velocity of the water surface. This time is assumed to be short enough in order to keep the water velocity at an (almost) constant level. Then the next wind speed was set and after 15 minutes of waiting time for the water body to reach its new equilibrium velocity all data acquisition was started again. More information on the wind speed during the experiment is given in section A.1 in the appendix. The water surface was not skimmed before the experiment[1]. Further details of the experimental conditions are provided in Nagel [2014].

The first two sets of measurements were conducted with the soluble surfactant dextran (see section 2.6.3). The first set was conducted with a concentration of $1\,\mathrm{mg/l} \mathrel{\widehat{=}} 18\,\mathrm{g}$ total[2] and the second set with $2\,\mathrm{mg/l} \mathrel{\widehat{=}} 36\,\mathrm{g}$ total. For the third and fourth set of measurements, 7.2 mg of the soluble surfactant palmitic acid, 95 mg of the unsoluble glycolipid mono-galactosyl-acylglycerol (MGDG) and 36 mg of the insoluble phospholipid phosphatidylglycerol (PG) were added to the water with the higher dextran concentration of 2 mg/l. This mixture was chosen to mimic naturally occurring surfactants and is referred to as *full mix* hereafter. The individual constituents are described in section 2.6.3.

ISG settings: The camera lens which was used for the experiments is a Nikon Micro Nikkor 105 mm, f=1:2.8 lens. The f-stop was set to 5.6. For the first day and the first wind speed condition on the second day, ISG image sequences of 4 raw images each were taken at $f = 6030\,\mathrm{Hz}$ with a delay of 1.496 s between the first images of two consecutive sequences. For all other wind speed conditions, sequences of 20 raw images each were taken with the same settings. At the end of each condition except for the first condition of the first day[3], a long sequence of 20000 images was taken at $f = 6030\,\mathrm{Hz}$ (see section 7.2 for details).

---

[1] The term *skimming* describes the process of cleaning the water surface to remove surface films. For that, a small barrier is mounted in the flume perpendicular to the direction of the main current and the wind such that its lower part touches the water surface. Then the wind is turned on at very low wind speed which leads to the water surface including any remaining surfactants and particles being pushed into a channel inside the barrier; leaving a clean water surface. The channel is continuously emptied by a pump.

[2] per 18 000 l, which is one filling of the Aeolotron at the water height of 1 m as used for these experiments.

[3] The long sequence for the first day of measurements is missing due to PC memory issues

Table 6.1.: Wind speeds and conditions for the 2013 Aeolotron campaign. Conditions where complete ISG data is available are marked with an x. For the conditions marked by (x), the length of each image sequence was accidentally set to 4 raw images instead of the desired 20. For the conditions marked with a star *, the long sequence of 20000 raw images is missing.

	f_{wind} [Hz]		5	7	9	12	16	22	29
	u_{ref} $[\frac{\mathrm{m}}{\mathrm{s}}]$		1.48	2.20	2.89	3.88	5.11	6.77	8.42
Date	surfactant	water height							
30/04/2013	$1\,\frac{\mathrm{mg}}{\mathrm{l}}$ Dextran	100.4 cm	(x)*	(x)	(x)	(x)	(x)	(x)	(x)
03/05/2013	$2\,\frac{\mathrm{mg}}{\mathrm{l}}$ Dextran	100.7 cm	(x)	x	x	x	x	x	x
08/05/2013	Full mix	99.7 cm	x	x*	x	x	x	x	x
10/05/2013	Full mix	100.0 cm	x	x	x	x	x	x	x

6.2 2014 Aeolotron Measurements

The measurements in 2014 have not been evaluated during the scope of this thesis, but the experiments are described in detail for future reference.

6.2.1 Wave Field Equilibrium Measurements

The measurements in early 2014 have been conducted together with Bopp [2014] who determined friction velocities for a clean and for a film-covered water surface (Triton X-100). ISG data is available for a wide range of wind speeds and was recorded in order to calculate mean square slope values for several different wind speeds at the given surfactant conditions. In table 6.2, the conditions are summarized. Therein, the values for u_{ref} are given for clean water according to Bopp and Jähne [2014].

On 21/02/2014, the first set of measurements was conducted with clean water without surfactants. The remaining six sets of measurements were conducted with the soluble surfactant Triton X-100 (see section 2.6.3) in two different concentrations. For the first three days of measurements with surfactant (25/02/2014,26/02/2014 and 27/02/2014), a concentration of $\frac{0.6\,\mathrm{g}}{18\,\mathrm{m}^3} \mathrel{\widehat{=}} 0.033\,\mathrm{g/m}^3$ was used. The last three sets (28/02/2014, 02/03/2014 and 03/03/2014) were conducted with a concentration of $\frac{3.0\,\mathrm{g}}{18\,\mathrm{m}^3} \mathrel{\widehat{=}} 0.167\,\mathrm{g/m}^3$. In order to conduct water height measurements, 5 g of the hydrophilic, pH-sensitive fluorescent dye pyranine have been added to the water before starting the measurements on 25/02/2014 and 26/02/2014 each.

The time of measurement varies between the conditions and ranges from about

10 minutes for the conditions measured on 26/02/2014 and 02/03/2014 up to more than two and a half hours for the lowest wind speeds on the other days[4]. On the two days just mentioned, a dense range of wind speeds was covered in order to obtain a coarse understanding of mean square slope values for many different wind speeds. As a result, the waiting time between two ISG measurements had to be drastically reduced, thus sacrificing the fulfilment of wave equilibrium conditions. For the other days, the waiting time between two measurements have been sufficient to guarantee equilibrium conditions concerning the wave field, even for low wind speeds. In between the individual conditions on 26/02/2014 and 02/03/2014, the wind was shut down for at least 15 min in order to allow for a decline of the wave field[5]. On these days, the ISG measurement was started approximately 5 min to 10 min after the wind was started for each condition. On the other days, the wind was not shut down between the individual conditions and ISG measurements were started at about 30 min to 150 min[6] after the new wind speed was set.

The water surface was skimmed before the first day of measurement with clean water in order to avoid surface contaminations.

ISG Settings: For the experiments a Zeiss 100 mm,f=1:2 lens was used at an f-stop of 8. Sequences of 20000 raw images were taken at $f = 6000$ Hz for each condition (see section 7.2 for details).

6.2.2 Continuous Wind Speed Measurements

In between 26/02/2014 and 28/02/2014 additional ISG measurements have been performed where the frequency f_{wind} at the frequency converter which drives the wind generation was changed continuously from 6 Hz to 22 Hz and back. This corresponds to wind speeds between $u_{ref}^{clean} = 1.86$ m/s to 6.72 m/s. The frequency was changed with a rate of $\Delta f_{wind} = 0.005$ Hz/s. An overview is given in table 6.3. One such measurement took approximately one hour. Sequences of 4 raw images were taken at $f = 6000$ Hz with a spacing of 500 ms between two sequences (see section 5.4 and section 7.2 for details).

These measurements were conducted with the same water, surfactant concentrations and camera lens as the equilibrium measurements described in section 6.2.1.

---

[4] Note, that only one ISG measurement is conducted for each sequence due to the rather long time needed for data transfer and storage (approximately 30 min for a sequence of 20000 raw images).

[5] Note that the mean water velocity will not reach zero during that time.

[6] The exact time depends on the wind speed with more time to wait for an equilibrium state at low wind speeds.

Table 6.2.: Wind speeds and conditions for the 2014 Aeolotron campaign I. Conditions which were measured on the respective day are marked with an x.

		f_{wind} [Hz]	5	6	7	8	9	10	11	12
		u_{ref} $\left[\frac{m}{s}\right]$	1.52	1.86	2.16	2.51	2.79	3.29	-	3.88
Date	surfactant	water height								
21/02/2014	clean water	99.5 cm			x		x			
25/02/2014	$\frac{0.6}{18}\frac{g}{m^3}$ Triton X-100	99.8 cm		x	x					x
26/02/2014	$\frac{0.6}{18}\frac{g}{m^3}$ Triton X-100	100.0 cm				x	x	x	x	x
27/02/2014	$\frac{0.6}{18}\frac{g}{m^3}$ Triton X-100	99.8 cm	x				x			
28/02/2014	$\frac{3.0}{18}\frac{g}{m^3}$ Triton X-100	100.0 cm			x					x
02/03/2014	$\frac{3.0}{18}\frac{g}{m^3}$ Triton X-100	100.0 cm				x	x	x	x	x
03/03/2014	$\frac{3.0}{18}\frac{g}{m^3}$ Triton X-100	100.0 cm	x				x			

f_{wind} [Hz]	13	14	15	16	17	18	19	20	21	22	29	36
u_{ref} $\left[\frac{m}{s}\right]$	-	4.58	-	5.08	-	5.69	-	6.29	-	6.72	8.47	9.74
Date												
21/02/2014				x							x	x
25/02/2014										x		
26/02/2014	x	x	x	x	x	x	x	x	x	x		
27/02/2014				x							x	
28/02/2014										x		
02/03/2014	x	x	x	x	x	x	x	x	x	x		
03/03/2014				x							x	

Table 6.3.: Wind speeds and conditions for the 2014 Aeolotron campaign II

Date	**Condition**	**Wind Speeds**	**Wind Speed Change**
26/02/2014	$\frac{0.6}{18}$ g/m^3 Triton X-100	6 Hz → 22 Hz 1.86 m/s → 6.72 m/s	0.005 Hz/s
27/02/2014	$\frac{0.6}{18}$ g/m^3 Triton X-100	22 Hz → 6 Hz 6.72 m/s → 1.86 m/s	0.005 Hz/s
28/02/2014	$\frac{3.0}{18}$ g/m^3 Triton X-100	22 Hz → 6 Hz 6.72 m/s → 1.86 m/s	0.005 Hz/s
28/02/2014	$\frac{3.0}{18}$ g/m^3 Triton X-100	6 Hz → 22 Hz 1.86 m/s → 6.72 m/s	0.005 Hz/s

6.3 Wind Speed in the Aeolotron

Due to the annular shape of the Aeolotron the wind profile does not exhibit the typical logarithmic shape. As shown in Jähne [1980] this has almost no influence on transfer processes but it makes the comparison with field data more complicated.

In the Aeolotron, the wind is varied by setting the frequency f_{wind} at the frequency converter which drives the wind generators. Wind speed u_{ref} is measured in the centre of the air side of the flume right below the ceiling using a hydrometric vane and a pitot tube as described in Bopp [2014]. The wind speed u_{ref} at a given frequency f_{wind} at the frequency converter varies depending on the amount of water, of surfactants, and on the amount and position of measurement devices in the flume. In order to compare the wind speed with measurements in the field and in other facilities, the facility-specific reference wind speed u_{ref} is of little use. Instead, the friction velocity $u^\star$ which is separately determined and converted into the value u_{10} as described in Bopp and Jähne [2014]. u_{10} is the wind speed which were measured in ten meters height on the open ocean if the same friction velocity $u^\star$ as in the Aeolotron is assumed.

6.3.1 Other measurements

In addition to the large measurement campaigns mentioned before, several test measurements with different targets have been performed with the ISG. The images of the wavelet target evaluated in section 8.3 were recorded on 12/06/2014 with a Zeiss 100 mm,f=1:2 lens at an f-stop of 8.

Part III.

Data Analysis & Discussion

7

Processing Routine

The raw images acquired with the ISG setup do not directly express any useful physical information. Several processing steps are necessary to extract this information from the raw images (see Figure 7.1).

During the first step the images of the lens float calibration target are used to obtain a lookup table (LUT) which allows for the conversion of measured intensity ratios in alongwind and crosswind directions into the corresponding surface slope values. This step will be called the *calibration step*.

In a second step, the *slope calculation step*, the raw images of the water surface are preprocessed. After that the LUT from the previous step is applied to the preprocessed data. This way images containing slope information for both directions are obtained.

In the third and last step, the *analysis step*, mean square slope, wave number energy spectra and other statistical information is extracted from the slope images of the previous step.

In the following chapter, the three steps are explained in detail. All calculations were done in MATLAB® R 2013b. The raw data is stored in raw format and the results of intermediate steps are stored in raw format or in HDF5 format.

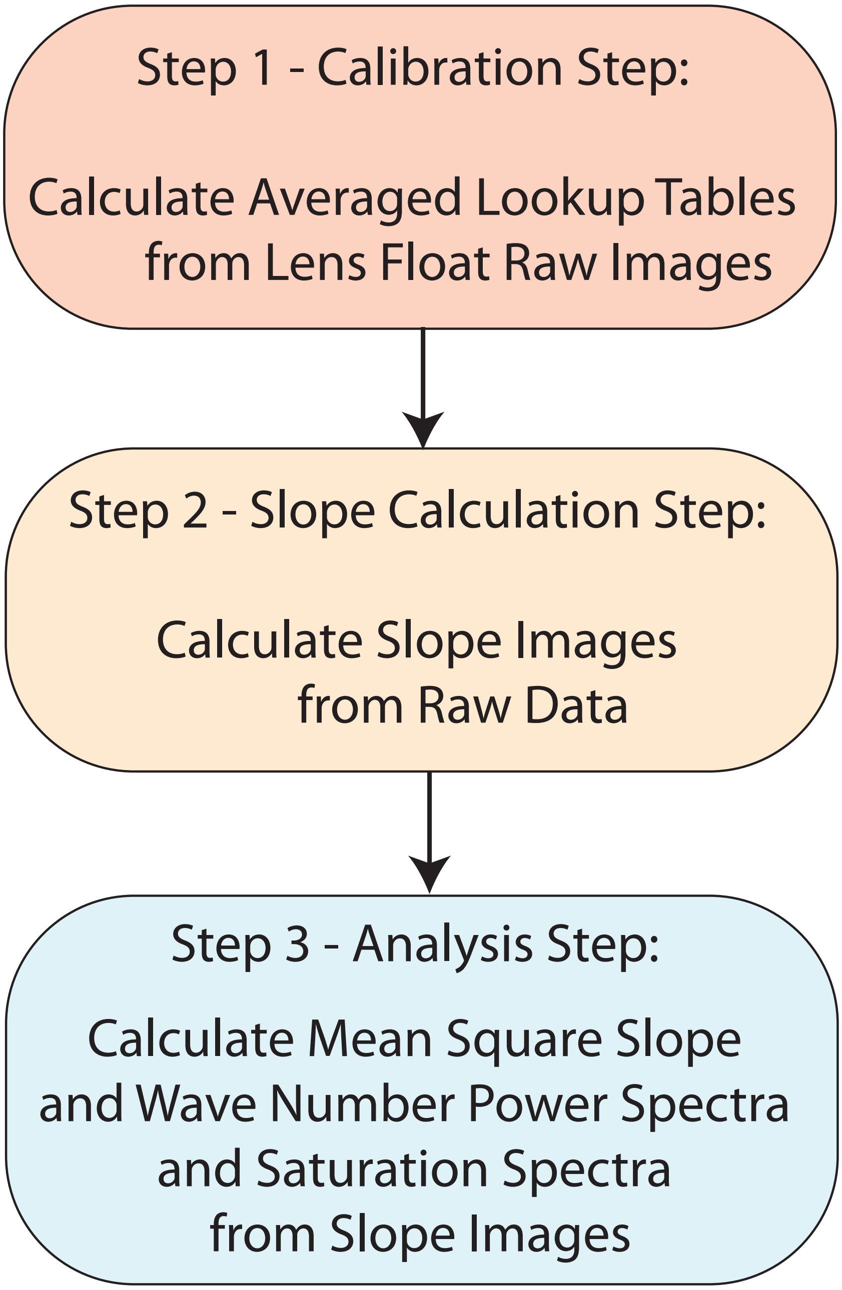

Figure 7.1.: Overview of the ISG data processing routine.

7.1 First Step: Calibration

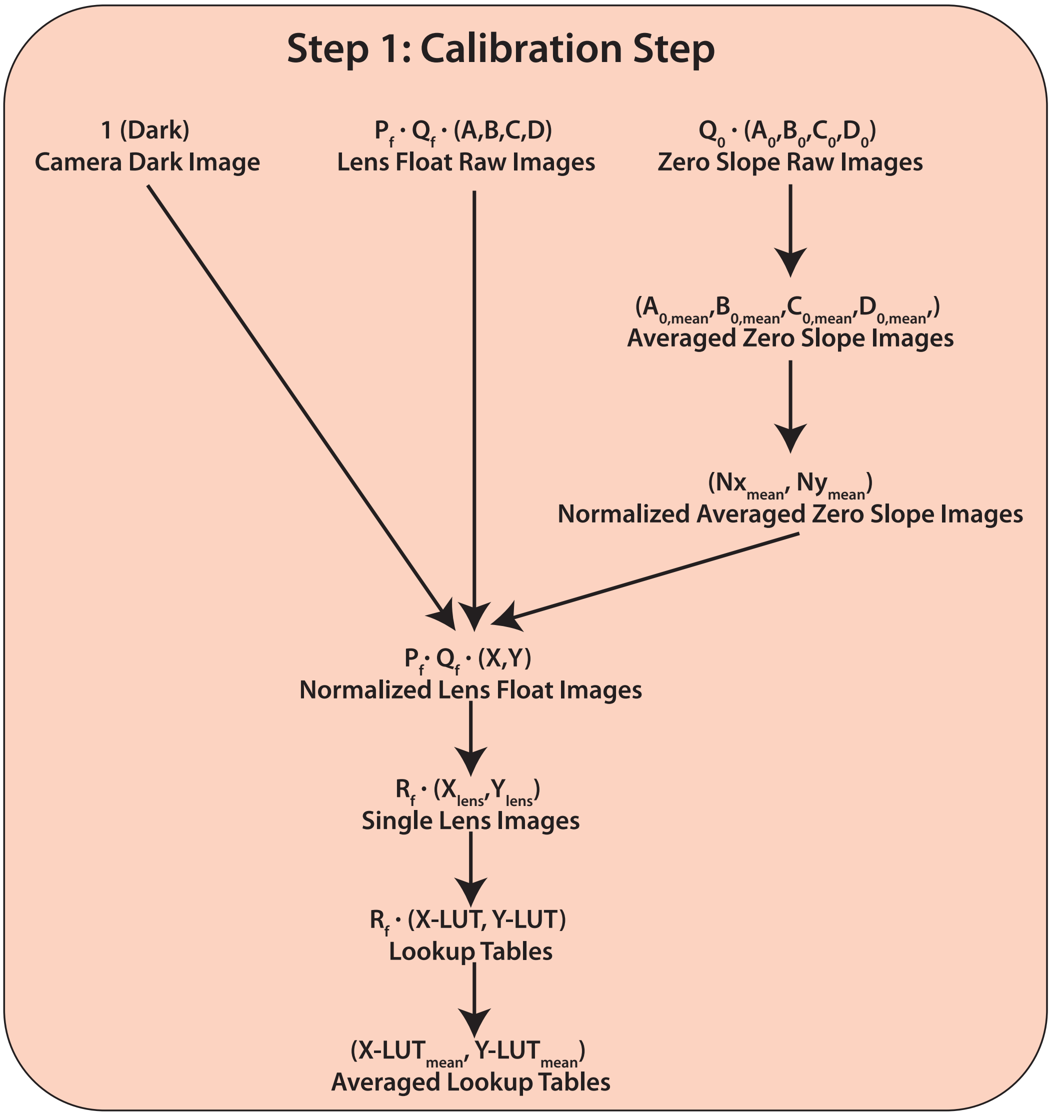

Figure 7.2.: Processing routine step 1: Calibration step. (A,B,C,D) refers to the illumination wedges as described in section 5.4. The indices 0 and f indicate *zero slope* and *lens float*, respectively. Q indicates the number of subsequences (A,B,C,D) per image sequence and P indicates the number of image sequences.

The calibration data consists of one dark image of the camera taken on 30/04/2014 as depicted in Figure 7.3, one sequence of zero slope images (A_0, B_0, C_0, D_0) of length Q_0 for each day of measurement as shown in Figure 7.4a and P_f sequences of lens float images (A, B, C, D) of length Q_f each as given in Figure 7.5. Here the letters (A,B,C,D) refer to the respective illumination wedges as described in section 5.4 and the indices 0 and f indicate *zero slope* and *lens float*, respectively.

Figure 7.2 depicts all steps which are necessary in order to prepare the calibration data in a preprocessing step and to produce an empirical calibration "function" in the form of averaged lookup tables from the calibration data. The lookup tables are explained in section 7.1.2.

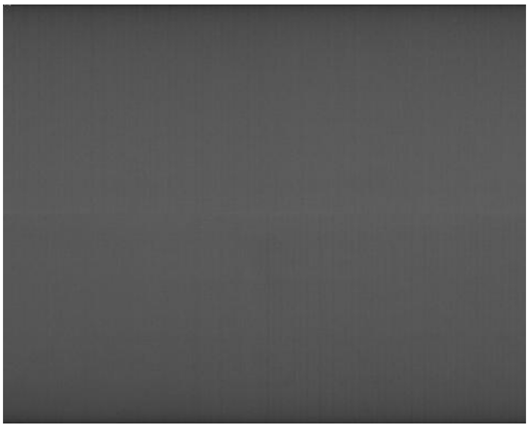

Figure 7.3.: Camera Dark Image $Dark$.

7.1.1 Preprocessing

The camera installed at the ISG setup provides intensity images. In order to calculate slope images from which spectra can be deduced the raw data of the experiment as well as the calibration data has to undergo some preprocessing steps first.

Dark Image and Zero Images

The zero slope images (A_0, B_0, C_0, D_0) are averaged over sequences of length Q_0 right after acquisition. The raw data is not saved, but the averaged zero slope images $(A_{0,\text{mean}}, B_{0,\text{mean}}, C_{0,\text{mean}}, D_{0,\text{mean}})$ are saved in tif format. One averaged image is saved for each illumination wedge. The lengths Q_0 are given in Table 7.1 for each day of measurement. Figure 7.4a shows the averaged zero slope images. Next, these are normalized as follows:

$$Nx_{\text{mean}} = \frac{A_{0,\text{mean}} - B_{0,\text{mean}}}{A_{0,\text{mean}} + B_{0,\text{mean}} - 2 \cdot Dark} \tag{7.1}$$

$$Ny_{\text{mean}} = \frac{C_{0,\text{mean}} - D_{0,\text{mean}}}{C_{0,\text{mean}} + D_{0,\text{mean}} - 2 \cdot Dark} \tag{7.2}$$

The resulting images Nx_{mean} and Ny_{mean} represent the intensity ratio for zero slope in alongwind and crosswind direction, respectively. As can be seen in Figure 7.4b the normalization process suppresses disturbing features in the raw images such as defects in the window or dirt on the water surface, the light source or the optical components which are visible as darker areas in the raw images.

Table 7.1.: Number of images used to average the zero slope images for each day of measurement. When two values are given, data with both lengths exists for that day.

Date	# of images $Q_0 \cdot 4$
30/04/2013	$5 \cdot 4 = 20$
03/05/2013	$250 \cdot 4 = 1000$
08/05/2013	$1508 \cdot 4 = 6032$
10/05/2013	$5 \cdot 4 = 20$
21/02/2014	$5 \cdot 4 = 20$
25/02/2014	$5 \cdot 4 = 20$ or $50 \cdot 4 = 200$
26/02/2014	$5 \cdot 4 = 20$
27/02/2014	$5 \cdot 4 = 20$ or $50 \cdot 4 = 200$
28/02/2014	$5 \cdot 4 = 20$
02/03/2014	$50 \cdot 4 = 200$
03/03/2014	$5 \cdot 4 = 20$
12/06/2014	$50 \cdot 4 = 200$

Lens Float Target Images

Each day a total of P_f[1] image sequences of the lens float target are recorded. Each image sequence consists of a multiple of subsequences of 4 images with different illumination wedges (A,B,C,D) each. Example images are depicted in Figure 7.5a. For each of these Q_f subsequences one intensity ratio image X of the component in alongwind direction x is calculated from A and B and one intensity ratio image Y of the component in crosswind direction y is calculated from C and D. This is done similarly as for the zero slope images according to the following equations:

$$X = \frac{A - B}{A + B - 2 \cdot Dark} - Nx_{\text{mean}} \tag{7.3}$$

$$Y = \frac{C - D}{C + D - 2 \cdot Dark} - Ny_{\text{mean}} \tag{7.4}$$

The result after normalization is shown in Figure 7.5b and will be referred to as normalized lens float (intensity) images (X,Y). The main advantages of this so called *ratio imaging* are that it corrects for lens effects at the water surface as well as that it reduces the demands to the homogeneity of the light source. This is demonstrated

---

[1] Remember that the index f labels the image sequence as *lens float target* data.

when comparing Figure 7.5a and Figure 7.5b. The individual LEDs of the light source are visible in the raw images although a diffusion screen is used to homogenize the light source. In the normalized images, they are not visible any more.

(a) Averaged Zero Slope Data. Left hand side: illumination wedges $A_{0,\mathrm{mean}}$, $B_{0,\mathrm{mean}}$ in upwind direction x. Right hand side: illumination wedges $C_{0,\mathrm{mean}}$, $D_{0,\mathrm{mean}}$ in crosswind direction y.

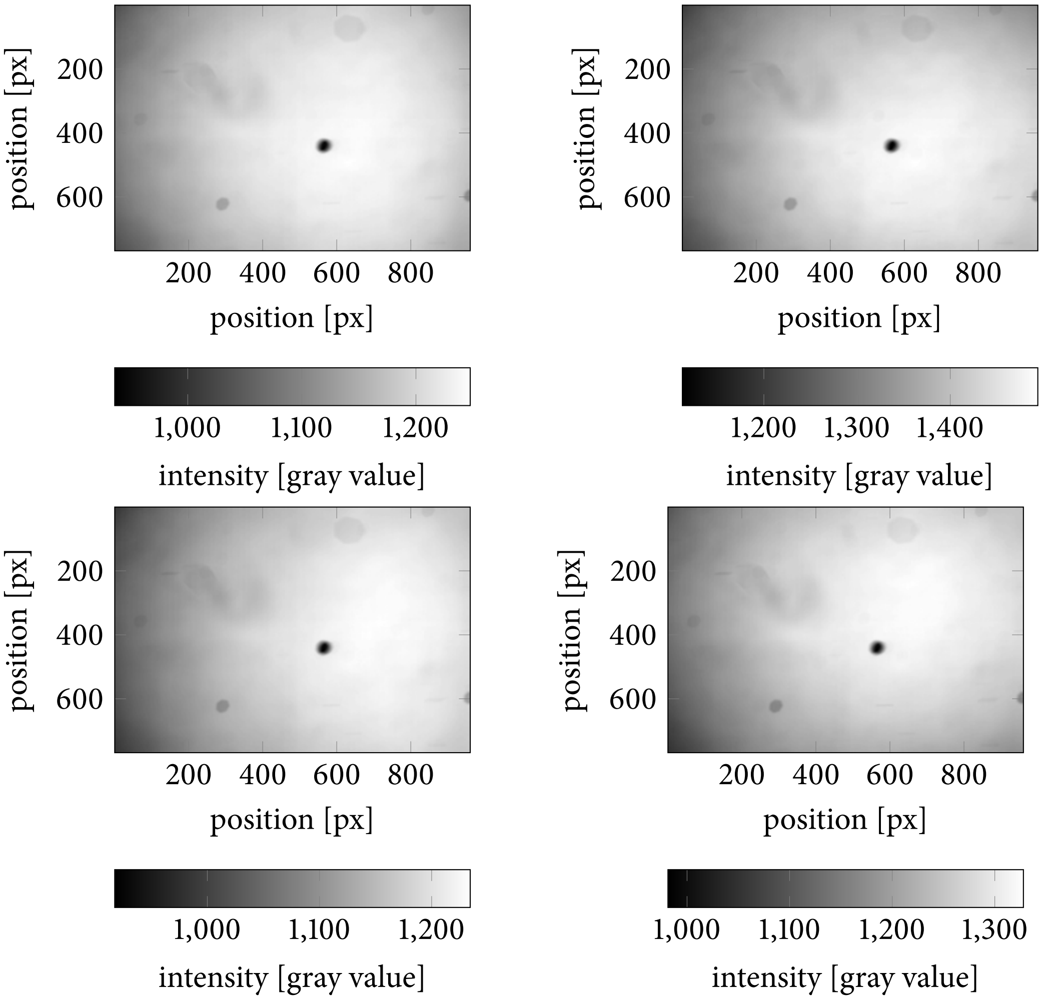

(b) Normalized Averaged Zero Slope Data. Left hand side: alongwind component Nx_{mean}. Right hand side: crosswind component Ny_{mean}.

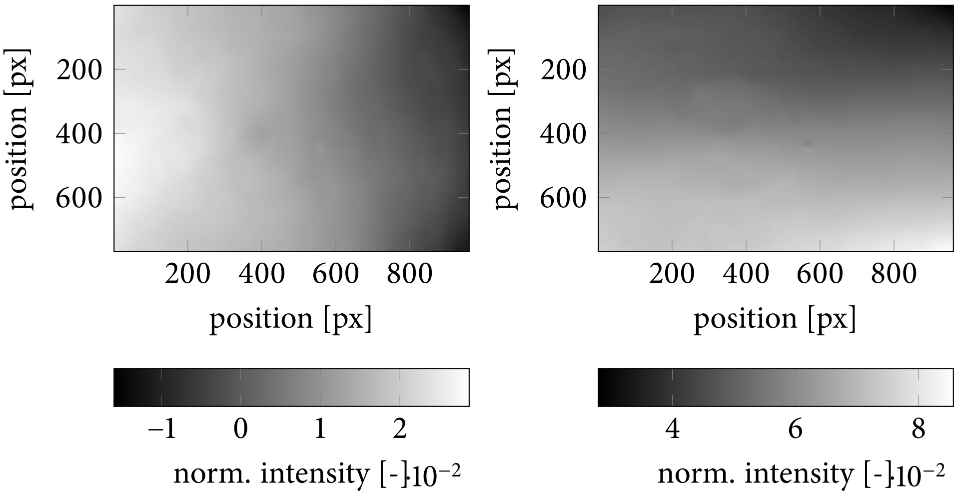

Figure 7.4.: Zero slope images. Averaged raw data and normalized images. (data of 30/04/2013)

(a) Raw data. Left hand side: illumination wedges in upwind direction x. Right hand side: illumination wedges in crosswind direction y.

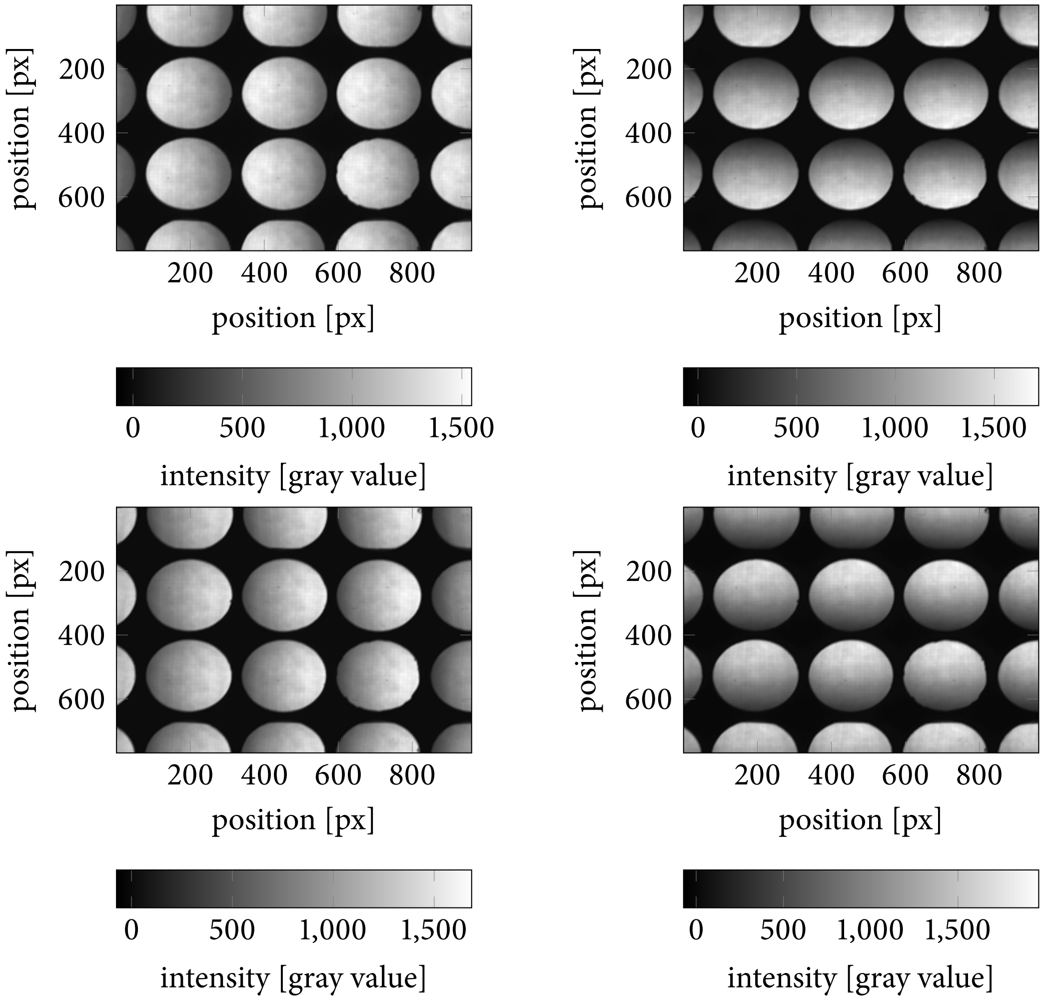

(b) Normalized Images. Left hand side: upwind direction x. Right hand side: crosswind direction y.

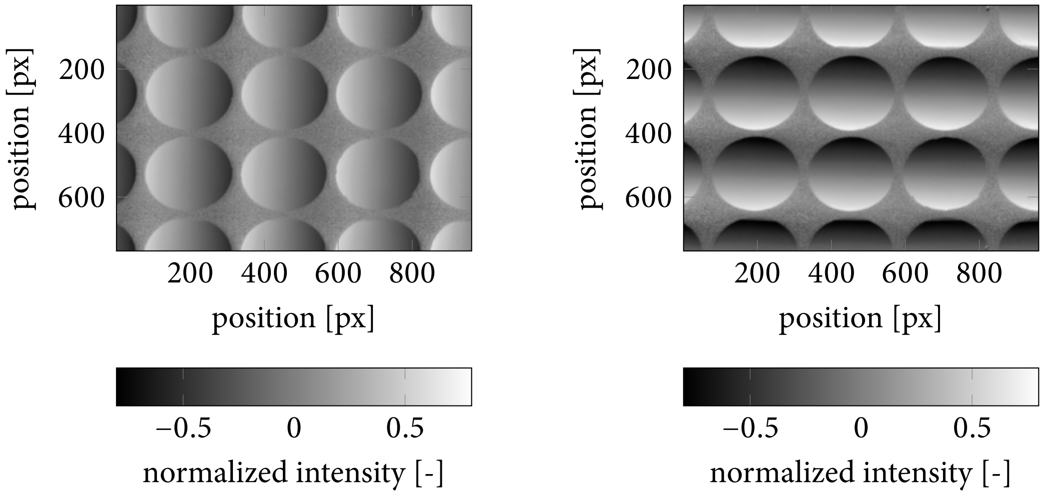

Figure 7.5.: Lens detection process: Raw data and normalized images (data of 30/04/2013).

7.1.2 Lookup Tables

After data preprocessing, a lookup table is created from the normalized lens float target calibration images which links calculated slope data $\vec{s} = [s_x, s_y]^T$ with measured intensity ratios $\vec{I} = [I_x, I_y]^T$.

Lens Detection

As a first step, the separate lenses have to be detected in the lens float calibration images. This is implemented with the MATLAB® function *imfindcircles* using a two-stage circular Hough transform with a sensitivity factor of 0.97 and a fixed edge gradient threshold of 0.01.

Exemplary images of several stages of this process are shown in Figure 7.6.

The circle detection is performed on a binary representation of a gradient image of the first illumination wedge A of a 4-image sequence[2] (Figure 7.6a). Therefore the intensity threshold to obtain the binary representation is set to 200. The result after circle detection is shown in Figure 7.6b.

An additional step is the automatic validation of the detected lenses where only those lenses are kept which lie entirely inside the image domain. The result of this step is depicted in Figure 7.6c.

The circle detection is rather error-prone which is why a manual selection of correctly detected lenses is performed afterwards. Examples of misdetected lenses are given in Figure 7.7. Most frequently, extracted lens images are discarded because they depict a lens of the lens float target which is glued such that it exhibits an irregular shape at the outside (see Figure 7.7c and Figure 8.4). Technically, these images do not have to be discarded because the center of the lens is determined correctly but it is done here for additional accuracy at the outside of the lenses. Secondly, water droplets on top of the lenses or air bubbles below the lenses due to experimental inaccuracy occur (Figure 7.7b). Thirdly, circle detection fails for some images (c.p. Figure 7.7a). This case

(a) Gradient Image

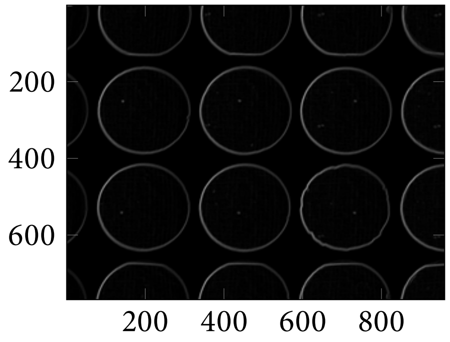

(b) Detected Lenses

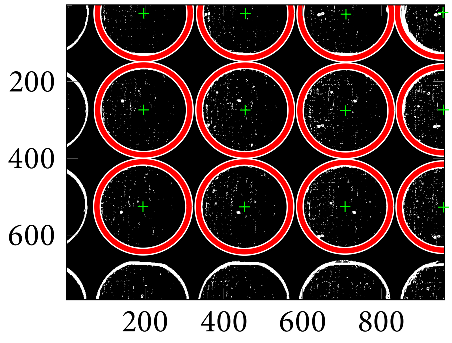

(c) Validated Lenses

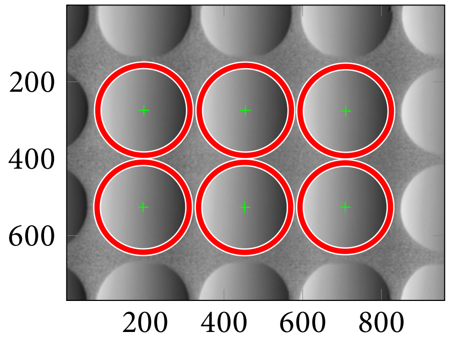

Figure 7.6.: Lens Detection Process (data of 30/04/2013)

---

[2] after correction for the camera dark image

occurs very rarely; for the data of 30/04/2013 only
two such cases were detected out of a total of 400
individual lens images as the output of the automatic validation step.

After correction for zero slope images the detected lenses are stored in HDF5 format together with a flag indicating the result of the manual selection process. The position of the lens in the calibration image is stored as well.

For the 2013 Aeolotron campaign data and 12/06/2014, Table 7.2 gives the number of lenses which were detected and validated by the algorithm and the number of lenses which were selected by hand for LUT computation.

Table 7.2.: Number R_f of lens float target lens image pairs (X_{lens}, Y_{lens}) used to create a mean lookup table pair $(X - LUT_{\text{mean}}, Y - LUT_{\text{mean}})$ for each day of the 2013 Aeolotron campaign

Date	# of lenses detected	# of valid lenses
30/04/2013	400	271
03/05/2013	2916	2013
08/05/2013	638	256
10/05/2013	606	255
12/06/2014	1659	802

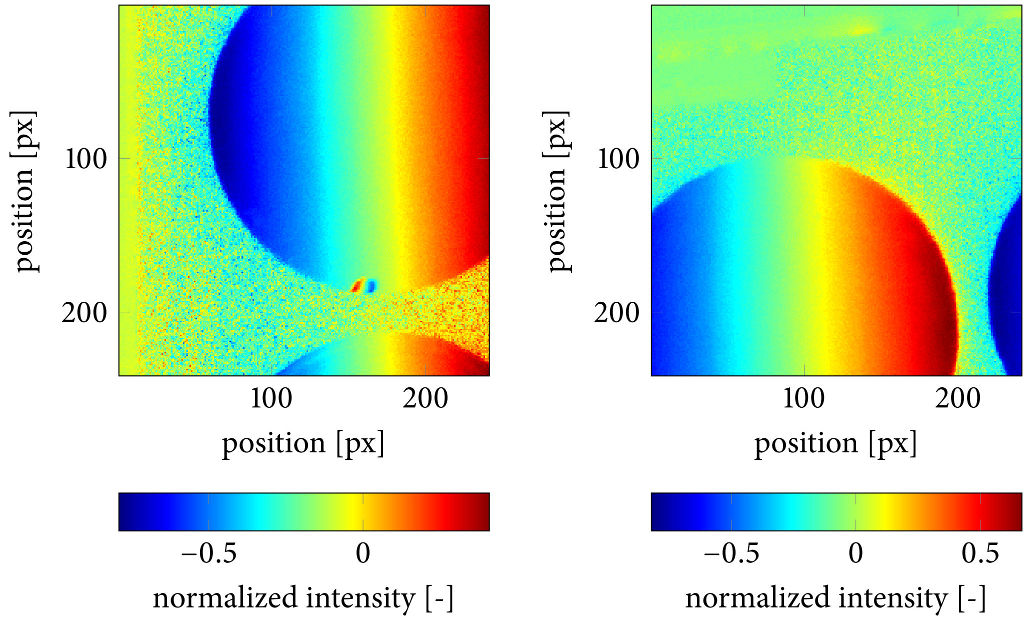

(a) Wrong position

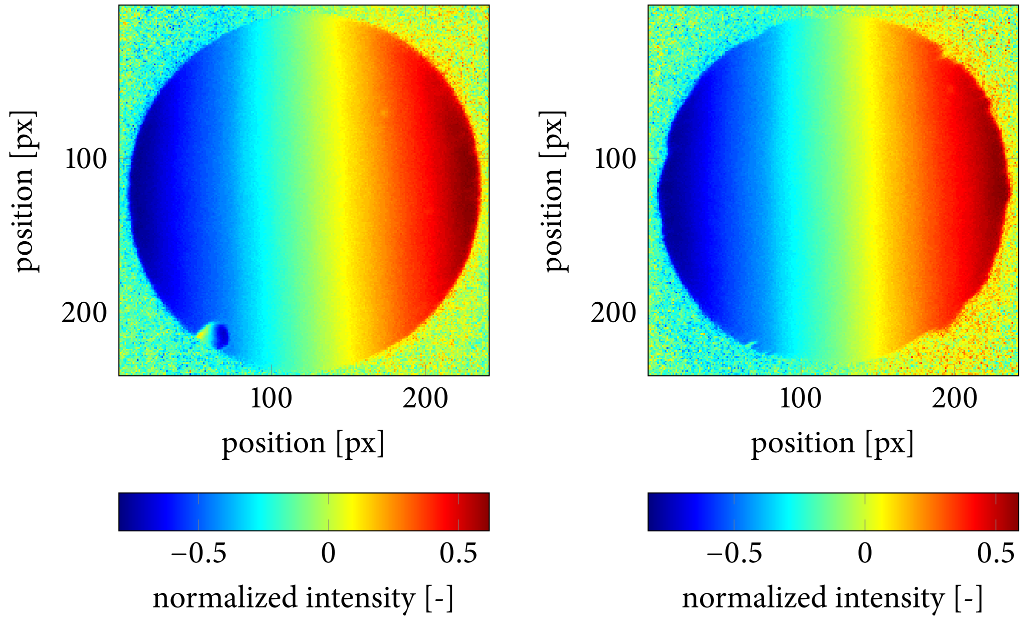

(b) Air bubble or water droplets

(c) Badly shaped lens

Figure 7.7.: Examples of misdetected lenses (data of 30/04/2013).

LUT calculation

In a first step, a lookup table pair $(X\text{-}LUT, Y\text{-}LUT)$ is calculated for each of the R_f valid lens image pairs $(X_{\text{lens}}, Y_{\text{lens}})$ from the previous step separately. In a second step, these are averaged in order to obtain a single mean lookup table pair $(X\text{-}LUT_{\text{mean}}, Y\text{-}LUT_{\text{mean}})$ for each day of measurement.

For the first step, all pixels outside the lens are set to NaN in the lens image pairs (X_{lens}, Y_{lens}). Also, the theoretical slope value expected at each pixel according to Equation 5.2 is calculated and translated into water equivalent slope via Equation 5.3. Then an integer-valued LUT index pair $(LUTindex_{\text{x}}, LUTindex_{\text{y}})$ in the interval (0,2000) is calculated for each pixel of the lens image pairs according to

$$(LUTindex_{\text{x}}, LUTindex_{\text{y}}) = (floor((X_{\text{lens}}+1)\cdot 1000), floor((Y_{\text{lens}}+1)\cdot 1000)) . \tag{7.5}$$

Now each pixel (m,n) is associated with a slope value pair $(sx_{\text{theor}}, sy_{\text{theor}})$, a normalized intensity value pair (I_x, I_y) as well as a LUT index pair $(LUTindex_{\text{x}}, LUTindex_{\text{y}})$. Next, a LUT pair $(X\text{-}LUT, Y\text{-}LUT)$ is calculated by looping through all pixels (m,n) of a LUT index image $LUTindex_{x/y}$ and assigning the corresponding slope component $sx_{\text{theor}}(m,n)$ to the respective LUT image pixel (i,j) which is determined by the LUT indices at position (m,n):

$$\begin{aligned} X\text{-}LUT(i,j) =& X\text{-}LUT\left(LUTindex_{\text{x}}(m,n), LUTindex_{\text{y}}(m,n)\right) = sx_{\text{theor}}(m,n) \\ Y\text{-}LUT(i,j) =& Y\text{-}LUT\left(LUTindex_{\text{x}}(m,n), LUTindex_{\text{y}}(m,n)\right) = sy_{\text{theor}}(m,n) \end{aligned} \tag{7.6}$$

When a value $\left(LUTindex_{\text{x}}(m,n), LUTindex_{\text{y}}(m,n)\right)$ occurs more than once the respective values are averaged.

As mentioned before, the second step comprises of averaging the LUT pairs to obtain one mean LUT pair $(\overline{X\text{-}LUT_{\text{mean}}}, \overline{Y\text{-}LUT_{\text{mean}}})$. After that missing values are interpolated[3]. Next, runaway values are eliminated with a 2D median filter[4] and the LUT is smoothed using a gaussian filter[5]. This yields the final LUT pair $(X\text{-}LUT_{\text{mean}}, Y\text{-}LUT_{\text{mean}})$. Figure 7.8a shows the LUT pair right after averaging and Figure 7.8b gives the final LUT pair after interpolation and averaging.

---

[3] using the Matlab® function *scatteredInterpolant*

[4] Matlab® function *medfilt2*

[5] Matlab® function *imfilter*

(a) Averaged LUT pair $\overline{X\text{-}LUT_{\text{mean}}}$ (left) and $\overline{Y\text{-}LUT_{\text{mean}}}$ (right)

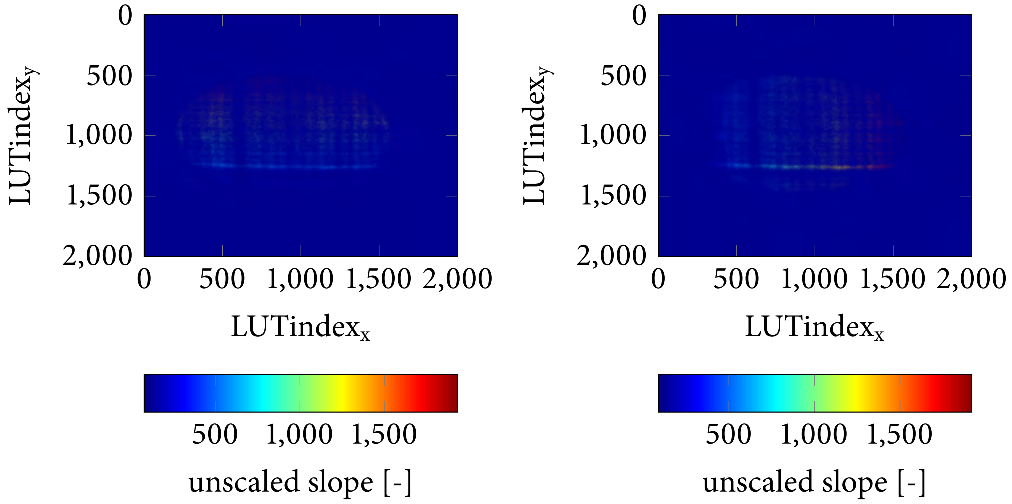

(b) Smoothed and interpolated LUT pair $X\text{-}LUT_{\text{mean}}$ (left) and $Y\text{-}LUT_{\text{mean}}$ (right).

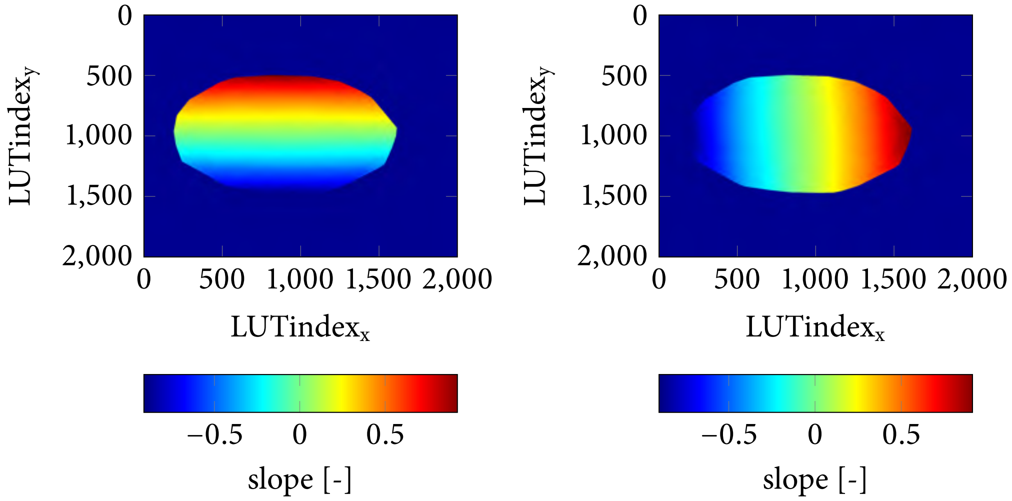

Figure 7.8.: LUT of 30/04/2013.

7.2 Second Step: Slope Calculation

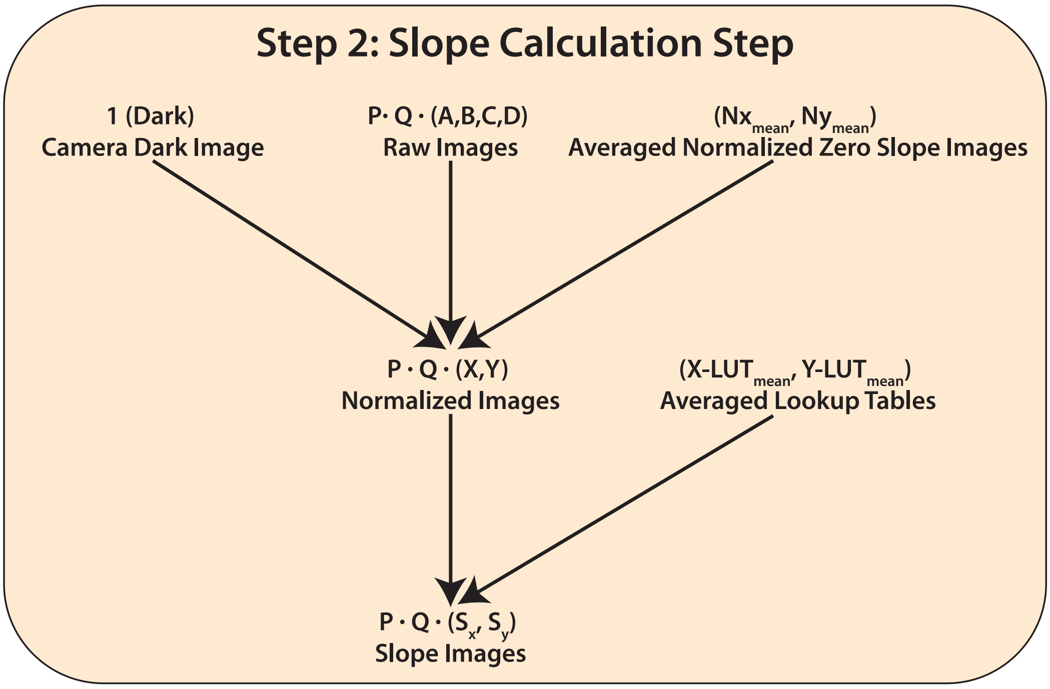

Figure 7.9.: Processing routine step 2: calculating slope images from raw data.

In order to calculate slope images from raw data (A, B, C, D) the LUT pair $(X\text{-}LUT_{\mathrm{mean}}, Y\text{-}LUT_{\mathrm{mean}})$ created in the previous step is applied to the normalized image pairs (X, Y). The normalization process is described in section 7.1. The normalized images are scaled onto the interval (0,2000) similar to Equation 7.5 to obtain two LUT indices. Next, a linear LUT index image is calculated according to

$$index = round(Y) \cdot 2000 + round(X). \tag{7.7}$$

Then the two slope images are calculated from

$$\begin{aligned} S_x &= X\text{-}LUT_{\mathrm{mean}}(index) \\ S_y &= Y\text{-}LUT_{\mathrm{mean}}(index). \end{aligned} \tag{7.8}$$

Finally, these images are saved in raw format with single precision.

7.3 Third Step: Analysis

In Figure 7.10 the steps necessary to calculate the desired mean square slope values and the saturation spectra from the slope images are visualized.

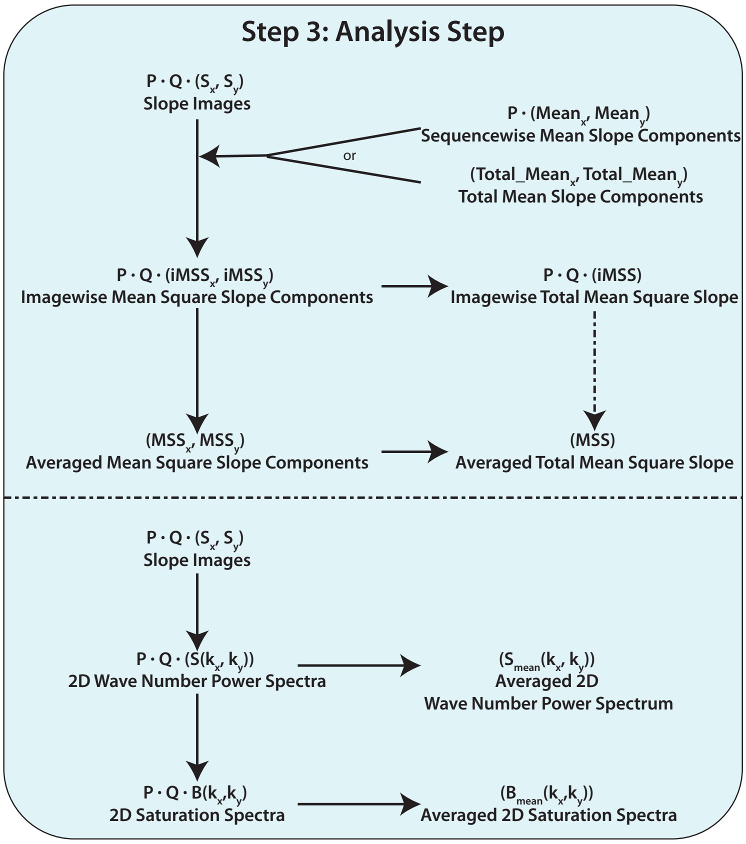

Figure 7.10.: Processing routine step 3: calculating mean square slope and spectra from slope images.

Mean Square Slope Calculation

In order to calculate mean square slope (mss) from the P sequences of slope image pairs $(S_x, S_y)_{p,q}$ of length Q each the following procedure is followed:

- A mean slope pair $(\text{mean}_x, \text{mean}_y)_p$ is calculated from each sequence by averaging $(S_x, S_y)_{p,q}$ along the temporal and spatial dimensions:

$$(\text{mean}_x, \text{mean}_y)_p = \frac{1}{m \cdot n \cdot q} \sum_{m,n,q} (S_x, S_y)_{m,n,p,q}. \tag{7.9}$$

  Recall that $m \in [1, M]$ and $n \in [1, N]$ are indices which indicate the pixel position (rows and columns).

- Next, from each image pair $(S_x, S_y)_{p,q}$ an imagewise mean square slope pair $(\mathrm{iMSS}_x, \mathrm{iMSS}_y)_{p,q}$ is calculated according to the following equation:

$$\mathrm{iMSS}_{x/y,p,q} = \frac{1}{M \cdot N} \sum_{m=1}^{M} \sum_{n=1}^{N} (S^{m,n}_{x/y,p,q} - \mathrm{mean}_{x/y,p} \cdot \mathbf{1})^2. \tag{7.10}$$

  Here, the square is to be understood as a pixelwise matrix multiplication in the sense of the Hadamard product[6] and **1** represents a matrix of ones the same size as S_x and S_y.

- Next, one way of continuing the calculations is to average the mean square slope components over all images of all sequences:

$$MSS_{x/y} = \sum_{q=1}^{\frac{Q}{2}} \sum_{p=1}^{P} \left(\frac{2}{Q} \cdot \frac{1}{P} \cdot \mathrm{iMSS}_{x/y,p,q} \right). \tag{7.11}$$

- Finally, the total mean square slope value is calculated as the sum of both components:

$$\mathrm{MSS} = \mathrm{MSS}_x + \mathrm{MSS}_y. \tag{7.12}$$

- Alternatively, the last two steps can be calculated in reverse order. Then a total mean square slope value

$$iMSS_{p,q} = \mathrm{iMSS}_{x,p,q} + \mathrm{iMSS}_{y,p,q} \tag{7.13}$$

  is calculated from each mean square slope pair $(\mathrm{iMSS}_x, \mathrm{iMSS}_y)_{p,q}$ first with the averaging being conducted in the last step:

$$\langle MSS \rangle = \sum_{q=1}^{\frac{Q}{2}} \sum_{p=1}^{P} \left(\frac{2}{Q} \cdot \frac{1}{P} \cdot \mathrm{iMSS}_{p,q} \right). \tag{7.14}$$

Saturation Spectra

The basic idea behind calculating saturation spectra is fairly simple and consists of applying the discrete Fourier Transform (DFT) to the slope image data. Special care has to be taken of the correct normalization of the spectra. For this work, saturation spectra are calculated from the N sequences of slope image pairs $(S_x, S_y)_{p,q}$ of length $q_{\mathrm{max}} = \frac{Q}{2}$ each according to the following routine which is based on Rocholz [2008]:

---

[6] For two matrices A, B of the same dimension $m \times n$ the Hadamard product $A \star B$ is the matrix of the same dimension as the operands with elements given by $(A \star B)_{i,j} = (A)_{i,j} \cdot (B)_{i,j}$.

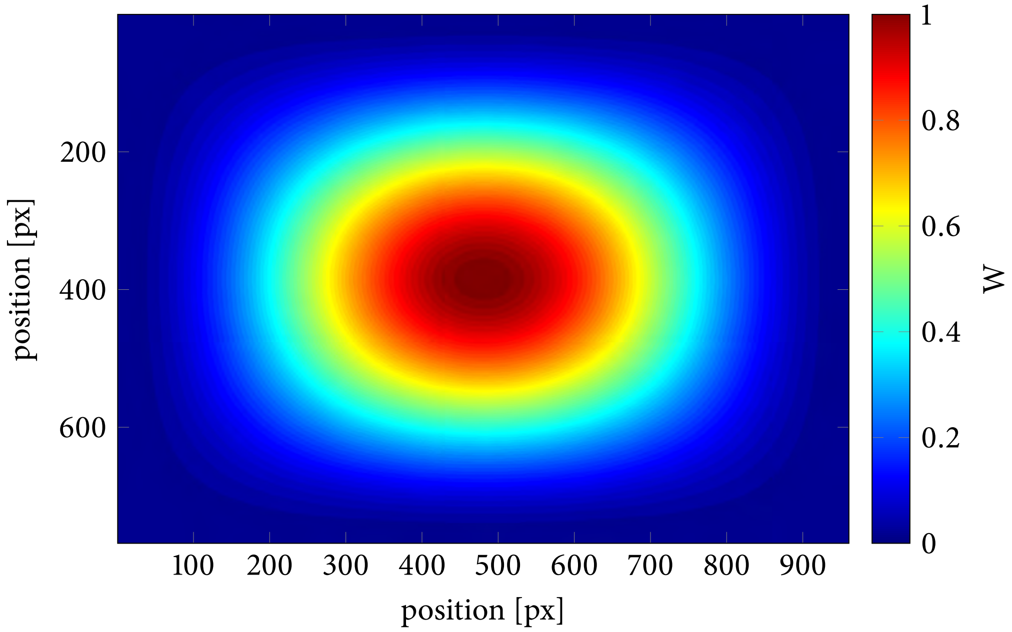

Figure 7.11.: 2D Hann window.

Wave number power spectra

- First, wave number power spectra $\mathbf{S_x}, \mathbf{S_y}$ are calculated by applying a raised cosine window[7] to the slope image pairs $(S_x, S_y)_{p,q}$, then applying the 2D-DFT and finally taking the square of the absolute value of the transformed images. Next the resulting spectra are averaged over all k images of a sequence and multiplied with a factor of f which occurs because of the energy loss due to windowing (see section 3.3). The whole step can be written as follows:

  $$\begin{aligned} &\mathbf{S_x}[W \star S_x](k_x, k_y) := f \cdot \tilde{\mathbf{S}}_\mathbf{x}[W \star S_x](k_x, k_y) \\ &:= f \cdot \sum_{q=1}^{\frac{Q}{2}} \left| \sum_{m=1}^{M} \sum_{n=1}^{N} (W \star S_x^{m,n}) \cdot \exp\left(-2\pi i \cdot \left[\frac{(k_x-1)(m-1)}{M} + \frac{(k_y-1)(n-1)}{N} \right] \right) \right|^2 \end{aligned} \tag{7.15}$$

  where $\star$ denotes the Hamard product of two matrices, W is the raised cosine window as depicted in Figure 7.11
  $W = w(M) \cdot w(N)^T = 0.5\ \left(1 - \cos\left(\frac{2\pi\cdot(0:M-1)}{(M-1)}\right)\right) \cdot 0.5\ \left(1 - \cos\left(\frac{2\pi\cdot(0:(N-1))^T}{N-1}\right)\right)$
  and $1 \leq k_x \leq M, 1 \leq k_y \leq N$.

- The factor f equals $\frac{64}{9}$. This is derived in section 3.3.

- Finally, the total wave number power spectrum components are the sum of

---

[7] also called Hann window, Hanning window or von Hann window; see section 3.3

the two components: $\mathbf{S}(k_x, k_y) \coloneqq \mathbf{S}_{\mathrm{tot}}(k_x, k_y) = \mathbf{S}_{\mathbf{x}}(k_x, k_y) + \mathbf{S}_{\mathbf{y}}(k_x, k_y)$

- Special care has to be taken concerning the correct normalization of the spectra. The total wave number power spectrum $\mathbf{S}(k_x, k_y)$ obtained in the last step is normalized with a factor $g = \frac{1}{M^2 N^2 \Delta k_x \Delta k_y}$ which is described in [Rocholz, 2008, Chapter 6.7] leading to the correctly normalized spectrum $\mathbf{S}_{\mathrm{norm}}(k_x, k_y) = g \cdot \mathbf{S}(k_x, k_y)$.

Log-polar spectra

- From the wave number power spectra on a Cartesian grid log-polar spectra are calculated because of their constant relative wavenumber resolution. For this, the wave number power spectrum $\mathbf{S}_{\mathrm{norm}}(k_x, k_y)$ is interpolated[8] onto a log-polar grid using an approach based on Rocholz et al. [2012] which results in a log-polar wave number power spectrum $\mathbf{S}(\log(k), \theta)$. The two grids are depicted in Figure 7.12. As described in Kiefhaber [2014] the drawback of this representation is that energy conservation is not guaranteed for small wave numbers.

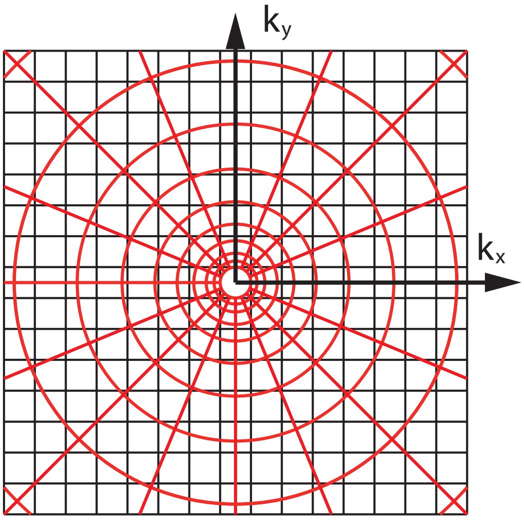

Figure 7.12.: Conversion from a Cartesian grid (black) to a log-polar (red) grid: Close to the origin, the resolution of the log-polar grid is much higher than that of the Cartesian grid. Far away from the origin, the reverse is true. Image taken from Kiefhaber [2014].

---

[8] using the Matlab® function *scatteredInterpolant*

Omnidirectional spectra

- Next, the log-polar wave number power spectrum $\mathbf{S}(\log(k), \theta)$ is integrated over all directions θ in order to obtain the omnidirectional wave number power spectrum $\mathbf{S}(\log(k))$.

Omnidirectional saturation spectra

- Finally, the omnidirectional wave number power spectrum $\mathbf{S}(\log(k))$ is multiplied with k^2 which leads to the omnidirectional saturation spectrum
$$\mathbf{B}(\log(k)) = k^2 \cdot \mathbf{S}(\log(k)). \tag{7.16}$$

8

Characterization of the Setup

Before the accuracy of the setup is explored it is of interest to examine its limitations. Therefore the temporal and spatial resolution is analysed in section 8.1. Next, section 8.2 explores the detection limits concerning mean square slope values. After that, the accuracy of the setup is explored in section 8.3.

8.1 Determination of the Frame Rate

In order to resolve all wave numbers and frequencies (which fit into the image section) in the 3D spectrum $B(\vec{k}, \omega)$ to finally obtain a dispersion relation $\omega(\vec{k})$, a certain frame rate (or sampling frequency) is necessary. The system is capable of measuring at $f_{system-limit} = 6030\,\text{Hz}$. As 4 raw images have to be taken and offset against each other, the effective temporal resolution is lowered by a factor of 4 and amounts to $f^{eff}_{system-limit} = 1507.5\,\text{Hz}$. The smallest structures that can be resolved by the measurement system are limited by the spatial resolution of the camera. Let $(\Delta x, \Delta y)$ be the size of the corresponding pixel spacing on the water surface. Then the smallest wavelengths which can be resolved are

$$\lambda_{min,x} = 2\Delta x \qquad \lambda_{min,y} = 2\Delta y.$$

$(\Delta x, \Delta y)$ can be calculated from the footprint (X, Y) of the camera image on the water surface by dividing it by the amount of pixels in the corresponding direction. For the 2013 measurements, $(X, Y) = (203\,\text{mm}, 166\,\text{mm})$ and for the 2014 measurements $(X, Y) = (227\,\text{mm}, 182\,\text{mm})$.

For gravity-capillary waves it is known that the square of the phase velocity c_{phase}

is given by

$$c_{\text{phase}}^2 = \frac{\omega^2}{k^2} = \frac{g}{k} + \frac{k \cdot \sigma}{\rho} \tag{8.1}$$

where in the case of waves at the interface of air and (pure) water $\sigma \approx 0.0727\,\mathrm{N/m}$ at 20 °C and $\rho \approx 1 \times 10^3\,\mathrm{kg/m^3}$.

Resolving this for ω yields

$$\omega(k) = \sqrt{g \cdot k + \frac{k^3 \cdot \sigma}{\rho}}. \tag{8.2}$$

From this the minimum frequency which is necessary to follow the fastest waves is calculated according to

$$f_{limit} = 2 \cdot \frac{\omega_{max}}{2 \cdot \pi} = \frac{4}{\pi} \cdot \sqrt{g \cdot \frac{2 \cdot \pi}{\lambda_{min}} + \frac{(\frac{2 \cdot \pi}{\lambda_{min}})^3 \cdot \sigma}{\rho}}. \tag{8.3}$$

Furthermore, the maximum wave number which is still resolvable by the given system is obtained from

$$k_{max,x} = \frac{2\pi}{\lambda_{min,x}} = \frac{\pi}{\Delta x} \qquad k_{max,y} = \frac{2\pi}{\lambda_{min,y}} = \frac{\pi}{\Delta y}.$$

This yields:

Exp.	Δx	Δy	$k_{max,x}$	$k_{max,y}$	$f_{limit,x}$	$f_{limit,y}$
2013	$\frac{0.203\,\mathrm{m}}{960\,\mathrm{px}}$	$\frac{0.166\,\mathrm{m}}{768\,\mathrm{px}}$	14 857 rad/m	14 535 rad/m	19 706 Hz	19 068 Hz
2014	$\frac{0.227\,\mathrm{m}}{960\,\mathrm{px}}$	$\frac{0.182\,\mathrm{m}}{768\,\mathrm{px}}$	13 286 rad/m	13 257 rad/m	16 666 Hz	16 611 Hz

The limiting frequencies are larger than the effective frequency by a factor of 11 to 13. Nevertheless, this is of no concern for the desired measurements because waves with wave numbers which correspond to these frequencies do not exist at all. Apel [1994] found that the highest wave numbers which can occur are about 6000 rad/m because above that limit, the effect of viscous damping, which scales with k^2, becomes too large. Experiments by Jähne and Riemer [1990]; Klinke [1996]; Zhang [1995] suggest a maximum wave number in the vicinity of 1000 rad/m. Rocholz [2008] argues that this might be an artefact arising from data recording and evaluation and the limit found by Apel [1994] is the correct physical quantity.

Plugging $k_{limit,exp} = 1000\,\mathrm{rad/m}$ into Equation 8.2 yields a frequency limit of $f_{limit,exp} = 366.4\,\mathrm{Hz}$ which is much lower than the system limit of the ISG. With $k_{limit,theo} = 6000\,\mathrm{rad/m}$ the frequency limit is located at $f_{limit,exp} = 5065.3\,\mathrm{Hz}$. With the given effective frame rate of the ISG, waves with a maximum wave number of

2660 rad/m can be resolved in the spectra without aliasing effects. Since the spectral energy close to 6000 rad/m is smaller than that at small wave numbers by several orders of magnitude the effects of the resulting aliasing are rather small.

Thus, in contrast to the one used by Rocholz [2008], the current ISG setup allows for measurements of wave spectra without or at least with small spatial and temporal aliasing effects.

8.2 Detection Limits

In order to analyse the detection limit for slope and mean square slope of the ISG setup, 10 zero image sequences of length 20 each[1] were taken on 30/04/2013, normalized, converted to slope and then averaged pixelwise. Afterwards the variance was calculated for each pixel and averaged over the whole image. This yields the minimum value of mean square slope which can be measured with the given setup. The reason for this is that the noise level acts as an additive offset on the physical contribution to mean square slope from the waves because variances are additive quantities. The value resulting from the calculations mentioned is $\sigma^2_{\mathrm{min}} = 3.2189 \cdot 10^{-4}$[2] (corresponding to a statistical slope measurement error of $\Delta s_{\mathrm{rms}} = 0.018$) which is a major improvement compared to the detection limit of the CISG setup of 2011 which is in the order of $\sigma^2_{\mathrm{min,CISG}} = 0.0025$ (see Kiefhaber [2014]). Yet one should bear in mind that, in a strict sense, only values much larger than the given limit represent the "real" physical value of mean square slope.

The maximum slope value that can be detected with the current setup and calibration method is given by the value at the border of a lens float lens (see section 7.1.2 for a description of the calibration process and section 5.6.1 for a description of the lens float target). It is $s_{\mathrm{max}} = \pm 0.9648$ after conversion to water equivalent slope. Absolute values of slope being larger than this limit are treated as NaN values and ignored for further evaluation leading to an underestimation of mean square slope when high slopes are present. In order to extend the range of slopes to be covered an extrapolation of the LUT is pursued. Using the MATLAB® function *scatteredInterpolant* two different extrapolation methods are examined on the alongwind component of the averaged LUT $X - LUT_{\mathrm{mean}}$ of 30/04/2013. The results are presented in Figure 8.1. It can clearly be seen that these extrapolation methods do not yield sufficient results as linearity is not preserved outside the known slope range. Thus extrapolation is not used for data evaluation for this thesis. If a target with higher slope ranges were used during the calibration process, the slope range which can be covered would ultimately be limited by the size of the light source.

---

[1] As described in section 7.1 this corresponds to a sequence length of Q=5 normalized intensity ratio images.

[2] The individual components are given by $\sigma^2_{\mathrm{min,x}} = 2.7685 \cdot 10^{-4}$ and $\sigma^2_{\mathrm{min,y}} = 4.5038 \cdot 10^{-5}$

(a) Linear method.

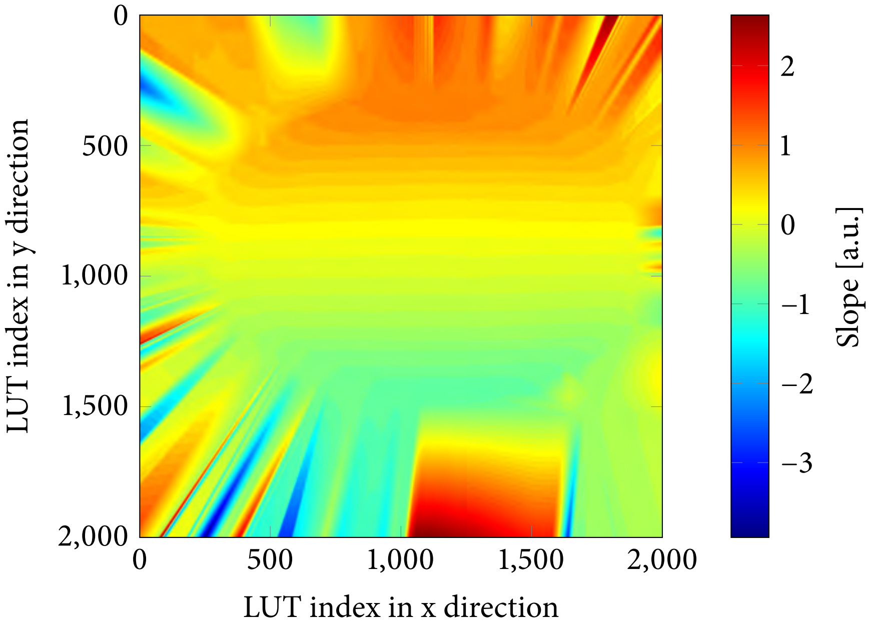

(b) Nearest Neighbour method.

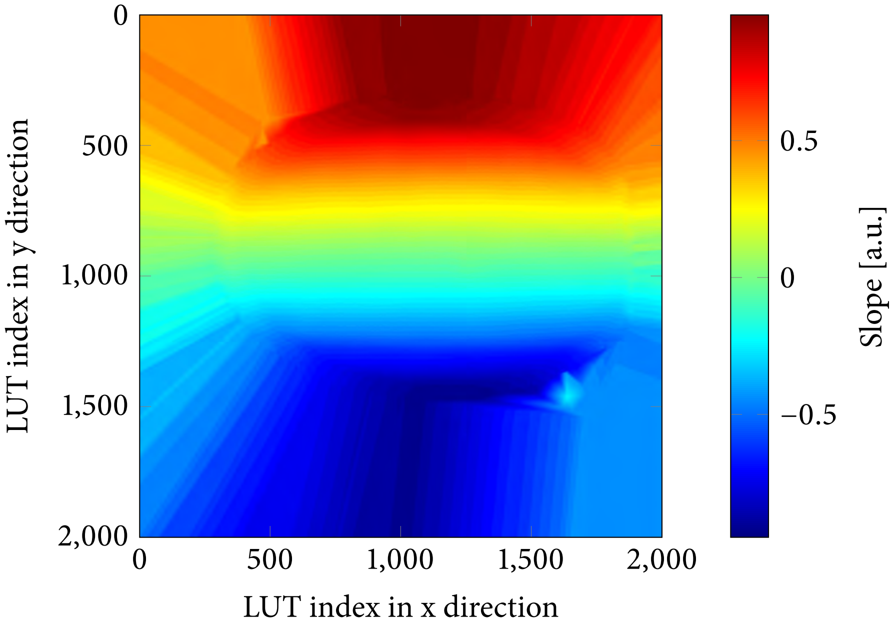

Figure 8.1.: Extrapolated LUT of 30/04/2013. Comparison of linear extrapolation and nearest neighbour extrapolation.

8.3 Accuracy of the ISG setup

The accuracy of the ISG setup is tested with specified calibration targets with known properties. The targets are described in section 5.6.

8.3.1 Lens Float Target

Figure 8.2a shows an image of the x-component of the reconstructed slope of the lens float target with slope values converted to water equivalent slope. Recalling the calibration process (section 7.1.2 and section 7.2) the LUT applied to the normalized lens float data is obtained from averaging the LUTs of many[3] single lenses detected in all lens float images of the same day. The individual LUTs are calculated from linking the normalized intensity ratios of a lens float target lens with the corresponding slope values which are known from the geometry.

In Figure 8.2b a profile through the centre of Figure 8.2a in vertical direction is depicted and Figure 8.2c shows a profile in horizontal direction.

The profile in vertical direction is expected to be constant because the same horizontal slope component is located at the same horizontal distance from the lens centre in each lens. Deviations arise because

- the lens float target is not orientated perfectly parallel to the image axes. This implies different slope values because the profile is taken at changing horizontal distance from the lens centres.
- the position of the light source is not orientated perfectly parallel to the image axes. This way the coordinate system of the image is rotated compared to that of the light source which results in isolines of constant slope being rotated, too.
- a possible position-dependency of the calibration function due to non-ideal behaviour of the optical components which has not been considered. This will be addressed in section 8.5.

The "jumps" in between the lenses which are visible in Figure 8.2b are about 0.06 ($\widehat{=}$ 3 % of the total slope range) which can be explained as follows: although the slope component in x direction remains constant the slope component in y direction is switching signs at a rather large absolute value of slope. The approximation made in Equation 5.3 leads to larger errors in the reconstructed slope then because the two slope components cannot be considered independently.

The profile in horizontal direction (Figure 8.2c) is expected to be the same for all lenses, but it is not expected to be constant but to follow the green line in Figure 8.2c which is the theoretical expectation calculated from the lens geometry according

---

[3] As described in section 7.1.2 typically more than 250 individual lens images are detected and used.

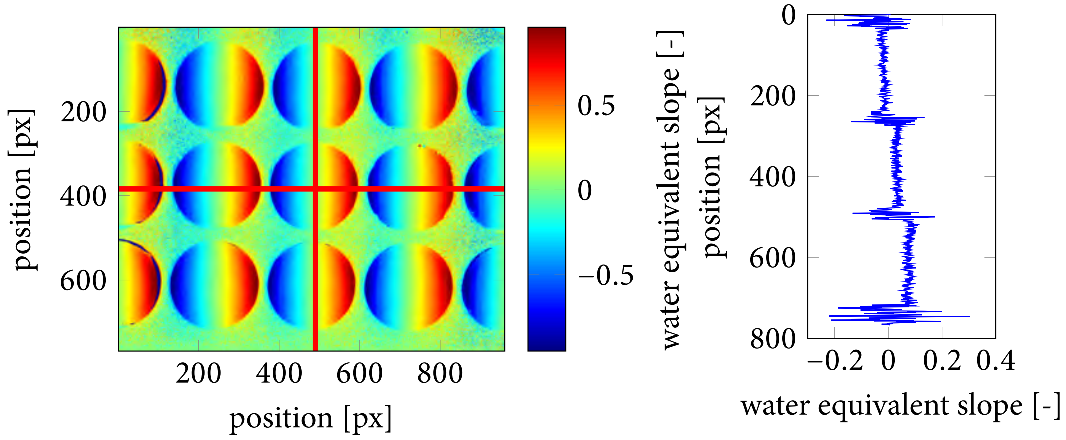

(a) Slope component in x direction. The red lines indicate the locations of the profiles.

(b) Profile in vertical direction.

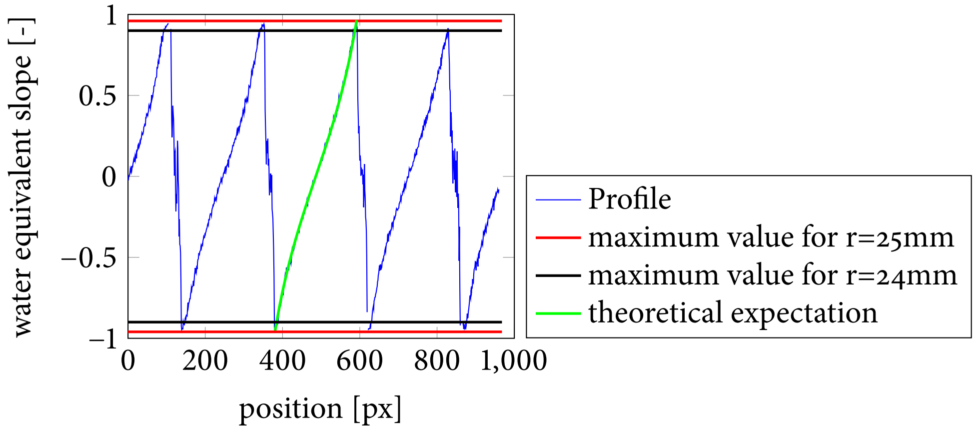

(c) Profile in horizontal direction.

Figure 8.2.: Resconstructed lens float target slope in units of water equivalent slope. LUT of 12/06/2014 applied to data of 12/06/2014.

to Equation 5.2 and Equation 5.3. From these equations the maximum value to be expected for both components of water equivalent slope is calculated as $s = 0.96$ for a lens radius of $r = 25\,\mathrm{mm}$ (red line in Figure 8.2c) and as $s = 0.90$ if we assume a lens radius of $r = 24\,\mathrm{mm}$ (black line). The two reference values are given here because of the uncertainties concerning the correct value of the visible lens radius which arise from the construction of the lens float target (see section 5.6.1 and section 8.3.2). The values obtained by applying the LUT calculated from all lens float target images of the same day are in good agreement with that.

Figure 8.3 shows the deviation of the horizontal profile of the central lens from the theoretical expectation (green line in Figure 8.2c). The standard deviation of the deviation along the profile is $\sigma = 0.0182$ which corresponds to 0.91 % of the total slope range $[-1, 1]$. Furthermore, a trend is clearly visible in the figure. The absolute value of the deviation from the theoretical expectation becomes higher with growing distance to the lens centre. This might be explained with the distance-dependent inaccuracy of the approximation made in Equation 5.3 when translating lens slope in water equivalent slope.

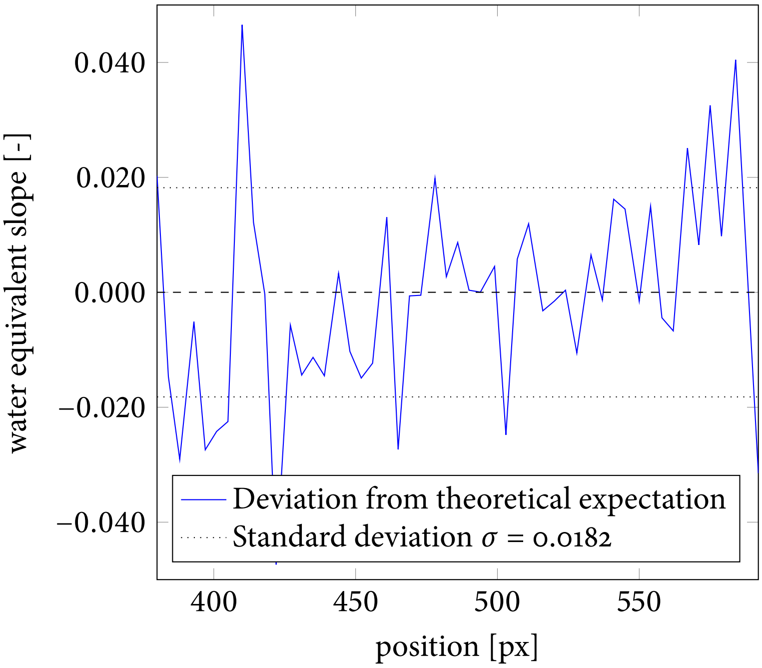

Figure 8.3.: Resconstructed lens float target slope. LUT of 12/06/2014 applied to data of 12/06/2014. Deviation from theoretical expectation.

8.3.2 Measurement of the Lens Float Target

The calibration process (see section 7.1) is based on matching the theoretically expected slope of the lens float target with an intensity ratio image of the target. Also the ISG footprint on the water surface is determined by determining the size of a lens in the image and comparing this to the size of a lens in reality. Thus, the accuracy of the calibration process depends on a correct determination of the lens radius. The lenses of the lens float target are glued into the float. This way, the visible diameter of the lenses might differ slightly from the 50 mm ± 0.1 mm which are expected as given by the lens specifications. Thus, a calliper is used in order to validate the radius of the visible part of each of the lenses. The measured diameters are given in Figure 8.4.

One of the lenses has been repaired leading to an irregular shape of the visible part of it due to excessive glue. It was excluded from all calculations. Thus, no diameter is given for this lens.

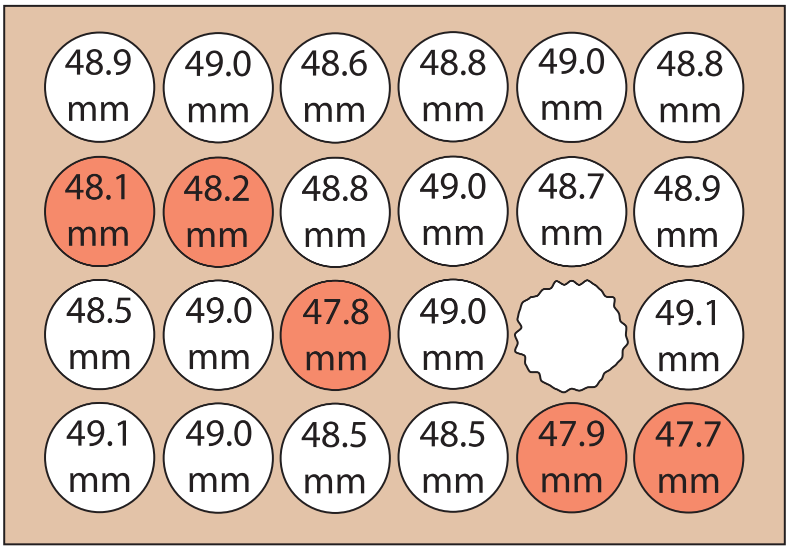

Figure 8.4.: Results of measuring the lens float target with a calliper. View from the bottom. The numbers indicate the visible diameter of the lenses in mm. Lenses marked in red are affected by shadowing effects due to their mounting.

From the measured diameters, a mean radius is calculated to be

$$\bar{r} = 24.33\,\text{mm} \;\pm\; (0.05\,\text{mm})_{\text{stat}} \;\pm\; (0.2\,\text{mm})_{\text{sys}}$$

This is a significant deviation from the expected radius of $r_{\text{ref}} = 25\,\text{mm}$. Yet it might still be possible to actually depict the entire lens due to light being refracted at the lens surface: All light rays which reach the camera sensor leave the lens in vertical direction (see section 5.2). Consider the trace of a light ray which leaves the lens right at its border (marked in green in Figure 8.5). If it has been refracted such that it is not obstructed by the lens mounting and the glue then the camera image will still depict the entire lens without shadowing effects. In the following the minimum open diameter d_{min} of mounting and glue is calculated which does not lead to an obstruction of the light rays at the border of the lens. The calculations were proposed by Balschbach [2014]. For simplicity a 2D case is considered. The lens surface slope at the border of the lens (i.e. at a distance $r_{max=25\,\text{mm}}$ from the centre) is given by Equation 5.2 as

$$\tan\alpha = \frac{r_{max}}{\sqrt{R^2 - r_{max}^2}}.$$

Furthermore Snell's law yields:

$$\sin(\beta) = \sin(\alpha)\cdot\frac{n_{air}}{n_{BK7}}. \tag{8.4}$$

Simple geometric considerations lead to the following calculation:

$$
\begin{aligned}
z &= \tan(\gamma) \cdot ET \\
&= \tan(\alpha - \beta) \cdot ET \\
&= \tan\left(\arctan\left(\frac{r_{max}}{\sqrt{R^2 - r_{max}^2}}\right) - \arcsin\left(\frac{\sin\left(\arctan\left(\frac{r_{max}}{\sqrt{R^2 - r_{max}^2}}\right)\right) \cdot n_{air}}{n_{BK7}}\right)\right) \cdot ET
\end{aligned}
\tag{8.5}
$$

where $ET = 3.55\,\mathrm{mm}$ is the edge thickness of the lenses as given by the manufacturer. Thus an open diameter of the mounting and glue of at least $d_{min} = 2 \cdot r_{max} - 2 \cdot z = 48.35\,\mathrm{mm}$ would not have any effect on the visible lens diameter. This corresponds to a radius of $r_{min} = \frac{d_{min}}{2} = 24.175\,\mathrm{mm}$. Five of the lenses of the lens float target have a smaller visible diameter and are thus affected by shadowing effects. This leads to the conclusion that calibration accuracy could be increased by choosing a different target for determining the optical resolution of the ISG. The MTF target is a good candidate its dimensions are well-known and there is no additional refraction occuring at the water surface. Another alternative is the use of a chessboard pattern.

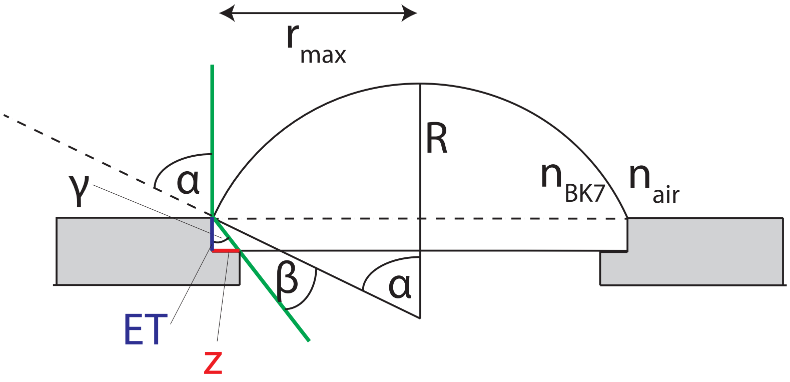

Figure 8.5.: Ray geometry at the border of a lens float lens. $ET = 3.55\,\mathrm{mm}$ is the edge thickness of the lenses as given by the manufacturer.

8.3.3 Wavelet Target

Figure 8.6 shows the reconstructed slope of the wavelet target (see section 5.6.2). Figure 8.6a gives the slope component in vertical direction which is expected to be zero if the target is aligned parallel to the image axes. Figure 8.6b depicts a profile along the red line which shows that the reconstructed slope values in y direction are close to zero indeed with a standard deviation of 0.008. The standard deviation is calculated for the left half of the profile only (pixels 7 to 508) because the black areas in the right half of the target correspond to areas where the horizontal slope component is too large to be reconstructed with the LUT obtained from the lens float target or even too large to be reached by a light ray coming from the light source and moving on towards the camera sensor. Because the horizontal slope component is too large to be included in the LUT and the LUT is calculated from both slope components the application of the LUT for slope reconstruction leads to NaN values in the vertical component, too (see section 7.2).

Figure 8.6c depicts the slope component in horizontal direction which is expected to vary according to the specification of the wavelet target (see Figure 5.9b). Along the red line a profile is drawn which is given in Figure 8.6d. The expected values for those slope components which are reconstructible with the LUT obtained from the lens float target images are shown as red lines. The expected slope values as well as the measured (reconstructed) slope values are summarized in Table 8.1. It is clearly visible that the deviation from the expected value is increasing for higher absolute values of slope. A possible explanation for that is the (spherical) aberration of the large Fresnel lens which becomes larger with increasing distance to the centre of the lens. The position where the light ray passes the Fresnel lens depends on the position in the image as well as on surface slope. Nevertheless, in general the lens is passed further away from the centre (where aberration is larger) for larger slope values.

Table 8.1.: Wavelet Target Slope: Reconstructed values, expected values and deviation; all given in units of slope. The slope segments are visible in Figure 8.6 and are numbered from left to right.

Slope Segment	**1**	**2**	**3**	**4**	**5**	**6**	**7**	**8**
Measured Slope	-0.017	-0.258	0.485	-0.791	0.955	NaN	NaN	NaN
Expected Slope	0.00	-0.25	0.50	-0.75	1.00	-1.25	1.25	-1.00
Deviation	-0.017	-0.008	-0.015	-0.041	-0.045	-	-	-

(a) Reconstructed slope component in y direction.

(b) Reconstructed slope component in y direction. Profile along red line.

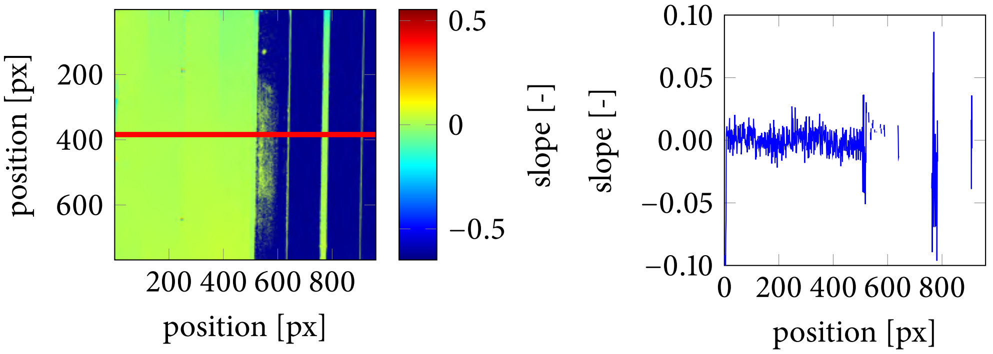

(c) Reconstructed slope component in x direction.

(d) Reconstructed slope component in x direction. Profile along red line.

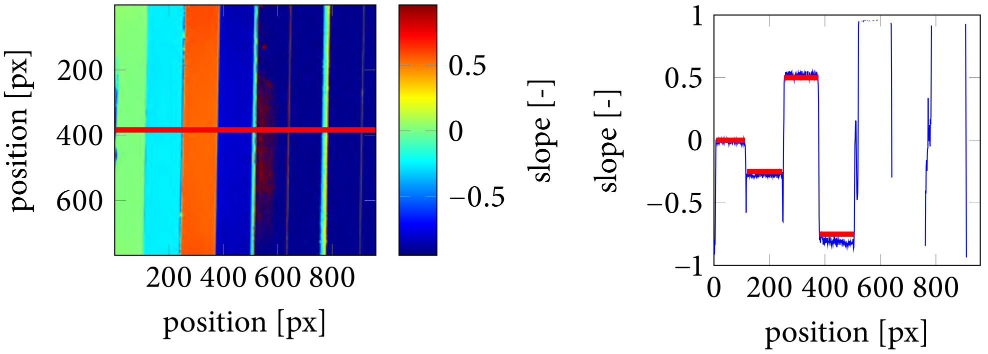

Figure 8.6.: Resconstructed wavelet target slope. LUT of 12/06/2014 applied to data of 12/06/2014.

8.3.4 Measurement of the Wavelet Target

The slope of the wavelet target was manually measured in order to investigate whether the observed deviations of the reconstructed slope values from the expectations stem from the reconstruction process or the construction of the target itself. For this purpose, a (red) laser is installed pointing vertically downwards onto the target. Then the target is tilted by an angle $\varphi = \arcsin\left(\frac{\Delta y}{\Delta x}\right)$ until the laser beam is reflected into its point of origin (see Figure 8.7). This angle equals the slope of the target at the segment where the laser point is reflected.

The length of the target was measured to be $\Delta x = 37.2\,\mathrm{cm}$. The values obtained are summarized in Table 8.2. They are in good agreement with the expected values which are also given in Table 8.2.

Table 8.2.: Measuring the wavelet target. When two values for Δy are given, the measurement was repeated to obtain an estimate for the experimental error. $\Delta x = 37.2\,\mathrm{cm}$.

segment	**distance** Δy [cm]	**angle** φ [rad]	**slope** tan φ [-]	**reference value** [-]
a	0	0	0	0.00
b	8.9; 9.2	0.24; 0.25	0.25; 0.26	0.25
c	-16.4	-0.46	-0.49	-0.50
d	22.4; 22.0	0.65; 0.63	0.75; 0.73	0.75
e	-26.1	-0.78	-0.98	-1.00
f	29.2; 29.2	0.90; 0.90	1.27; 1.27	1.25
g	-28.9	-0.89	-1.23	-1.25
h	26.4; 26.3	0.79; 0.79	1.01; 1.00	1.00
i	-22.0	-0.63	-0.73	-0.75
j	16.5; 16.5	0.46; 0.46	0.49; 0.49	0.50
k	-8.9	-0.24	-0.25	-0.25
l	0	0	0	0.00

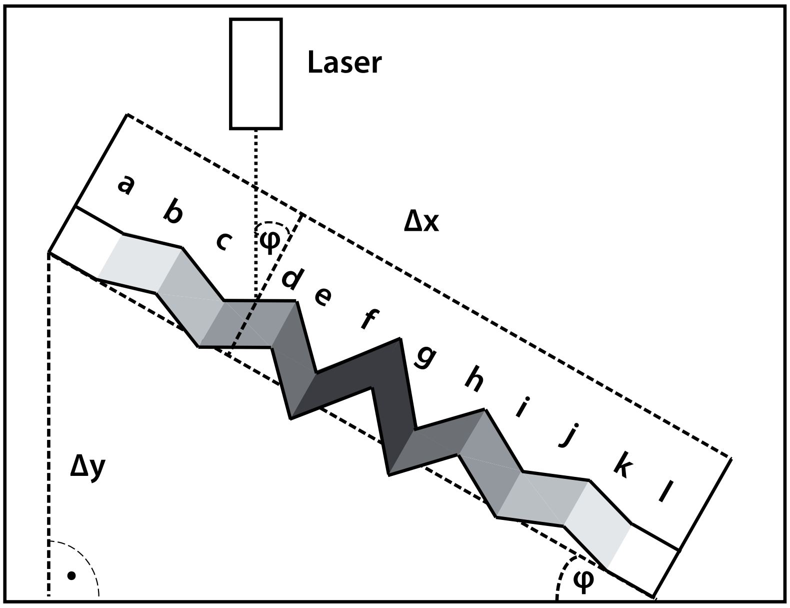

Figure 8.7.: Measuring the wavelet target using laser reflection.

8.4 Spatial Distribution of Calibration Lenses

The calibration process does not consider any spatial inhomogeneities of the setup except for those corrected by the ratio imaging. Nevertheless, spatial inhomogeneities due to the optical setup might appear as position-dependent intensity ratios of the lens float calibration target lenses. Figure 8.8 depicts the spatial distribution of the centres of the lens float calibration target lenses[4] for different days of measurement of the 2013 campaign and of 12/06/2014. One can see that the positions of the lenses relative to the whole image section are scattered rather widely, providing a spatially well averaged LUT.

The curve- and line-shaped patterns in the position images occur because the lens float calibration target is moving slowly across the field of view of the camera when a longer image sequence is taken.

Nonetheless, the dependence of the final LUT on the position of the lens float lens used for its calculation is evaluated in order to justify the use of a spatially averaged LUT. For this purpose the position dependency of the measured intensity ratio at a given slope value is evaluated in the next section.

---

[4] after manual selection, see section 7.1

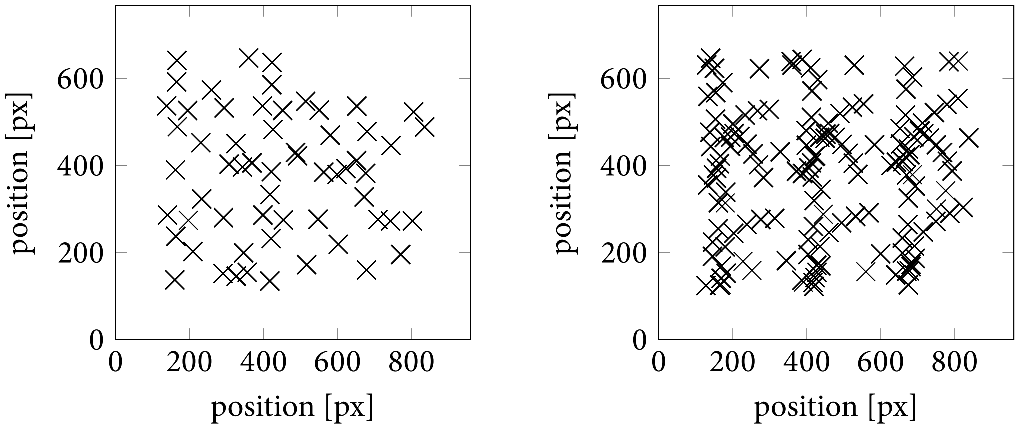

(a) Position of Lens Float Lens Centers, data of 30/04/2013

(b) Position of Lens Float Lens Centers, data of 03/05/2013

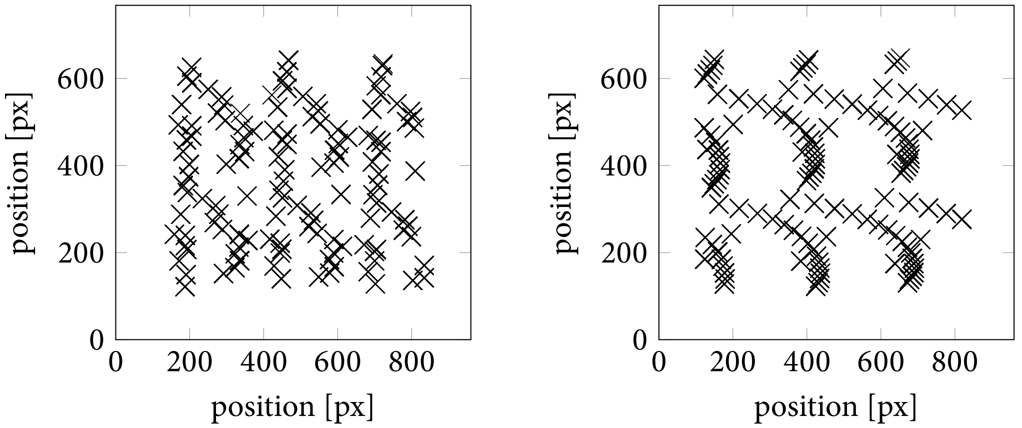

(c) Position of Lens Float Lens Centers, data of 08/05/2013

(d) Position of Lens Float Lens Centers, data of 10/05/2013

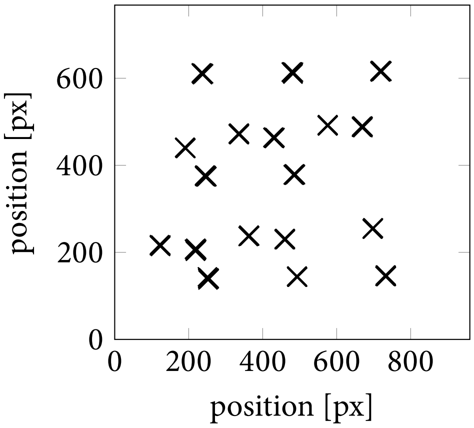

(e) Position of Lens Float Lens Centers, data of 12/06/2014

Figure 8.8.: Positions of the lens float lens centers.

8.5 Influence of the non-ideal imaging properties of the Fresnel Lens

The position dependency of the measured intensity at a given slope value is demonstrated using the lens float calibration target and a gridded foil which is placed right on top of the diffusing screen of the light source. Figure 8.9 depicts an image of the first illumination wedge *A* with setup as described. The position of the gridded foil compared to the lens centres varies slightly from lens to lens. This variation gives a qualitative impression of the distortion. As suggested by Jähne [2014] a more quantitative analysis could be performed by determining the centre of the light source[5] first and covering the whole light source with an opaque material except for a small area around this point. Then the position of the uncovered point are varied and the corresponding positions seen through the lens float lenses are evaluated depending on the position of the lens in the image.

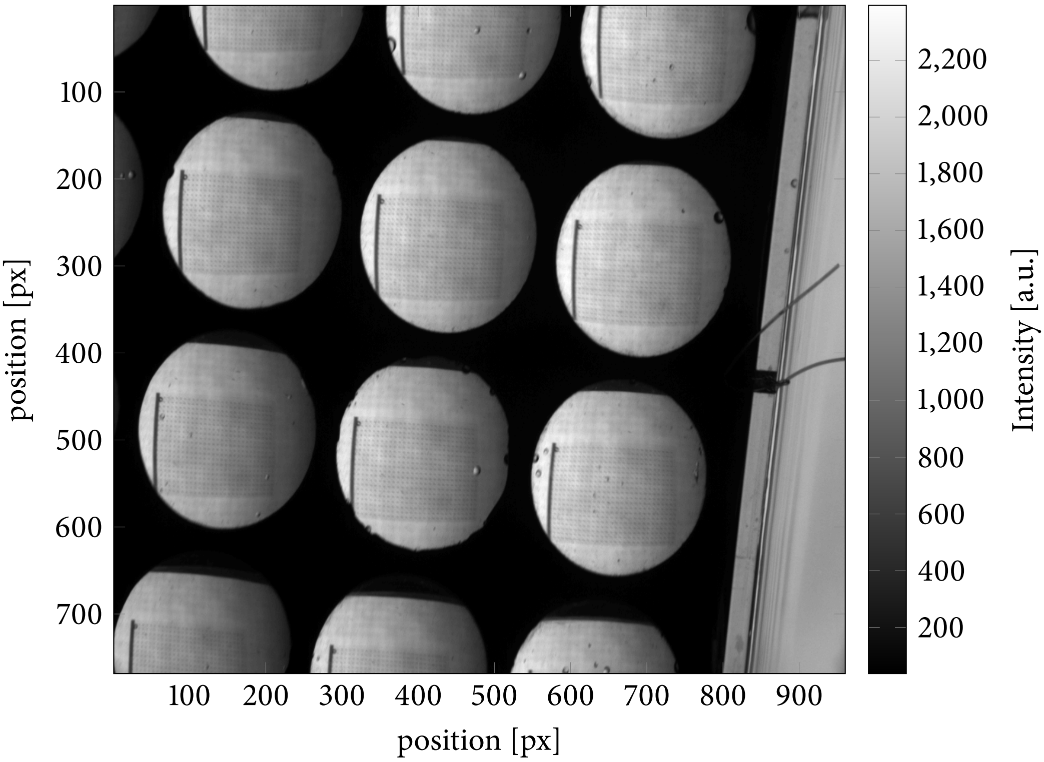

Figure 8.9.: Raw image of first illumination wedge *A* with transparent gridded foil placed on top of the light source and lens float target on the water surface. Data of 30/10/2013.

---

[5] more specifically, the point on the light source where zero slope light rays stem from

9

The Influence of Surfactants on Water Waves and Gas Transfer

In this chapter, the 2013 Aeolotron data is evaluated with a particular focus on mean square slope. Furthermore, wave slope power spectra obtained from the reconstructed slope data are presented. Since one row of LEDs of the ISG light source failed from the second day of the measurement campaign on and could not be repaired during the campaign, the LUT computed from the lens float calibration target images of the first day was used to reconstruct slope data for all conditions (see section 7.1 for a description of the reconstruction process). Since the optical setup was not modified and the mean water height was approximately constant for all days of measurement, this should have a small impact only on the results.

9.1 Surfactants and Water Wave Slope

It is expected that the presence of surfactants on the water surface influences water wave slopes (see section 2.6). In figure 9.1 example wave images are presented. The alongwind component of slope is depicted for two different amounts of surfactant and three different wind speeds each. In each column, approximately the same wind speed was present and in each row, the same surfactant was used. The top row depicts the smaller amount (and only one type) of surfactant (1 mg/l Dextran) versus the full mix surfactant in the second row, and wind speed increases from left to right. It is clearly visible that for lower wind speeds, small capillary waves are strongly suppressed by the full mix surfactants (see section 9.4). This is not the case for the Dextran condition, where small waves are visible. For the highest wind speeds, the wave fields look very similar for both conditions. For intermediate wind speeds, Data of 30/04/2013, 1 mg/l Dextran. Wind Speeds of 1.48, 3.88 and 8.42 m/s.

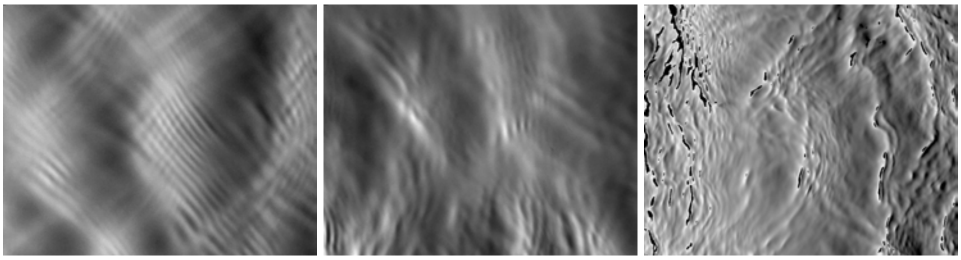

Data of 10/05/2013, full mix. Wind Speeds of 1.48, 3.88 and 8.42 m/s.

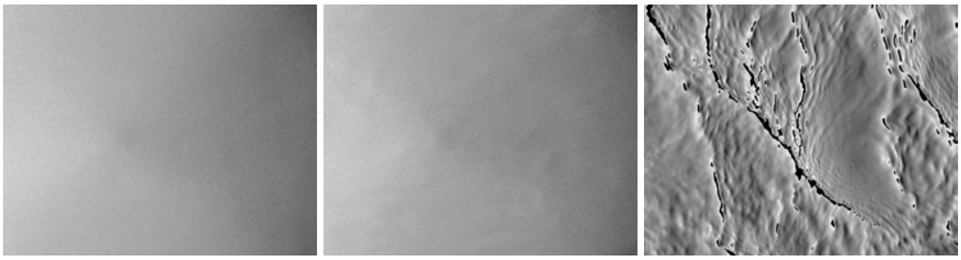

Figure 9.1.: Wave slope images measured with the ISG. Displayed is the alongwind slope component; the wind is blowing from the left.

the wave field for the Dextran condition is growing whereas the full mix condition still has a flat water surface. For the highest wind speeds, slope values outside the measuring range of the ISG occur. They are visible in black in the images. For the calculation of mean square slope, these values are ignored and do not contribute. Thus, mean square slope is underestimated for high wind speeds.

9.2 Surfactants and Mean Square Slope

Among other things, the Imaging Slope Gauge at the Heidelberg Aeolotron can be used to provide mean square slope data for the analysis of the effect of wave-suppression by surfactants on gas transfer velocities. Mean square slope has proven to yield a better parametrization of gas transfer velocities than wind speed (Frew et al. [2004]; Jähne et al. [1987]). For the 2013 Aeolotron measurements as described in section 6.1 mean square slope data has been calculated with the procedure detailed in section 8.3. Transfer velocities were provided by Krall et al. [2014] and friction velocities by Bopp and Jähne [2014]. For comparison, the results of the 2011 Aeolotron measurements as summarized in Kiefhaber [2014] are given as well.

Uncorrelated Mean Square Slope over Time

In order to obtain mean square slope values for a longer period of time, sequences of 20 raw images each were used to calculate one averaged value for mean square slope (see chapter 7). This yields approximately one value for mean square slope per 1.5 s. Mean square slope varies on smaller timescales, thus the correlation between the individual values of mean square slope calculated here is very low.

Figure 9.2 presents the resulting mean square slope values plotted over time[1] for the different wind speed conditions for the data of 08/05/2013 (full mix). Therein, the black curve is mean square slope as calculated. The red curve represents a running mean with a window size of 100 datapoints (which equals 150 s) and the orange curves gives the standard deviation with respect to the running mean. Note the different scaling of the vertical axis. The data for the other days is presented in section A.3.

The current measuring technique provides a good means to describe the wave field, although it is not suitable to make a general statement concerning the physical source of the observed patterns. In the following, an exemplary description of some noticeable patterns will be given.

The data as depicted in Figure 9.2 exhibits various patterns. The mean square slope signal remains remarkably constant for wind speeds up to 2.89 m/s. Fluctuations occur on rather small scales compared to those at higher wind speeds. This is consistent with the observation described in section 9.1 that waves with short wavelengths appear to be suppressed by the full mix surfactant. For a wind speed of 2.20 m/s some sequences were corrupted during data storage which leads to runaway values in the reconstructed mean square slope data and drastically increases the standard deviation.

For a wind speed of 3.88 m/s the running average of mean square slope remains relatively constant (in the given example, at a value of about 1.7×10^{-3}), but the standard deviation is increasing over time. This higher variability in mean square slope corresponds to a more inhomogeneous wave field. In contrast, for a wind speed of 5.11 m/s the running average of mean square slope increases over time and the standard deviation as well. For higher wind speeds, both remain relatively constant again. In combination with the increase of gas transfer velocities for this wind speed (which will be presented in section 9.4) this leads to the conclusion that the surface film was ruptured during this condition. Apparently, in the transition zone between large and small suppression of the wave field by surfactants, the variability of the wave field increases at lower wind speeds compared to mean square slope. All in all, mean square slope is higher for higher wind speeds as one expects because of the larger energy input from the wind field into the wave field.

---

[1] Note that the zero point of the time axis is the beginning of the respective wind speed condition and thus differs for each plot.

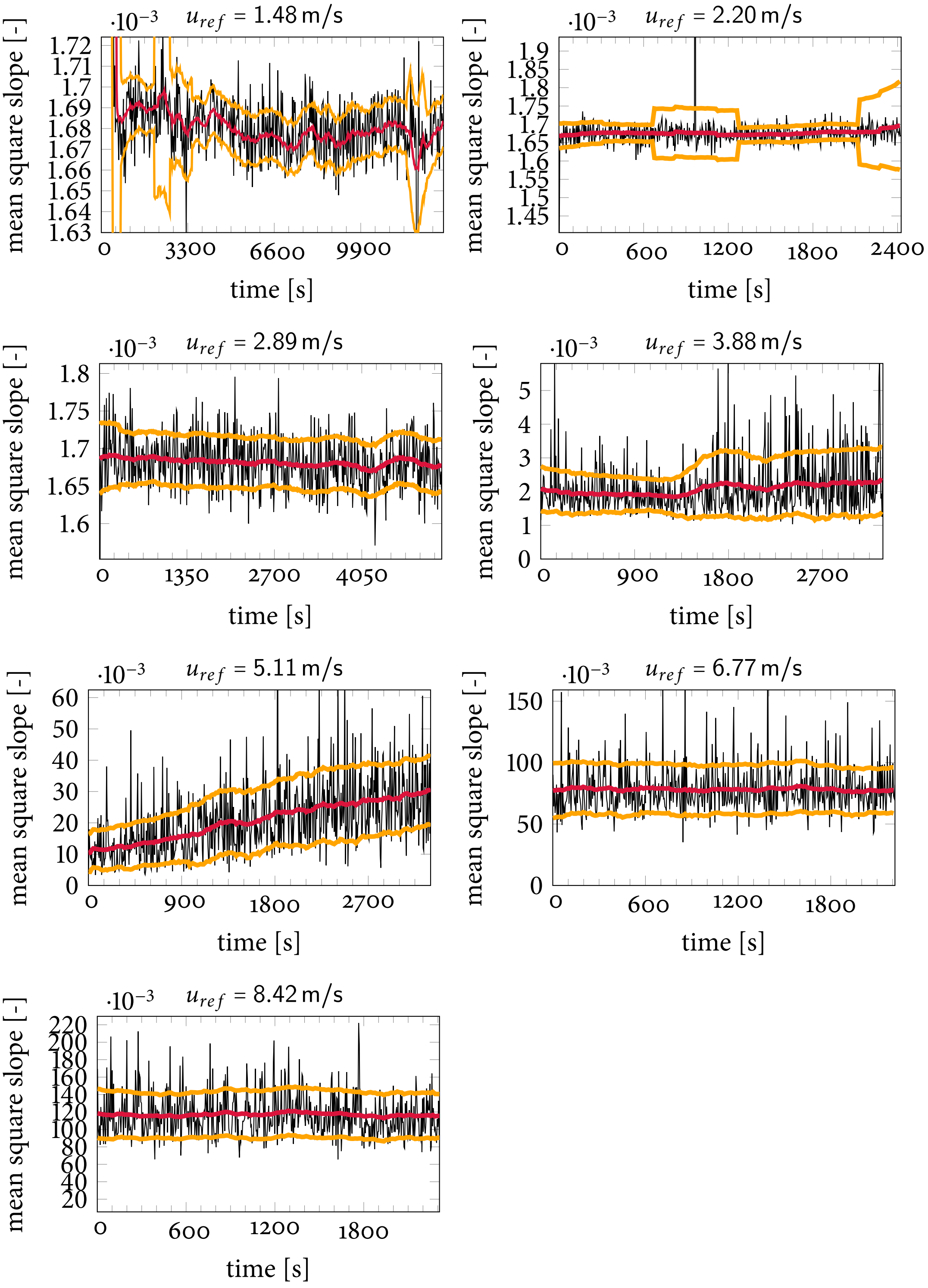

Figure 9.2.: Mean Square Slope plotted over time for different values of u_{ref}. Data of 08/05/2013 (full mix). Note the different scaling of the vertical axis. The black line gives mean square slope data, the read line gives a running mean with a window size of 150 s and the orange lines give the standard deviation.

Choice of Running Mean Window Size

In order to obtain a reliable estimate for the variability of mean square slope on longer time scales, many mean square slope data points have to be averaged over time for each dataset. The choice of the averaging period is crucial. In general, a larger averaging time yields a more constant mean value. Shorter averaging times result in higher temporal resolution. The best choice of averaging time depends on the time scale of interest. As an example, the dataset of 30/04/2013 with the lower Dextran concentration at the highest wind speed is analysed with different window sizes for the running mean. The results for two extreme cases for the window size are presented in Figure 9.3. Naturally, the running mean exhibits more variation for the smaller window size and gives almost constant values for the large window size.

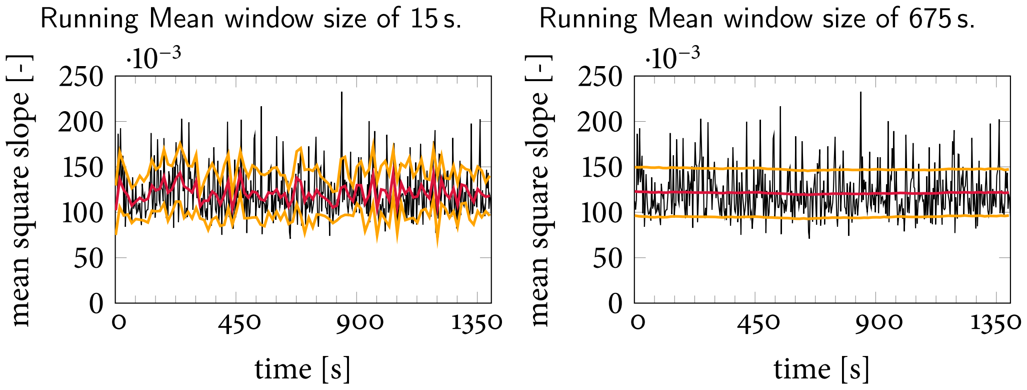

Figure 9.3.: Mean Square Slope plotted over time with different window sizes of the running mean. Data of 30/04/2013 (1 mg/l Dextran) for a wind speed of 8.42 m/s. The black line gives mean square slope data, the red line gives the running mean and the orange lines give the standard deviation.

Experimentally, a value between 100 s and 250 s has found to yield best results for the given datasets. To determine this value, the running standard deviation for mean square slope was calculated with different window sizes between 15 and 300 s for each wind speed condition of 30/04/2013. For each dataset and window size, the resulting vector was averaged. Finally, the averaged standard deviation was plotted over the window size. To facilitate the comparison between the different wind speed conditions, the value was normalized to a normalized mean standard deviation of 1. The results are given in Figure 9.4. When the normalized mean standard deviation approaches a constant value, then mean square slope varies on smaller timescales and the minimum window size to obtain a stable mean square slope value is found. For the given dataset, the normalized mean standard deviation becomes sufficiently constant in the range between 100 and 250 s.

As no temporal resolution of mean square slope is necessary for the analysis performed in the following sections, one value for mean square slope has been calculated for each wind speed and surfactant condition with the exception of the

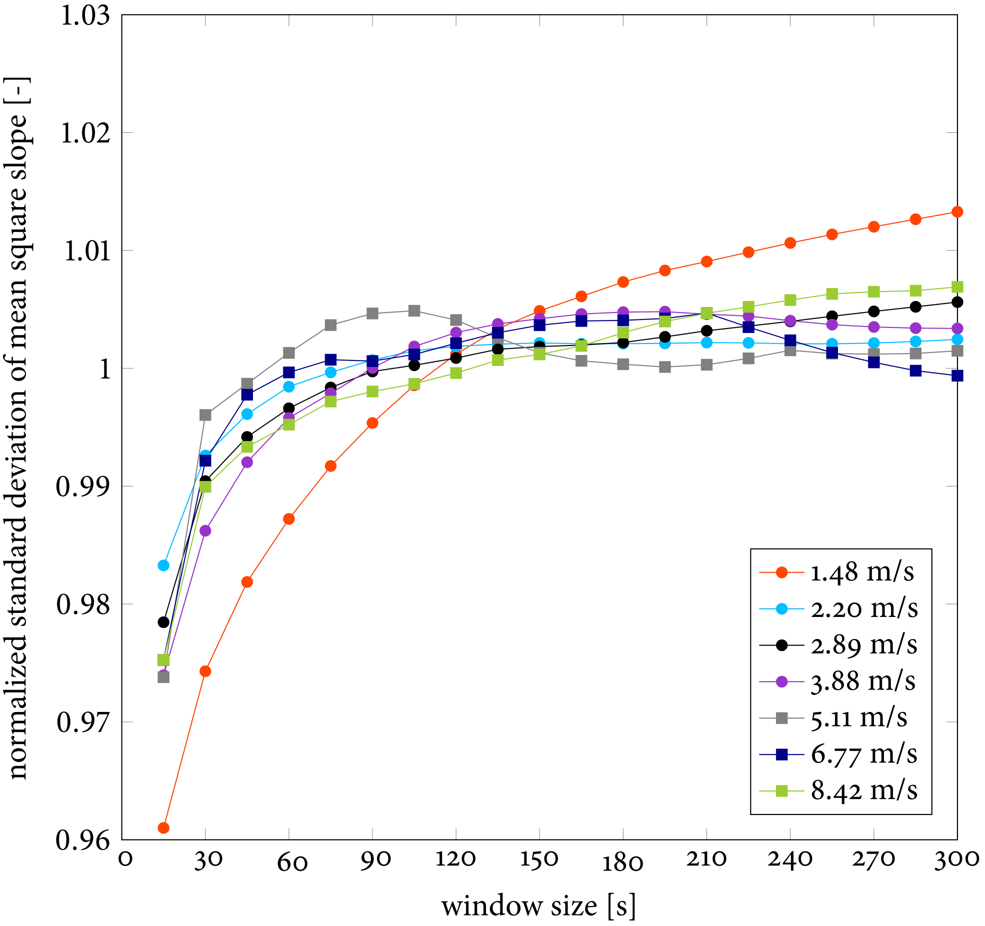

Figure 9.4.: Normalized standard deviation plotted over running mean window size for the dataset of 30/04/2013 (1 mg/l Dextran).

fifth wind speed (5.11 m/s) on 08/05/2013 and 10/05/2013 which have been parted into four parts each in order to be consistent with gas transfer velocity data. The results are summarized in section A.2.

Correlated Mean Square Slope over Time

In addition to short image sequences of 20 raw images each, long time series of surface slope were measured during the 2013 experiment. The current measuring technique allows for mean square slope measurements with a temporal resolution of up to $\Delta t = \frac{4}{6030} 1/\mathrm{s} \approx 0.66\,\mathrm{ms}$. For the measurements presented here the full temporal resolution of the ISG was exploited. One value for mean square slope is available per 0.66 ms. Thus, it is expected that the resulting time series of mean square slope are more correlated than those described in the previous section. Due to the limited amount of memory available in the camera (see section 5.3), a sequence of about 3.32 s was taken.

??–**??** in the appendix present the resulting mean square slope values plotted over time for the different experimental conditions. Here, only the dataset of 10/05/2013 is briefly discussed (Figure 9.5). Again, note the different scaling of the vertical axis.

Remarkable patterns are visible in the data of 08/05/2013 and 10/05/2013, which are the full mix surfactant cases, for wind speeds of 2.89 m/s and 3.88 m/s. In contrast to the other datasets, mean square slope varies almost periodically. Provided that small capillary waves are suppressed by the surface film and the wave field thus consists of mainly gravity waves with longer amplitudes, the frequencies occurring in the time series of mean square slope corresponds to the frequency of these waves. For the datasets mentioned above, a beat-like pattern[2] occurs. This may indicate that two frequencies close to each other make up the main part of the mean square slope time series. For all other datasets, the signal is not that regular. In Figure 9.6 the two slope components of the dataset at a wind speed of 3.88 m/s on 10/05/2013 are shown. Wave structures are clearly visible but appear to be moving in crosswind direction as well. Interestingly, this effects occurs only for the two full mix conditions which were measured on two different days at the same intermediate wind speeds. As explained later in this section, the next-highest wind speed 5.11 m/s covered with the given experiment is the wind speed where the surface film appears to rupture.

Other noticeable patterns occur for 2.20 m/s on 03/05/2013, and for 8.42 m/s on 10/05/2013 towards the end of the sequences. Here, mean square slope appears to rapidly drop to zero. This is not a physical phenomenon, but occurs due to technical difficulties during the saving process of the raw data.

---

[2] German: Schwebung

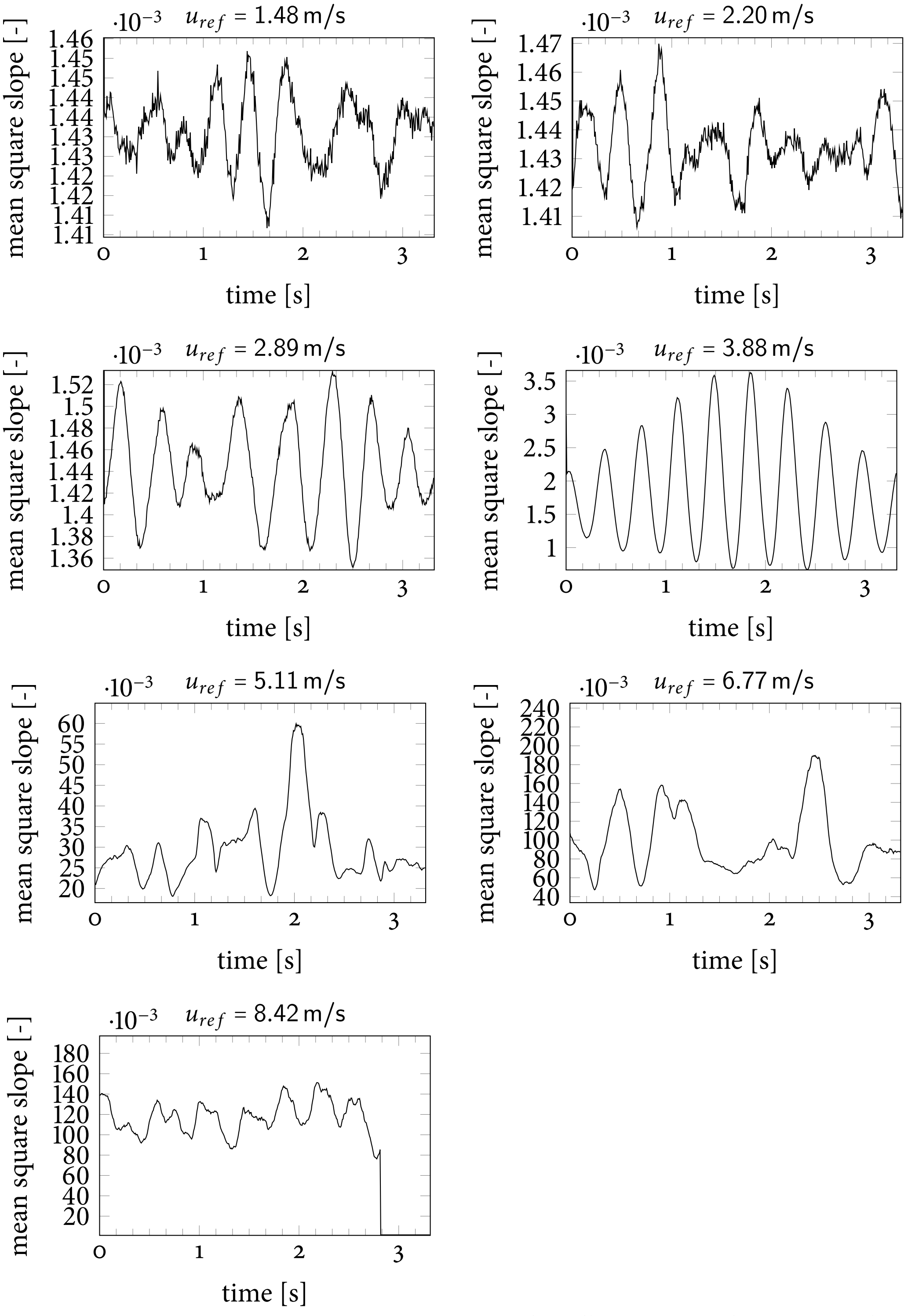

Figure 9.5.: Mean Square Slope plotted over time for different values of u_{ref}. Data of 10/05/2013 (full mix). Note the different scaling of the vertical axis.

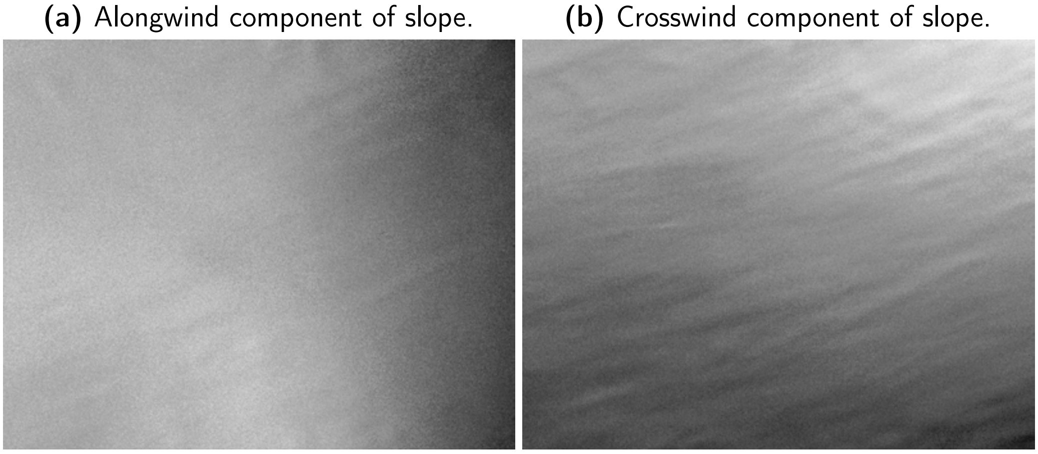

Figure 9.6.: Example for the slope components at a wind speed of 3.88 m/s on 10/05/2013 (full mix). Wave patterns are clearly visible. Alongwind direction is left-right and crosswind direction is top-bottom.

9.3 Surfactants, Mean Square Slope and Gas Transfer Velocities

In order to parametrize gas transfer velocities with mean square slope, one average mean square slope value is calculated for each wind speed condition on the four days of measurement in 2013 by averaging the uncorrelated time series. Mean square slope is plotted over the friction velocity in Figure 9.7.

Figure 9.8 shows the gas transfer velocities for nitrous oxide (N_2O) scaled to that of CO_2 at 20 °C in fresh water, k_{600}, as calculated by Krall [2013]; Krall et al. [2014] plotted over mean square slope. For comparison, k_{600} plotted over friction velocities as calculated by Bopp and Jähne [2014] is presented in Figure 9.9.

Friction velocities, gas transfer velocities for and mean square slope values as measured with the CISG and evaluated by Kiefhaber [2014] are given for the 2011 Aeolotron campaign, which is described in detail in Bopp [2011]; Kräuter [2011]; Kiefhaber [2014], for comparison in figures 9.7 to 9.9.

The error bars given for the mean square slope values for the 2013 measurements reflect the standard deviation of the mean square slope time series calculated for a window size of one (see section 9.1). This “error” arises from a physical origin rather than from the measuring device because mean square slope is a property of the wave field which varies on the timescales resolved by this measurement. The real measurement error is smaller.

Figure 9.7 shows a plot of mean square slope over the friction velocity $u_{\star,water}$. As expected, mean square slope grows with growing friction velocity. The data is in good agreement with the measurements from 2011. The full mix conditions exhibit a behaviour similar to the measurements of 2011 with the higher concentration of

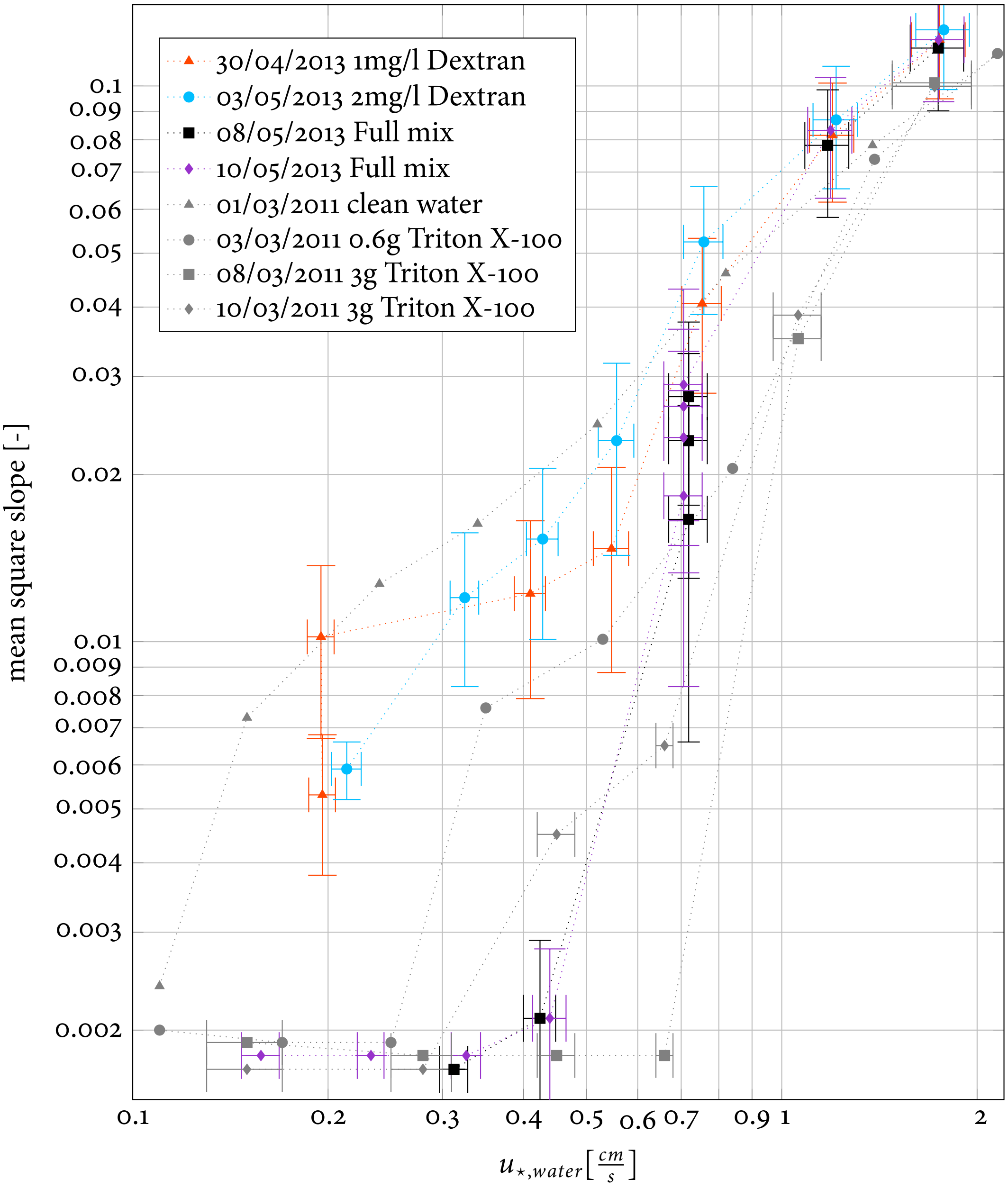

Figure 9.7.: Mean square slope plotted over friction velocity. The values for the friction velocity are preliminary results.

Triton X-100. For these conditions, mean square slope remains constantly small until a critical wind speed is reached where the surface film ruptures and a sudden increase of mean square slope occurs. For higher wind speeds, mean square slope grows in both cases. For the two Dextran conditions and low wind speeds, mean square slope is closer to the value at the clean water condition.

Surprisingly, mean square slope for the 2013 measurements is higher than the value of the 2011 clean water condition at the highest friction velocities, yet still compatible within the error tolerances. This might be due to improper calibration of the CISG used for the 2011 measurements. Reference measurements with clean water with the new ISG setup are advisable to quantify this effect.

Figure 9.8 illustrates the effect of wave suppression by surfactants (represented by mean square slope) on the gas transfer velocities k_{600}. The red line indicates a curve fit of the form $k = A \cdot (\mathrm{mss})^B$ with fit parameters $A = 479$ and $B = 1.15$ to the data of 2013. The curve was fitted to the data points with mean square slope larger than 0.015 only (red dots). Data points with blue dots were excluded from the fit. For comparison, Krall [2013] found fit parameters of $A_{2011} = 478$ and $B_{2011} = 1.11$ for the 2011 data.

Surfactants are known to modify the hydrodynamic boundary conditions at the water surface and thus to suppress waves (see section 2.6). At the same time, gas transfer velocities k are reduced compared to clean water conditions. For mean square slope values larger than ≈ 0.02, the transfer velocity correlates well with mean square slope for all surfactants shown in figure 9.8. The clean water case has slightly larger transfer velocities at a given value of mean square slope, but is still close to the surfactant cases and is compatible within the error bars. For low values of mean square slope, there is no correlation visible. For these conditions, almost no waves are present, thus energy is transferred from the wind field to the water body by the generation of shear currents only. Then waves cannot be responsible for near-surface turbulence which influences gas transfer, but the shear current is. It is not surprising that mean square slope as a parameter related to waves cannot describe the dependency of gas transfer on this process.

Figure 9.9 depicts the transfer velocity k_{600} over the friction velocity $u_{\star,water}$. As found in earlier studies [Krall, 2013] the curves connecting the individual datasets of each day of measurement differs for different surfactant concentrations. In comparison with figure 9.8, this shows that mean square slope is better suitable as a quantity to parametrize the transfer velocity k_{600} than the friction velocity is.

It is noticeable that in contrast to theoretical expectations, the mean square slope values for a Dextran concentration of 1 mg/L at a given wind speed are lower than those for a Dextran concentration of 2 mg/L (see Figure 9.7). The same effect is seen in the gas transfer velocities (Figure 9.9). A possible explanation for that is the presence of additional contaminations in the water[3] which act like surfactants and

---

[3] The water surface was not skimmed before the experiments and additional contaminations might have entered the water body during sampling procedures.

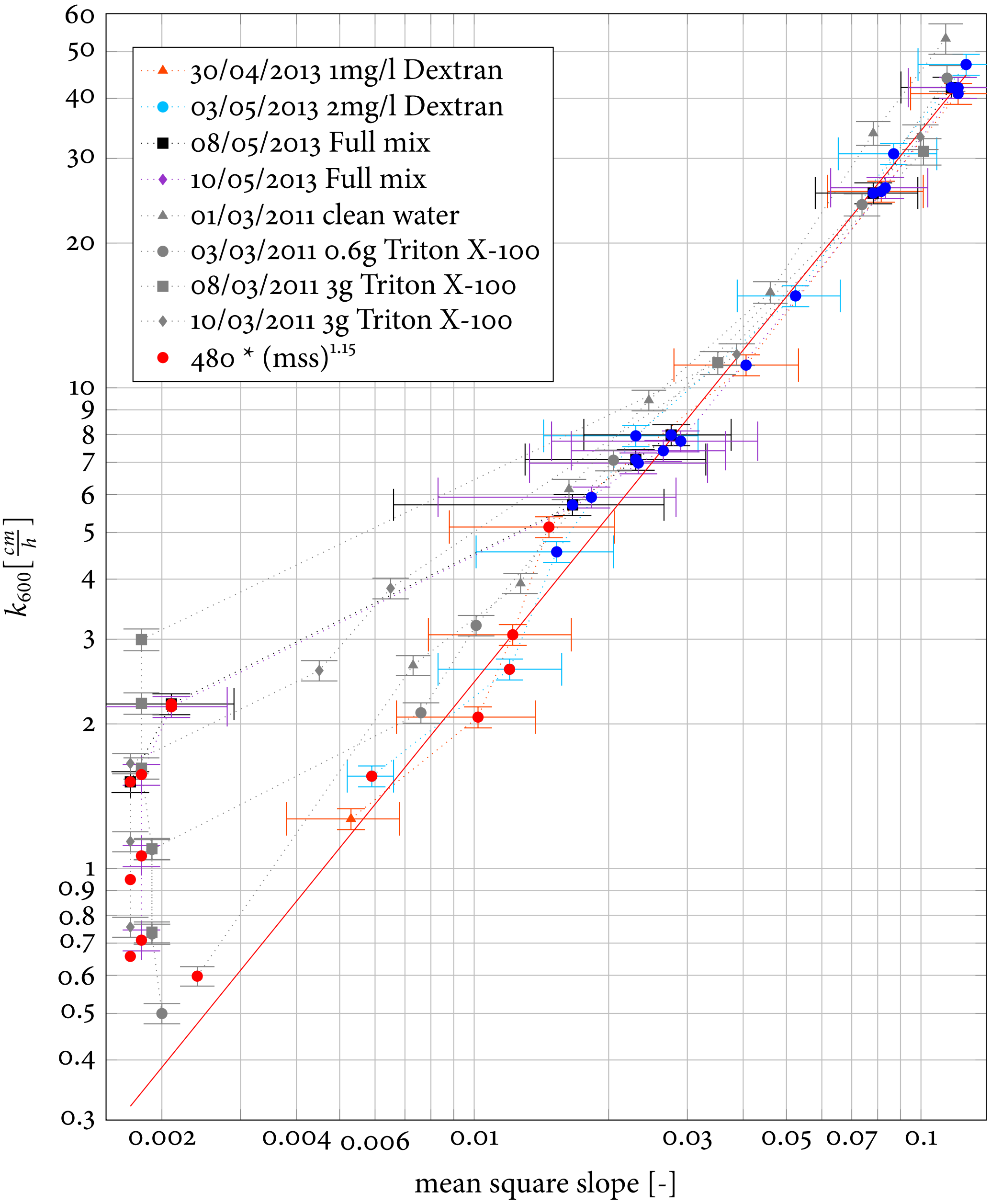

Figure 9.8.: Transfer velocity plotted over mean square slope. The values for the transfer velocity are preliminary results. The red line indicates a curve fit of the form $k = A \cdot (\text{mss})^B$ with fit parameters $A = 480$ and $B = 1.15$ to the data of 2013. The curve was fitted to the data points with mean square slope larger than 0.015 only (red dots). Data points with blue dots were excluded from the fit. For comparison, Krall [2013] found fit parameters of $A_{2011} = 478$ and $B_{2011} = 1.11$ for the 2011 data.

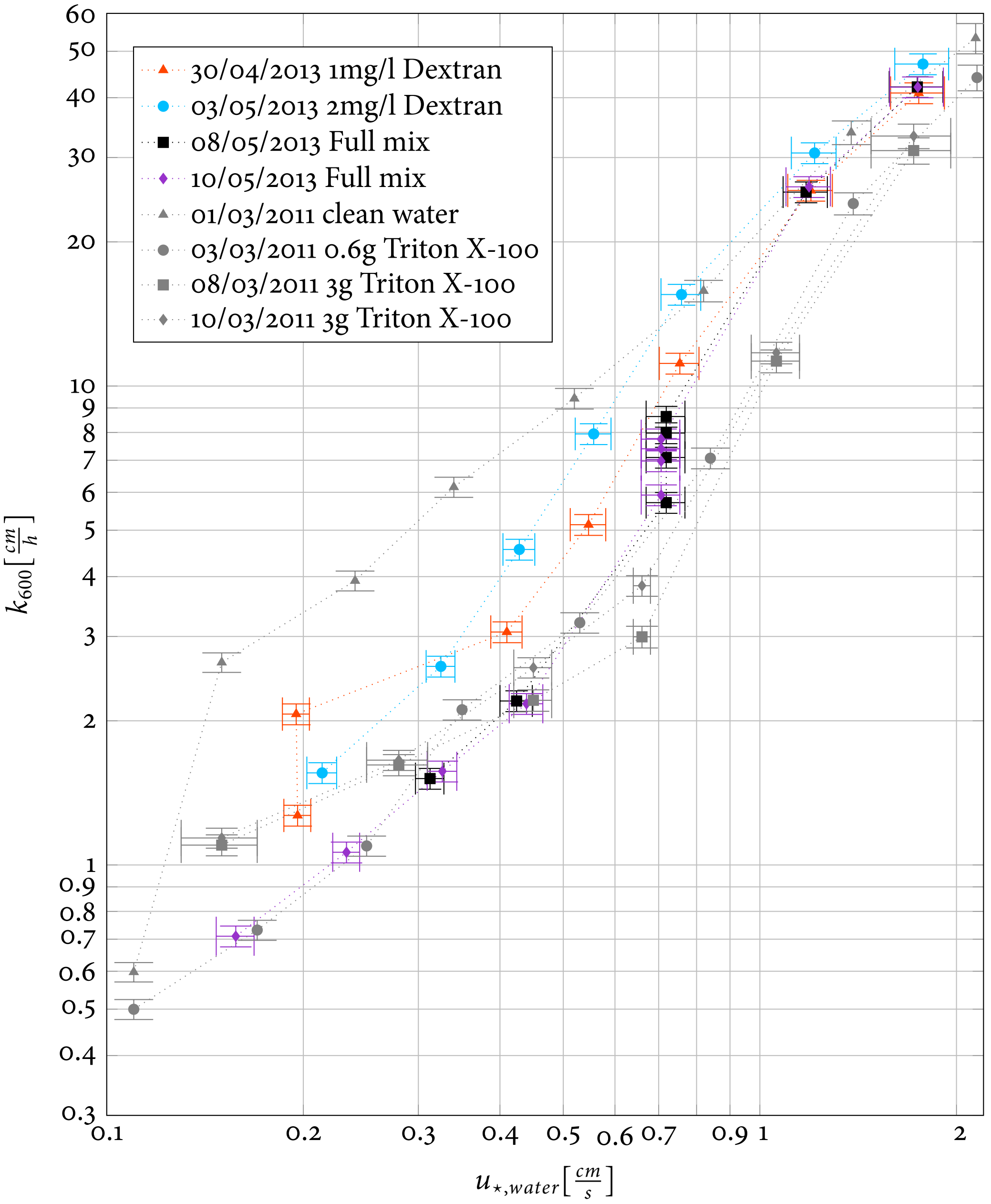

Figure 9.9.: Transfer velocity plotted over friction velocity. Preliminary results.

inhibit gas exchange and the generation of high slope waves.

All in all, the results confirm that mean square slope is a parameter which is suitable to describe gas exchange for different kinds of surfactant concentrations, especially for the higher wind speed conditions covered ($u_{\mathrm{ref}} > 6\,\mathrm{m/s}$). Mean square slope is more strongly correlated with the gas transfer velocity than friction velocity is. For lower wind speeds, the correlation is low, because gas transfer is enhanced by shear-induced turbulence which cannot be described by a wave field parameter like mean square slope.

9.4 The Effects of Surfactants on Small-scale Waves

Directional Slope Wave Number Power Spectra

At this point, slope wave number power spectra are calculated from the slope data as described in section 7.3 (see Figure 9.10a for an example). As these are hard to interpret, omnidirectional power spectra $S(k)$ are calculated from them by integrating over all directions (see section 7.3 for a description of this process). An example is provided in Figure 9.10b. Due to the large range covered and to allow for comparison with other studies (Rocholz [2008]; Kiefhaber [2014]), dimensionless omnidirectional saturation spectra $B(k) = k^2 \cdot S(k)$ (see Figure 9.10c) will be used in the following section to compare different spectra.

Omnidirectional Saturation Spectra

Omnidirectional saturation spectra are a good tool to study the suppression of the wave field by surfactants. Figure 9.11 depicts omnidirectional saturation spectra grouped by the surfactant used for seven different wind speeds each. Therein, for all surfactants, the dashed line indicates the noise level. Due to the multiplication with k^2, white noise in the slope power spectra $S(k)$ is amplified at high wave numbers $(B(k) = k^2 \cdot S(k))$.

In general, the spectral energy content of the wave field as represented by the omnidirectional saturation spectra shown here increases with wind speed as expected. The overall shape of the spectra is similar to that observed in previous studies (see Rocholz [2008]; Kiefhaber [2014] for examples).

For the two full mix conditions (Figures 9.11c to 9.11d) it is clearly visible that the surface film is intact up to the fourth wind speed condition (about 3.88 m/s, green curves) and is ruptured above 5.11 m/s (dark blue). The spectral energy content increases rapidly between these two conditions. The transition appears to be smoother for the two Dextran cases (Figures 9.11a to 9.11b). The same observation was made in the mean square slope data (Figure 9.8). Additional measurements for several wind speeds in the transition zone might help to understand the influence of rupturing surface films on water waves.

For lower wind speeds, the full mix surfactant effectively suppresses small and medium-scale waves. Compared to the two Dextran cases, wave suppression is much higher for the full mix cases. For higher wind speeds (dark blue, violet and black curves, 5.11 m/s, 6.77 m/s, 8.42 m/s), the spectra are very similar for all surfactant cases, indicating that the type of surfactant present becomes insignificant for the wave field at sufficiently high wind speeds. An explanation for that is that the surface film is mixed into the bulk water (e.g. by breaking waves) at higher wind speeds. For higher wind speeds, the spectra look very similar to the clean water case studied by Kiefhaber [2014].

(a) Logarithm of the 2D Power Spectrum $\mathbf{S}(\vec{k})$. The numbers on the axes indicate the wave number vector components k_x and k_y.

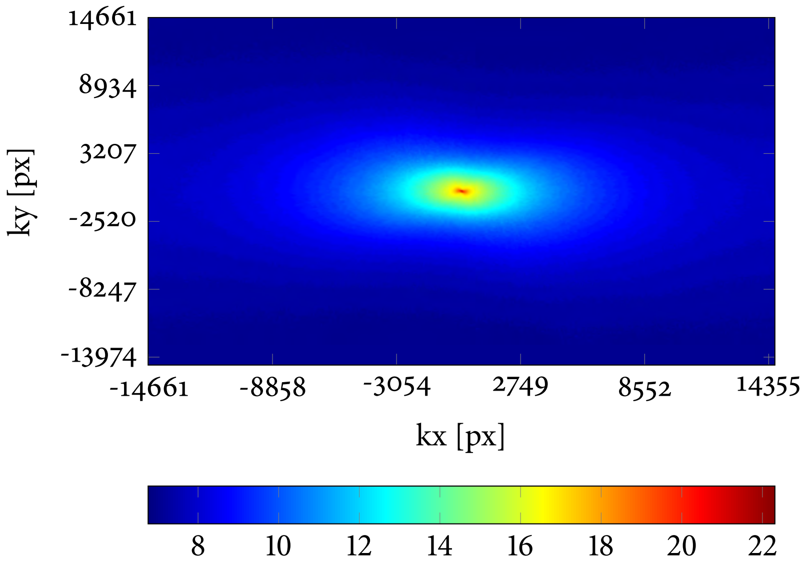

(b) Omnidirectional Power Spectrum $\mathbf{S}(k)$

(c) Omnidirectional Saturation Spectrum B(k)

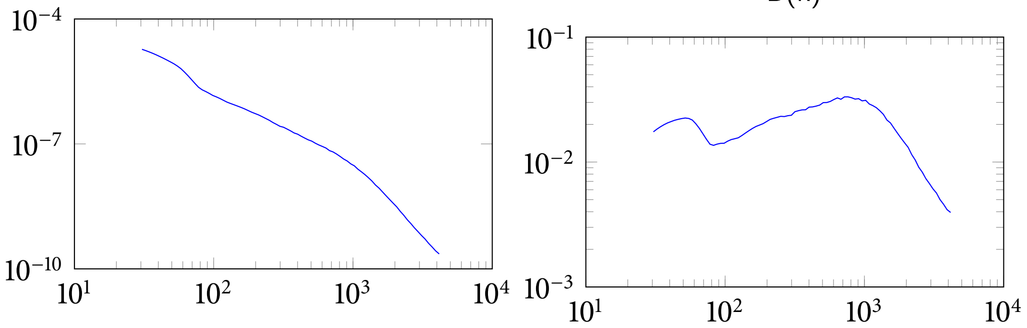

Figure 9.10.: Comparison of some different types of spectra. Data of 30/04/2013 (1 mg/l Dextran) for a wind speed of 8.42 m/s.

Compared to the measurements with Triton X-100 as evaluated by Kiefhaber [2014], the wave suppression at low wave numbers (below 100 rad/m) is less prominent. Apparently, wave suppression is less effective for the surfactants studied here compared to Triton X-100.

It is noticeable that the red curve (lowest wind speed 1.48 m/s) displays characteristic “bumps” at a k of about 2×10^2 and 5×10^2 for the first three surfactant cases. It is not visible for the last surfactant condition, which is essentially the same as the third one. It is likely to be an artifact from data evaluation without physical origin in the wave field.

For comparison, the spectra at a wind speed of 3.88 m/s and 5.11 m/s are given for all surfactant cases in Figure 9.12 (see section A.5 for the other conditions). As

(a) Data of 30/04/2013, 1 mg/L Dextran. **(b)** Data of 03/05/2013, 2 mg/L Dextran.

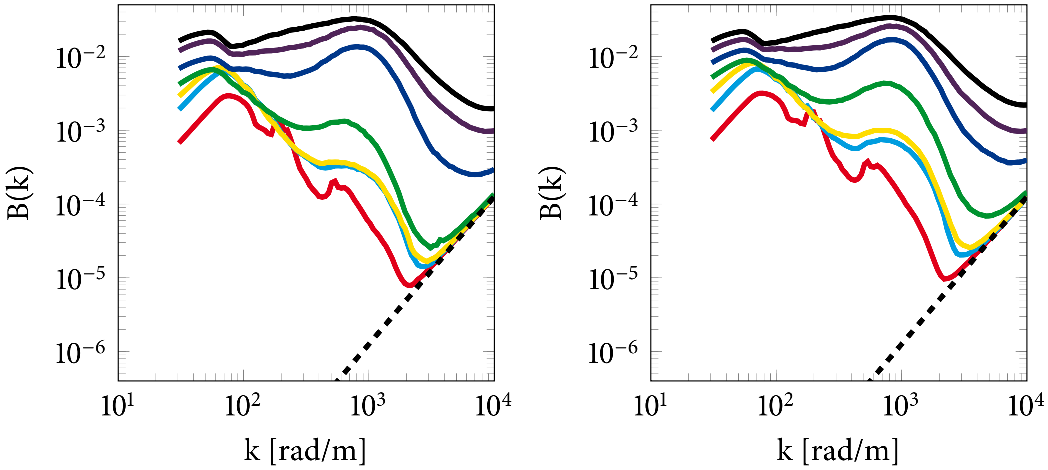

(c) Data of 08/05/2013, full mix. **(d)** Data of 10/05/2013, full mix.

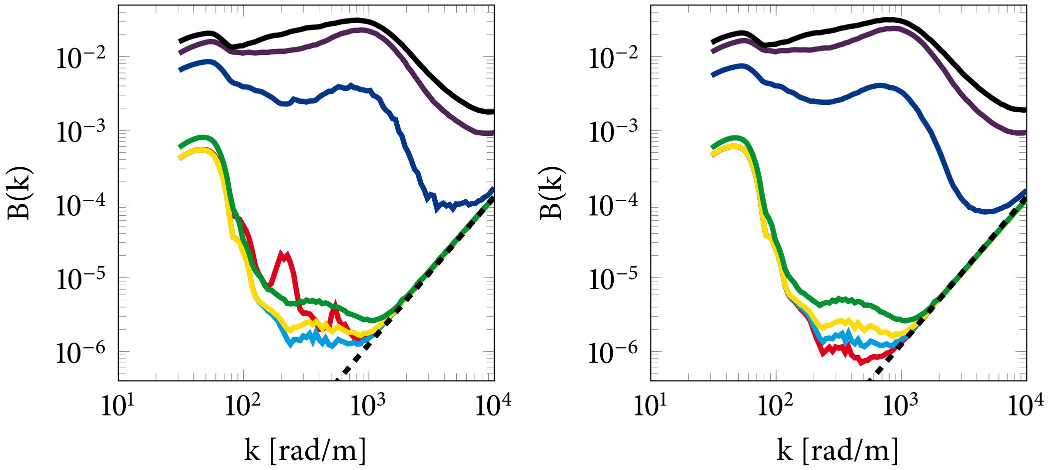

Figure 9.11.: Omnidirectional saturation spectra $B(k) = S(k) \cdot k^2$ plotted over k for the different surfactant conditions. Wind speed increases from condition 1 to condition 7 in the order red (🟥 1.48 m/s), blue(🟦 2.20 m/s), yellow(🟨 2.89 m/s), green(🟩 3.88 m/s), dark blue(🟦 5.11 m/s), violet(🟪 6.77 m/s), black(⬛ 8.42 m/s). The dashed line gives the noise level (white noise in $S(k)$).

mentioned in the previous section, the curves of the two Dextran cases appear to be the wrong way round because the spectral energy content is higher for the case with more surfactant. As before, an explanation for this phenomenon could be the pollution of the water with additional substances due to not skimming the surface. The curves for the two full mix cases were recorded on different days, but with the same surfactant concentration. Thus, they are almost identical as expected.

Furthermore, Figure 9.12 illustrates that for a wind speed of 3.88 m/s, the spectral energy content for the two Dextran cases (30/04/2013 & 03/05/2013) is much higher than that for the two full mix cases (08/05/2013 & 10/05/2013). When the surface film has ruptured for the full mix cases at a wind speed of 5.11 m/s the spectral energy content of the Dextran cases and of the full mix cases becomes almost the same, indicating that the influence of the surfactant becomes independent of the type of surfactant present[4].

All in all, the analysis of the omnidirectional saturation spectra shows that the two types of surfactant have different influences on the water waves for the concentrations used. In the full mix cases, waves are suppressed more effectively (especially in the high wave number range) than in the Dextran cases. This might be due to the insoluble components of the full mix surfactant which are not as easily mixed into the bulk water.

---

[4] Probably due to mixing into the bulk water.

(a) Condition 4. Wind speed of 3.88 m/s

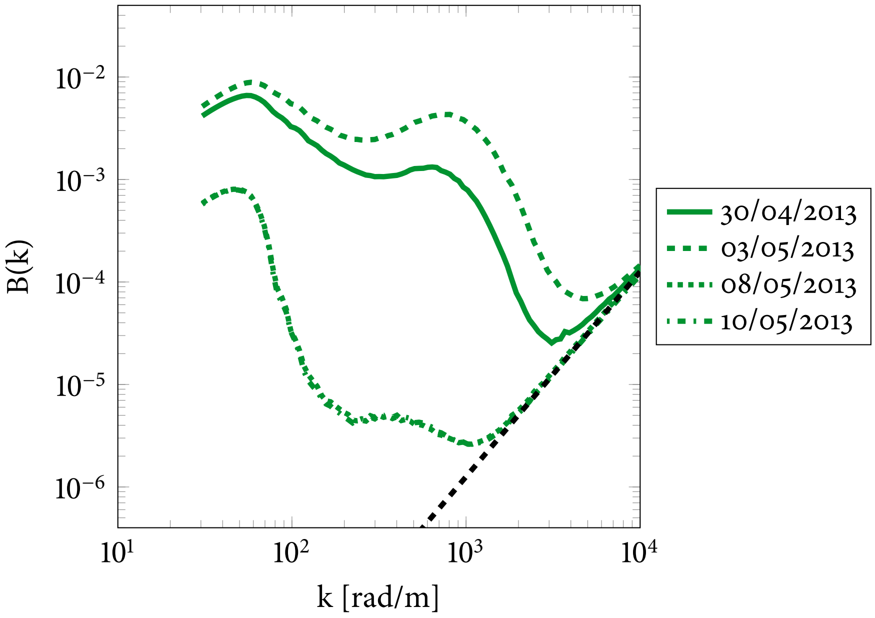

(b) Condition 5. Wind speed of 5.11 m/s

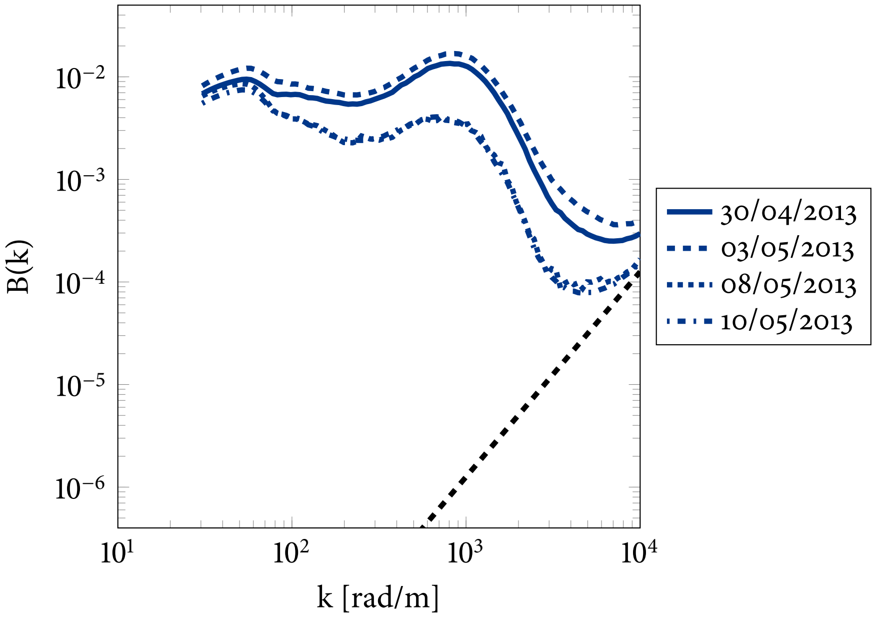

Figure 9.12.: Omnidirectional saturation spectra $B(k) = S(k) \cdot k^2$ plotted over k for conditions 4 and 5. The color code for the wind speeds is the same as in Figure 9.11.

10

Conclusion and Outlook

10.1 Conclusion

The ISG at the Heidelberg Aeolotron

In this work, the new high speed Imaging Slope Gauge at the Heidelberg Aeolotron (chapter 4 and section 5.2) has successfully been put into operation for the first time. Moreover, a data evaluation routine (chapter 7) similar to that described by Rocholz [2008] has been implemented for the new setup.

Regarding the ISG setup, the brightness of the illumination source (section 5.4) has been increased compared to the first tests described in Fahle [2013]. This allows for measurements with smaller aperture[1] and hence with improved image quality in terms of depth of field.

For the calibration procedure, a method based on a lens float calibration target (see section 5.6) has been adapted (chapter 7) and investigated (section 8.3).

The setup has been characterized regarding the range of wave numbers which can be resolved in saturation spectra (section 8.1). Thanks to the new high speed camera (section 5.3) which is installed as part of the ISG setup it is now possible to record both components of water surface slope with an unprecedented frame rate of more than 1500 Hz. With the current setup, waves with wave numbers up to 2660 rad/m can be included into saturation spectra without aliasing effects. Detection limits for slope and mean square slope (section 2.4) have been explored for the current setup (section 8.2). Compared to the old CISG setup of 2011, the detection limit for mean square slope is lowered by a factor of ≈ 10 and assumes a value of 3.2×10^{-4}. Slope

---

[1] At the moment, measurements at an f-stop of 8 are possible.

values between ±0.965 in alongwind and crosswind direction are covered by the new setup.

A spatial dependency of the calibration method remains due to the non-ideal optical imaging characteristics of the Fresnel lens, yet the resulting error appears negligible (Sections 8.4 to 8.5).

Waves and Gas Exchange in the Laboratory

The influence of different types of natural and synthetic surface films (section 2.6) on water waves has been analysed using mean square slope time series and wave number saturation spectra. Data was recorded for seven wind speed conditions with reference wind speeds between 1.48 m/s to 8.42 m/s for each surfactant.

The effect of a mixture of nature-like surfactants on water wave surface slopes has been shown to be larger[2] than that of Dextran (section 9.1) for wind speeds up to 5.11 m/s. Up to this wind speed, nature-like surfactants have been found to suppress waves, especially short- and medium-scale waves, very effectively.

The averaging time necessary to obtain a stable estimate for mean square slope was found to lie in between 100 s and 250 s (section 9.2). Furthermore, mean square slope data has been compared with data from a previous experiment at the Aeolotron with a different surfactant and clean water. The results give further evidence that, when waves are present, mean square slope is better suited for parametrizing gas transfer velocities than friction velocity is (section 9.3). In the literature, evidence is given which demands for a replacement of existing wind speed parametrizations for gas transfer velocities with other models. The present work supports with mean square slope.

For the higher wind speeds covered, the relation between mean square slope and transfer velocities has been shown to be similar for several types of soluble and insoluble surfactants.

The damping effect of surfactants on water waves has been studied using a spectral description of the wave field through wave slope saturation spectra (section 2.3, section 9.4). All in all, the results were found to be consistent with findings reported in Rocholz [2008]; Kiefhaber [2014].

---

[2] with the chosen reference concentrations

10.2 Outlook

From the technical side of view, new calibration targets which cover a higher range of slope values are desirable in order to take advantage of the full capacity of the ISG. Furthermore, the effective frame rate of the system may be increased by using a more complex illumination scheme which allows for the determination of both slope components from three raw images.

In the future, an MTF correction as examined by Rocholz [2008] for the CISG setup should be further investigated in order to obtain corrected saturation spectra for large wave numbers. With this improvement, light may be shed on the question of spectral cutoff. Furthermore, it should be analysed whether the Fourier Decomposition Method (FDM), which includes phase information as described in Troitskaya et al. [2011]; Fahle [2013], can be applied to the ISG data in order to include waves with smaller wave numbers into the spectra.

The possible future range of application for the ISG at the Aeolotron will include providing wave parameters such as mean square slope for gas exchange measurements, yet it is not limited to this. Specific experiments targeted at the understanding of wind driven water waves, especially their suppression by surfactants, can be conducted. A question of special interest, which arose during the interpretation of the results of the 2013 Aeolotron campaign, is the specification of the processes which occur in the transition zone between wind speeds where waves are largely suppressed by surfactants and wind speeds where the influence of surfactants on the wave field is diminished.

Future experiments will include combined measurements of wave parameters, gas and heat exchange, sea spray and bubble bursting with sea water at the Aeolotron which are planned for November 2014.

Bibliography

W. Alpers. The damping of ocean waves by surface films: A new look at an old problem. *J. Geophys. Res.*, 94(C5):6251–6265, May 1989.

J. R. Apel. An improved model of the ocean surface wave vector spectrum and its effects on radar backscatter. *J. Geophys. Res.*, 99:16269–16292, Aug. 1994. doi: 10.1029/94JC00846.

W. Asher, H. Liang, C. Zappa, M. Loewen, M. Mukto, T. Litchendorf, and A. Jessup. Statistics of surface divergence and their relation to air-water gas transfer velocity. *J. Geophys. Res.*, 117(C5):C05035, 2012. doi: 10.1029/2011JC007390.

J. Atwood and J. Steed. *Encyclopedia of Supramolecular Chemistry*. Number 2 in Dekker Encyclopedias Series. M. Dekker, 2004. ISBN 9780824747244.

G. Balschbach. *Untersuchungen statistischer und geometrischer Eigenschaften von Windwellen und ihrer Wechselwirkung mit der wasserseitigen Grenzschicht*. Dissertation, Institut für Umweltphysik, Fakultät für Physik und Astronomie, Univ. Heidelberg, 2000. URL `http://www.ub.uni-heidelberg.de/archiv/2473/`.

G. Balschbach. Oral communication, August 2014.

S. Banerjee. The air-water interface: turbulence and scalar exchange. In C. S. Garbe, R. A. Handler, and B. Jähne, editors, *Transport at the Air Sea Interface — Measurements, Models and Parameterizations*, pages 87–101. Springer-Verlag, 2007. doi: 10.1007/978-3-540-36906-6_6.

M. L. Banner and O. M. Phillips. On the incipient breaking of small-scale waves. *J. Fluid Mech.*, 65:647–656, 1974.

N. Barber. A diffraction analysis of a photograph of the sea. *Nature*, 164:485–485, 1949.

G. Bigg. *The Oceans and Climate*. Cambridge University Press, 2003. ISBN 9780521016346.

E. J. Bock and T. Hara. Optical measurements of ripples using a scanning laser slope gauge. In *Optics of the Air-Sea Interface*, volume 1749, page 272ff, 1992a. Part II: Data analysis and interpretation from a laboratory.

E. J. Bock and T. Hara. Optical measurements of ripples using a scanning-laser slope gauge: Part II Data analysis and interpretation from a laboratory wave tank. In *Proceedings of SPIE, Optics of the Air-Sea Interface: Theory and Measurement*, volume 272, 1992b.

E. J. Bock and T. Hara. Optical measurements of capillary-gravity wave spectra using a scanning laser slope gauge. *J. Atmos. Oceanic Technol.*, 12(2):395–403, April 1995.

E. J. Bock and J. A. Mann. On ripple dynamics II. A corrected dispersion relation for surface waves in the presence of surface elasticity. *Journal of Colloid and Interfacial Science*, 129(2):501–505, 1989.

E. J. Bock, T. Hara, N. M. Frew, and W. R. McGillis. Relationship between air-sea gas transfer and short wind waves. *J. Geophys. Res.*, 104(C11):25821–25831, 1999. ISSN 0148-0227. doi: 10.1029/1999JC900200. J NOV 15.

M. Bopp. Messung der schubspannungsgeschwindigkeit am heidelberger aeolotron mittels der impulsbilanzmethode. Bachelor thesis, Institut für Umweltphysik, Fakultät für Physik und Astronomie, Univ. Heidelberg, 2011.

M. Bopp. Luft- und wasserseitige strömungsverhältnisse im ringförmigen heidelberger wind-wellen-kanal (aeolotron). Masterarbeit, Institut für Umweltphysik, Universität Heidelberg, Germany, 2014. URL `http://www.ub.uni-heidelberg.de/archiv/17151`.

M. Bopp and B. Jähne. Measurements of the friction velocity in a circular wind-wave tank by the momentum balance method. Unpublished., 2014.

H. C. Broecker, W. Siems, and J. Petermann. The influence of wind on CO_2 exchange in a wind wave tunnel, including the effects of monolayers. *J. Marine Res.*, 36: 595–610, 1978.

K. Caldeira and M. Akai. *Ocean Storage*, chapter 6, page 442. Cambridge University Press, Cambridge, United Kingdom and New York, NY, USA, 2013. doi: 10.1017/CBO9781107415324.014. URL `http://www.ipcc.ch/`.

D. J. Carlson. Dissolved organic materials in surface microlayers: Temporal and spatial variability and relation to sea state. *Limnol. Oceanogr.*, 28(3):415–431, 1983. doi: 10.4319/lo.1983.28.3.0415.

C. Cattani and J. Rushchitsky. *Wavelet and Wave Analysis as Applied to Materials with Micro Or Nanostructure*. World Scientific Publishing Company, 2007.

G. Caulliez. The generation of the first visible wind waves. *Physics Fluids*, 10(4): 757–759, April 1998.

P. Ciais, C. Sabine, G. Bala, L. Bopp, V. Brovkin, J. Canadell, A. Chhabra, R. DeFries, J. Galloway, M. Heimann, C. Jones, C. L. Quéré, R. Myneni, S. Piao, and P. Thornton. *Carbon and Other Biogeochemical Cycles*, chapter 6, page 465–570. In IPCC [2013], 2013. doi: 10.1017/CBO9781107415324.014. URL `http://www.ipcc.ch/`.

M. Coantic. A model of gas transfer across air–water interfaces with capillary waves. *J. Geophys. Res.*, 91:3925–3943, 1986. doi: 10.1029/JC091iC03p03925.

C. Cox and W. Munk. Statistics of the sea surface derived from sun glitter. *J. Marine Res.*, 13(2):198–227, 1954a.

C. Cox and W. Munk. Measurements of the roughness of the sea surface from photographs of the sun's glitter. *J. Opt. Soc. Am.*, 44(11):838–850, 1954b.

C. S. Cox. Measurement of slopes of high-frequency wind waves. *J. Marine Res.*, 16 (3):199–225, 1958.

G. D. Crapper. An exact solution for progressive capillary waves of arbitrary amplitude. *J. Fluid Mech.*, 2:532–540, 1957. doi: 10.1017/S0022112057000348.

M. Cunliffe, R. C. Upstill-Goddard, and J. C. Murrell. Microbiology of aquatic surface microlayers. *FEMS Microbiology Reviews*, 35(2):233–246, 2011. ISSN 1574-6976. doi: 10.1111/j.1574-6976.2010.00246.x.

M. Cunliffe, A. Engel, S. Frka, B. Gasparovic, C. Guitart, J. C. Murrell, M. Salter, C. Stolle, R. Upstill-Goddard, and O. Wurl. Sea surface microlayers: A unified physicochemical and biological perspective of the air-ocean interface. *Prog. Oceanog.*, 109:104–116, 2013. doi: 10.1016/j.pocean.2012.08.004.

E. L. Deacon. Gas transfer to and across an air-water interface. *Tellus*, 29:363–374, 1977. doi: 10.1111/j.2153-3490.1977.tb00746.x.

E. B. Dobson. Measurements of the fine-scale structure of the sea. *J. Geophys. Res.*, 75:2853–2856, 1970.

M. A. Donelan and R. Wanninkhof. Gas transfer at water surfaces - conepts and issues. In M. A. Donelan, W. M. Drennan, E. S. Saltzman, and R. Wanninkhof, editors, *Gas Transfer at Water Surfaces*, pages 1–10. American Geophysical Union, 2002. doi: 10.1029/GM127p0001.

A. Dyachenko, A. Korotkevich, and V. Zakharov. Weak turbulent kolmogorov spectrum for surface gravity waves. *Physical review letters*, 92(13):134501, 2004.

P. Fahle. Hochauflösende messung der raumzeitlichen variation der neigung winderzeugter wasserwellen. Diplomarbeit, Institut für Umwelphysik, Univeristät Heidelberg, Germany, 2013.

R. Farn. *Chemistry and Technology of Surfactants*. Wiley, 2008. ISBN 9781405171793.

N. Frew, E. Bock, U. Schimpf, T. Hara, H. Haussecker, J. Edson, W. McGillis, R. Nelson, S. McKenna, B. Uz, and B. Jähne. Air-sea gas transfer: Its dependence on wind stress, small-scale roughness, and surface films. *J. Geophys. Res.*, 109:C08S17, 2004. doi: 10.1029/2003JC002131.

N. M. Frew, J. C. Goldman, M. R. Denett, and A. S. Johnson. Impact of phytoplankton-generated surfactants on air-sea gas-exchange. *J. Geophys. Res.*, 95(C3):3337–3352, 1990. doi: 10.1029/JC095iC03p03337.

N. M. Frew, D. M. Glover, E. J. Bock, and S. J. McCue. A new approach to estimation of global air-sea gas transfer velocity fields using dual-frequency altimeter backscatter. *J. Geophys. Res.*, 112:C11003, 2007. doi: 10.1029/2006JC003819.

D. Fuß. *Kombinierte Höhen- und Neigungsmessung von winderzeugten Wasserwellen am Heidelberger Aeolotron*. Dissertation, Institut für Umweltphysik, Fakultät für Physik und Astronomie, Univ. Heidelberg, Heidelberg, Germany, 2004. URL `http://www.ub.uni-heidelberg.de/archiv/4820`.

M. Gade, H. Hühnerfuss, and G. M. Korenowski, editors. *Marine Surface Films: Chemical Characteristics, Influence on Air-Sea Interactions and Remote Sensing*. Springer, Berlin, 2006. doi: 10.1007/3-540-33271-5.

B. Gašparović, M. Plavšić, B. Ćosović, and A. Saliot. Organic matter characterization in the sea surface microlayers in the subarctic norwegian fjords region. *Marine Chemistry*, 105(1-2):1 – 14, 2007. ISSN 0304-4203. doi: 10.1016/j.marchem.2006.12.010.

General Electric Plastics. Lexgard®RS-1250 ballistic laminate product datasheet. online. URL `http://www.daybrasil.com.br/produtos/construcao/img/lexgard_drs1250.pdf`.

R. S. Hansen and J. A. Mann, Jr. Propagation characteristics of capillary ripples. I. The theory of velocity dispersion and amplitude attenuation of plane capillary waves on viscoelastic films. *Journal of Applied Physics*, 35:152–158, Jan. 1964. doi: 10.1063/1.1713057.

V. Hilsenstein. *Design and Implementation of a Passive Stereo-Infrared Imaging System for the Surface Reconstruction of Water Waves*. Dissertation, Institut für Umweltphysik, Fakultät für Physik und Astronomie, Univ. Heidelberg, 2004. URL `http://www.ub.uni-heidelberg.de/archiv/4601`.

D. T. Ho, C. S. Law, M. J. Smith, P. Schlosser, M. Harville, and P. Hill. Measurements of air-sea gas exchange at high wind speeds in the southern ocean: Implications for global parameterizations. *Geophys. Res. Lett.*, 33:16611–16616, August 2006. doi: 10.1029/2006GL026817.

K. Holmberg. Natural surfactants. *Current Opinion in Colloid & Interface Science*, 6 (2):148 – 159, 2001. ISSN 1359-0294. doi: 10.1016/S1359-0294(01)00074-7.

B. A. Hughes, R. W. Grant, and R. W. Chappell. A fast response surface-wave slope meter and measured wind-wave moments. *Deep-Sea Res.*, 24:1211–1223, 1977.

P. A. Hwang. Spatial measurements of small-scale ocean waves. In B. Jähne and E. Monahan, editors, *Air-Water Gas Transfer, Selected Papers, 3rd Intern. Symp. on Air-Water Gas Transfer*, pages 153–164, Hanau, 1995. AEON. doi: 10.5281/zenodo.10571.

P. A. Hwang. A study of the wavenumber spectra of short water waves in the ocean. part ii: Spectral model and mean square slope. *J. Atmos. Oceanic Technol.*, 14(5): 1174–1186, 1997. doi: 10.1175/1520-0426(1997)014<1174:ASOTWS>2.0.CO;2.

J. Ilmberger. Impulsübertrag und Strömungsverhältnisse in einem runden Wind-Wasser Kanal. Diplomarbeit, Institut für Umweltphysik, Fakultät für Physik und Astronomie, Univ. Heidelberg, 1981. IUP D-167.

IPCC. *Climate Change 2013: The Physical Science Basis. Contribution of Working Group I to the Fifth Assessment Report of the Intergovernmental Panel on Climate Change.* Cambridge University Press, Cambridge, United Kingdom and New York, NY, USA, 2013. doi: 10.1017/CBO9781107415324.014. URL `http://www.ipcc.ch/`.

P. Janssen. *The Interaction of Ocean Waves and Wind.* Cambridge Univ Press, 2004. doi: 10.2277/0521465400.

H. Jeffreys. On the formation of water waves by wind. *Proceedings of the Royal Society of London. Series A*, 107(742):189–206, 1925.

H. Jeffreys. On the formation of water waves by wind (second paper). *Proceedings of the Royal Society of London. Series A, Containing Papers of a Mathematical and Physical Character*, pages 241–247, 1926.

I. S. F. Jones and Y. Toba. *Wind Stress over the Ocean.* Cambridge University Press, Cambridge,UK, 2001.

B. Jähne. *Zur Parametrisierung des Gasaustauschs mit Hilfe von Laborexperimenten.* Dissertation, Institut für Umweltphysik, Fakultät für Physik und Astronomie, Univ. Heidelberg, 1980. URL `http://www.ub.uni-heidelberg.de/archiv/16796`. IUP D-145, Link Nationalbibliothek http://d-nb.info/810123614.

B. Jähne. *Transfer processes across the free water interface*. Habilitation thesis, Institut für Umweltphysik, Fakultät für Physik und Astronomie, Univ. Heidelberg, 1985. URL `http://www.ub.uni-heidelberg.de/archiv/16798`. IUP D-200.

B. Jähne. Analytische Beschreibung der Bildgebung bei der kombinierten Neigungs- und Höhenmessung von Windwellen. Technical report, Interdisziplinäres Zentrum für Wissenschaftliches Rechnen und Institut für Umweltphysik, Universität Heidelberg, 2004.

B. Jähne. Oral communication, August 2014.

B. Jähne and E. Bock. Physically-based modeling of air-sea gas transfer. 2002.

B. Jähne and H. Haußecker. Air-water gas exchange. *Annu. Rev. Fluid Mech.*, 30: 443–468, 1998. doi: 10.1146/annurev.fluid.30.1.443.

B. Jähne and K. Riemer. Two-dimensional wave number spectra of small-scale water surface waves. *J. Geophys. Res.*, 95(C7):11531–11646, 1990. doi: 10.1029/JC095iC07p11531.

B. Jähne and H. Schultz. Calibration and accuracy of optical slope measurements for short wind waves. In L. Estep, editor, *Optics of the Air-Sea Interface: Theory and Measurements*, volume 1749 of *SPIE Proc.*, pages 222–233, 1992. doi: 10.1117/12.138851.

B. Jähne and S. Waas. Optical measuring technique for small scale water surface waves. In B. Jähne and S. Waas, editors, *Advanced Optical Instrumentation for Remote Sensing of the Earth's Surface from Space, SPIE Proceeding 1129, International Congress on Optical Science and Engineering, Paris, 24-28 April 1989*, pages 147–152, 1989. doi: 10.1117/12.961496.

B. Jähne, K. O. Münnich, and U. Siegenthaler. Measurements of gas exchange and momentum transfer in a circular wind-water tunnel. *Tellus*, 31:321–329, 1979. doi: 10.1111/j.2153-3490.1979.tb00911.x.

B. Jähne, K. H. Fischer, J. Ilmberger, P. Libner, W. Weiss, D. Imboden, U. Lemnin, and J. M. Jaquet. Parameterization of air/lake gas exchange. In W. Brutsaert and G. H. Jirka, editors, *Gas transfer at water surfaces*, pages 469–476, Hingham, MA, 1984a. Reidel. doi: 10.1007/978-94-017-1660-4_42.

B. Jähne, W. Huber, A. Dutzi, T. Wais, and J. Ilmberger. Wind/wave-tunnel experiments on the schmidt number and wave field dependence of air-water gas exchange. In W. Brutsaert and G. H. Jirka, editors, *Gas transfer at water surfaces*, pages 303–309, Hingham, MA, 1984b. Reidel. doi: 10.1007/978-94-017-1660-4_28.

B. Jähne, K. O. Münnich, R. Bösinger, A. Dutzi, W. Huber, and P. Libner. On the parameters influencing air-water gas exchange. *J. Geophys. Res.*, 92:1937–1950, Feb. 1987. doi: 10.1029/JC092iC02p01937.

B. Jähne, J. Klinke, and S. Waas. Imaging of short ocean wind waves: a critical theoretical review. *J. Opt. Soc. Am. A*, 11:2197–2209, 1994. doi: 10.1364/JOSAA.11.002197.

B. Jähne, H. Haußecker, U. Schimpf, and G. Balschbach. The Heidelberg Aeolotron - a new facility for laboratory investigations of small scale air-sea interaction. In *Poster presented at: The Wind-Driven Air-Sea Interface: Electromagnetic and Acoustic Sensing, Wave Dynamics and Turbulent Fluxes*, Sydney, Australia, 1999.

R. S. Kasevich. Directional wave spectra from daylight scattering. *J. Geophys. Res.*, 80:4535–4541, 1975. doi: 10.1029/JC080i033p04535.

W. C. Keller and B. L. Gotwols. Two-dimensional optical measurement of wave slope. *Appl. Optics*, 22(22):3476–3491, November 1983. doi: 10.1364/AO.22.003476.

D. Kiefhaber. Development of a reflective stereo slope gauge for the measurement of ocean surface wave slope statistics. Diplomarbeit, Institut für Umweltphysik, Fakultät für Physik und Astronomie, Univ. Heidelberg, 2010. URL `http://www.ub.uni-heidelberg.de/archiv/12673/`.

D. Kiefhaber. *Optical Measurement of Short Wind Waves — from the Laboratory to the Field.* Dissertation, Institut für Umweltphysik, Fakultät für Physik und Astronomie, Univ. Heidelberg, 2014. URL `http://www.ub.uni-heidelberg.de/archiv/16304`.

D. Kiefhaber, S. Reith, R. Rocholz, and B. Jähne. High-speed imaging of short wind waves by shape from refraction. *J. Europ. Opt. Soc. Rap. Public.*, 9:14015, 2014. doi: 10.2971/jeos.2014.14015.

B. Kinsman. *Wind Waves: Their Generation and Propagation on the Ocean Surface.* Prentice-Hall, Englewood Cliffs, 1965.

S. Kitaigorodskii. On the fluid dynamical theory of turbulent gas transfer across an air-sea interface in the presence of breaking wind waves. *J. Phys. Oceanogr.*, 14: 960–972, 1984. doi: 10.1175/1520-0485(1984)014<0960:OTFDTO>2.0.CO;2.

S. A. Kitaigorodskii. On the theory of the equilibrium range in the spectrum of wind-generated gravity waves. *J. Phys. Oceanogr.*, 13:816–827, 1983. doi: 10.1175/1520-0485(1983)013<0816:OTTOTE>2.0.CO;2.

J. Klinke. *Optical Measurements of Small-Scale Wind Generated Water Surface Waves in the Laboratory and the Field.* Dissertation, Institut für Umweltphysik, Fakultät für Physik und Astronomie, Univ. Heidelberg, 1996.

E. Kohlschütter. Die Forschungsreise S.M.S. Planet II. Stereophotogrammetrische Aufnahmen. *Annalen der Hydrographie und Maritimen Meterologie*, 34:220–227, 1906.

A. N. Kolmogorov. The local structure of turbulence in compressible turbulence for very large Reynolds numbers. *Compt.Rend.Akad.Nauk SSSR*, 30:301, 1941.

K. E. Krall. *Laboratory Investigations of Air-Sea Gas Transfer under a Wide Range of Water Surface Conditions*. Dissertation, Institut für Umweltphysik, Fakultät für Physik und Astronomie, Univ. Heidelberg, 2013. URL `http://www.ub.uni-heidelberg.de/archiv/14392`.

K. E. Krall, klaus Schneider-Zapf, S. Reith, D. Kiefhaber, and B. Jähne. Air-sea gas exchange under nature-like surfactant influence in the lab. In *7th SOPRAN Annual Meeting, Bremen, Germany, 25-26 March 2014*, 2014. doi: 10.5281/zenodo.10900.

C. Kräuter. Aufteilung des transferwiderstands zwischen luft und wasser beim austausch flüchtiger substanzen mittlerer löslichkeit zwischen ozean und atmosphäre. Diplomarbeit, Institut für Umweltphysik, Fakultät für Physik und Astronomie, Univ. Heidelberg, 2011. URL `http://www.ub.uni-heidelberg.de/archiv/13010`.

P. K. Kundu. *Fluid Mechanics*. Academic Press, Elsevier, San Diego, CA, 4th edition, 2008.

M. Kuznetsova, C. Lee, J. Aller, and N. Frew. Enrichment of amino acids in the sea surface microlayer at coastal and open ocean sites in the north atlantic ocean. *Limnol. Oceanogr.*, 49(5):1605–1619, 2004. doi: 10.4319/lo.2004.49.5.1605.

W. Laas. Photographische Messung der Meereswellen. *Zeitschr. d. Vereins Dtsch. Ingenieure*, 49:S.1889 ff. S.1937 ff. und S.1976 ff., 1905.

W. Laas. Messung der Meereswellen und ihre Bedeutung für den Schiffsbau. *Jahrbuch der Schiffsbautechn. Gesellschaft*, 7:S.391 ff., 1906.

W. Laas. Die photographische Messung der Meereswellen. *Veröff. Inst. f. Meereskunde N. F. Reihe A*, Heft 7, 1921.

J. C. Lamont and J. C. Scott. An eddy cell model of mass transfer into the surface of a turbulent liquid. *AIChE Journal*, 16:513–519, 1970. doi: 10.1002/aic.690160403.

H. Lauer. *Untersuchung der Neigungsstatistik von Wasseroberflächenwellen mittels eines schnellen, bildaufnehmenden Verfahrens*. Dissertation, IWR, Fakultät für Physik und Astronomie, Univ. Heidelberg, 1998.

V. G. Levich. *Physicochemical hydrodynamics*. Prentice-Hall (Englewood Cliffs, N.J), 1962.

D. R. Lide, editor. *CRC Handbook of Chemistry and Physics, CD-ROM Version*. CRC Press, 85 edition, 2005.

P. S. Liss and L. Merlivat. Air-sea gas exchange rates: Introduction and synthesis. In P. Buat-Menard, editor, *The role of air-sea exchange in geochemical cycling*, pages 113–129. Reidel, Boston, MA, 1986.

P. S. Liss and W. G. N. Slinn, editors. *Air-Sea Exchange of Gases and Particles*. Number 108 in NATO ASI Series C: Mathematical and Physical Sciences. Reidel, Dordrecht, 1983.

P. Lombardini, F. Piazzese, and R. Cini. The marangoni wave in ripples on an air-water interface covered by a spreading film. *Il Nuovo Cimento C*, 5(2):256–263, 1982. ISSN 0390-5551. doi: 10.1007/BF02509014.

S. R. Long and N. E. Huang. On the variation and growth of wave-slope spectra in the capillary-gravity range with increasing wind. *Journal of Fluid Mechanics Digital Archive*, 77(02):209–228, 1976.

M. S. Longuet-Higgins. Reflection and refraction at a random moving surface. i. pattern and paths of specular points. *J. Opt. Soc. Am.*, 50:838–844, Sept. 1960.

J. Lucassen. Longitudinal capillary waves. part 1.-theory. *Trans. Faraday Soc.*, 64: 2221–2229, 1968a. doi: 10.1039/TF9686402221.

J. Lucassen. Longitudinal capillary waves. part 2.-experiments. *Trans. Faraday Soc.*, 64:2230–2235, 1968b. doi: 10.1039/TF9686402230.

E. Lucassen-Reynders and J. Lucassen. Properties of capillary waves. *Advances in Colloid and Interface Science*, 2(4):347 – 395, 1970. ISSN 0001-8686. doi: 10.1016/0001-8686(70)80001-X.

S. P. McKenna and W. R. McGillis. The role of free-surface turbulence and surfactants in air-water gas transfer. *Int. J. Heat Mass Transfer*, 47:539–553, 2004. doi: 10.1016/j.ijheatmasstransfer.2003.06.001.

J. C. McWilliams, P. P. Sulliivan, and C.-H. Moeng. Langmuir turbulence in the ocean. *J. Fluid Mech.*, 334:1–30, 1997.

W. K. Melville, R. Shear, and F. Veron. Laboratory measurements of the generation and evolution of langmuir circulations. *J. Fluid Mech.*, 364:31–58, 1998. doi: 10.1017/S0022112098001098.

J. W. Miles. On the generation of surface waves by shear flows. *J. Fluid Mech.*, 3(02): 185–204, 1957. doi: 10.1017/S0022112057000567.

J. W. Miles. On the generation of surface waves by shear flows part 3. Kelvin-Helmholtz instability. *Journal of Fluid Mechanics*, 6:583–598, 11 1959a. ISSN 1469-7645. doi: 10.1017/S0022112059000842.

J. W. Miles. On the generation of surface waves by shear flows. part 2. *Journal of Fluid Mechanics*, 6:568–582, 11 1959b. ISSN 1469-7645. doi: 10.1017/S0022112059000830.

H. Mitsuyasu and E. J. Bock. The influence of surface tension. In Jones and Toba [2001], pages 242–253. ISBN 9780511552076. doi: 10.1017/CBO9780511552076.014. Cambridge Books Online.

D. Myers. *Surfactant Science and Technology*. Wiley, 2005. ISBN 9780471746065.

L. Nagel. Chemical classes of surface films and their properties. Talk at the "Gas Exchange and waves/Computer Vision " Group Seminar WS 2013/2014, 2013.

L. Nagel. *Active Thermography to Investigate Small-Scale Air-Water Transport Processes in the Laboratory and the Field*. Dissertation, Institut für Umweltphysik, Fakultät für Chemie und Geowissenschaften, Univ. Heidelberg, 2014. URL `http://www.ub.uni-heidelberg.de/archiv/16831`.

R. Nielsen. *Gasaustausch - Entwicklung und Ergebnis eines schnellen Massenbilanzverfahrens zur Messung der Austauschparameter*. Dissertation, Institut für Umweltphysik, Fakultät für Physik und Astronomie, Univ. Heidelberg, 2004. URL `http://www.ub.uni-heidelberg.de/archiv/5032`.

P. D. Nightingale, G. Malin, C. S. Law, A. J. Watson, P. S. Liss, M. I. Liddicoat, J. Boutin, and R. C. Upstill-Goddard. In situ evaluation of air-sea gas exchange parameterization using novel conservation and volatile tracers. *Global Biogeochem. Cycles*, 14:373–387, 2000. doi: 10.1029/1999GB900091.

pco.dimax datasheet. PCO AG, Kelheim. URL `http://www.pco.de/fileadmin/user_upload/db/products/datasheet/BR_pco_dimax_104.pdf`.

O. M. Phillips. On the generation of waves by turbulent wind. *Journal of fluid mechanics*, 2(05):417–445, 1957.

O. M. Phillips. The equilibrium range in the spectrum of wind-generated waves. *J. Fluid Mech.*, 156:426–434, 1958.

O. M. Phillips. *The Dynamics of the Upper Ocean*. Cambridge University Press, 2 edition, 1977.

O. M. Phillips. Spectral and statistical properties of the equilibrium range in wind-generated gravity waves. *J. Fluid Mech.*, 4:426–434, 1985.

C. Prettyman and M. Cermak. Time variation of the rough ocean surface and its effect on an incident laser beam. *Geoscience Electronics, IEEE Transactions on*, 7 (4):235–243, Oct 1969. ISSN 0018-9413. doi: 10.1109/TGE.1969.271357.

A. Pushkarev, D. Resio, and V. Zakharov. Weak turbulent approach to the wind-generated gravity sea waves. *Physica D: Nonlinear Phenomena*, 184(1):29–63, 2003.

T. Reinthaler, E. Sintes, and G. J. Herndl. Dissolved organic matter and bacterial production and respiration in the sea-surface microlayer of the open atlantic and the western mediterranean sea. *Limnol. Oceanogr.*, 53(1):122–136, 2008. doi: 10.4319/lo.2008.53.1.0122.

I. Robb. Determination of the aqueous solubility of fatty acids and alcohols. *Australian Journal of Chemistry*, 19:2281–2284, 1966. doi: http://dx.doi.org/10.1071/CH9662281.

R. Rocholz. *Spatiotemporal Measurement of Short Wind-Driven Water Waves*. Dissertation, Institut für Umweltphysik, Fakultät für Physik und Astronomie, Univ. Heidelberg, 2008. URL `http://www.ub.uni-heidelberg.de/archiv/8897`.

R. Rocholz, P. Fahle, and B. Jähne. High speed and high resolution wave imaging to investigate the initial generation of wind waves at very small fetch. WISE (Waves In Shallow Environments) 2012, 19th International Conference, Barcelona, Spain, 16-20 April 2012. URL `http://hci.iwr.uni-heidelberg.de/publications/dip/MISC/WISE_2012_rrocholz/2012_WISE_rrocholz_noVideos.pdf`.

C. L. Sabine, R. A. Feely, N. Gruber, R. M. Key, K. Lee, J. L. Bullister, R. Wanninkhof, C. S. Wong, D. W. R. Wallace, B. Tilbrook, F. J. Millero, T.-H. Peng, A. Kozyr, T. Ono, and A. F. Rios. The ocean sink for anthropogenic CO_2. *Science*, 305: 367–372, 2004.

A. H. Schooley. A simple optical method of measuring the statistical distribution of water surface slopes. *J. Opt. Soc. Am.*, 44(37), 1954.

A. Schuhmacher. Stereophotogrammetrische Wellenaufnahmen. In *Wissenschaftliche Ergebnisse der Deutschen Atlantischen Expedition auf dem Forschungs- und Vermessungsschiff "Meteor" 1925–1927*, volume 7, part 2. de Gruyter, Berlin, 1939.

J. C. Scott. The influence of surface-active contamination on the initiation of wind waves. *Journal of Fluid Mechanics*, 56:591–606, 12 1972. ISSN 1469-7645. doi: 10.1017/S0022112072002538.

D. Shah. *Micelles: Microemulsions, and Monolayers: Science and Technology*. Taylor & Francis, 1998. ISBN 9780824799908.

C. E. Shannon. Communication in the presence of noise. *Proc.Institute of Radio Engineers*, 37(1):10–21, 1949.

Sigma Aldrich. Sigma aldrich product information sheet triton x-100. online, 1999. URL `https://www.sigmaaldrich.com/content/dam/sigma-aldrich/docs/Sigma/Product_Information_Sheet/1/t8532pis.pdf`.

R. L. Snyder, F. W. Dobson, J. A. Elliott, and R. B. Long. Array measurements of atmospheric pressure fluctuations above surface gravity waves. *J. Fluid Mech.*, 102 (-1):1–59, 1981. doi: 10.1017/S0022112081002528.

J. Stapf. Bestimmung der dynamischen oberflächenspannung mit hilfe der blasendruckmethode. Diplomarbeit, Institut für Umweltphysik, Fakultät für Physik und Astronomie, Univ. Heidelberg, 2010.

D. J. Stilwell. Directional energy spectra of the sea from photographs. *J. Geophys. Res.*, 74:1974–1986, 1969. doi: 10.1029/JB074i008p01974.

G. G. Stokes. On the theories of the internal friction of fluids in motion, and of the equilibrium and motion of elastic solids. *Transactions of the Cambridge Philosophical Society*, 8(II):287–319, 1849.

T. Takahashi, S. Sutherland, R. Wanninkhof, C. Sweeney, R. Feely, D. Chipman, B. Hales, G. Friederich, F. Chavez, C. Sabine, et al. Climatological mean and decadal change in surface ocean pCO_2, and net sea-air CO_2 flux over the global oceans. *Deep Sea Research Part II: Topical Studies in Oceanography*, 56:554–577, 2009. doi: doi:10.1016/j.dsr2.2008.12.009.

M. A. C. Teixeira and S. E. Belcher. On the distortion of turbulence by a progressive surface wave. *J. Fluid Mech.*, 458:229–267, May 2002.

N. Tepić, B. Gašparović, and M. Ahel. Multivariate statistical analysis of the distribution patterns of carbohydrates and surface-active substances in the northern adriatic sea. *Marine Chemistry*, 114(1-2):37 – 46, 2009. ISSN 0304-4203. doi: http://dx.doi.org/10.1016/j.marchem.2009.03.005.

Y. Troitskaya, D. Sergeev, O. Ermakova, and G. Balandina. Statistical parameters of the air turbulent boundary layer over steep water waves measured by the PIV technique. *J. Phys. Oceanogr.*, 41:1421–1454, 2011. doi: 10.1175/2011JPO4392.1.

W.-T. Tsai, S.-M. Chen, G.-H. Lu, and C. Garbe. Characteristics of interfacial signatures on a wind-driven gravity-capillary wave. *J. Geophys. Res.*, 118:1715–1735, 2013. doi: 10.1002/jgrc.20145.

K. Tsujii. *Surface activity: principles, phenomena, and applications*. Series in polymers, interfaces, and biomaterials. Academic Press, 1998. ISBN 9780127022802.

N. van Os. *Nonionic Surfactants: Organic Chemistry*. Surfactant Science. Taylor & Francis, 1997. ISBN 9780824799977.

F. Veron and W. Melville. Remote observations of the initial generation of surface waves. In *Geoscience and Remote Sensing Symposium, 2001. IGARSS '01. IEEE 2001 International*, volume 2, pages 961–963, Sydney, NSW, Australia, 2001a. doi: 10.1109/IGARSS.2001.976694. Meeting Date: 07/09/2001 - 07/13/2001 ISBN: 0-7803-7031-7.

F. Veron and W. K. Melville. Experiments on the stability and transition of wind-driven water surfaces. *J. Fluid Mech.*, 446:25–65, 2001b. doi: 10.1017/S0022112001005638.

S. Waas and B. Jähne. Combined slope-height measurements of short wind waves: first results from field and laboratory measurements. In L. Estep, editor, *Optics of the Air-Sea Interface: Theory and Measurements*, volume 1749 of *SPIE Proc.*, pages 295–306, 1992. doi: 10.1117/12.138858.

G. Wallace and R. Duce. Transport of particulate organic matter by bubbles in marine waters. *Limnology and Oceanography*, 23:1155–1167, 1978.

R. Wanninkhof. Relationship between wind speed and gas exchange over the ocean. *J. Geophys. Res.*, 97:7373–7382, 1992. doi: 10.1029/92JC00188.

R. Wanninkhof and W. R. McGillis. A cubic relationship between gas transfer and wind speed. *Geophys. Res. Lett.*, 26:1889–1892, 1999. doi: 10.1029/1999GL900363.

R. Wanninkhof, W. E. Asher, D. T. Ho, C. Sweeney, and W. R. McGillis. Advances in quantifying air-sea gas exchange and environmental forcing. *Annu. Rev. Marine Sci.*, 1:213–244, 2009. doi: 10.1146/annurev.marine.010908.163742.

J. W. Wright and W. C. Keller. Doppler spectra in microwave scattering from wind waves. *The Physics of Fluids*, 14:466–474, 1971.

J. Wu. Slope and curvature distribution of wind-disturbed water surface. *Journal of the Optical Society of America*, 61:852–858, July 1971.

J. Wu. Directional slope and curvature distribution of wind waves. *J. Fluid Mech.*, 79:463–480, 1977.

O. Wurl, E. Wurl, L. Miller, L. Johnson, and S. Vagle. Formation and global distribution of sea-surface microlayers. *Biogeosciences*, 8:121–135, 2011.

V. Zakharov and N. Filonenko. Weak turbulence of capillary waves. *Journal of Applied Mechanics and Technical Physics*, 8(5):37–40, 1967.

C. Zappa, M. Banner, H. Schultz, A. Corrada-Emmanuel, L. Wolff, and J. Yalcin. Retrieval of short ocean wave slope using polarimetric imaging. *Meas. Sci. Technol.*, 19:055503 (13pp), 2008. doi: 10.1088/0957-0233/19/5/055503.

C. J. Zappa, W. E. Asher, and A. T. Jessup. Microscale wave breaking and air-water gas transfer. *J. Geophys. Res.*, 106(C5):9385–9391, 2001. doi: 10.1029/2000JC000262.

C. J. Zappa, W. E. Asher, A. T. Jessup, J. Klinke, and S. R. Long. Microbreaking and the enhancement of air-water transfer velocity. *J. Geophys. Res.*, 109:C08S16, 2004. doi: 10.1029/2003JC001897.

C. J. Zappa, W. R. McGillis, P. A. Raymond, J. B. Edson, E. J. Hintsa, H. J. Zemmelink, J. W. H. Dacey, and D. T. Ho. Environmental turbulent mixing controls on the air-water gas exchange in marine and aquatic systems. *Geophys. Res. Lett.*, 34: L10601, 2007. doi: 10.1029/2006GL028790.

C. J. Zappa, M. L. Banner, H. Schultz, J. Gemmrich, R. P. Morison, D. LeBel, and T. Dickey. An overview of sea state conditions and air-sea fluxes during RaDyO. *J. Geophys. Res.*, 117:C00H19, 2012. doi: 10.1029/2011JC007336.

X. Zhang. Capillary-gravity and capillary waves generated in a wind wave tank: Observations and theories. *J. Fluid Mech.*, 189:51–82, 1995.

X. Zhang and C. S. Cox. Measuring the two-dimensional structure of a wavy water surface optically: A surface gradient detector. *Exp. Fluids*, 17:225–237, Aug. 1994. doi: 10.1007/BF00203041.

J. Zhou, K. Mopper, and U. Passow. The role of surface-active carbohydrates in the formation of transparent exopolymer particles by bubble adsorption of seawater. *Limnology and Oceanography*, 43(8):1860–1871, 1998.

B. Ćosović and V. Vojvodić. Voltammetric Analysis of Surface Active Substances in Natural Seawater. *Electroanalysis*, 10(6):429–434, 1998. ISSN 1521-4109. doi: 10.1002/(SICI)1521-4109(199805)10:6<429::AID-ELAN429>3.0.CO;2-7.

Part IV.

Appendix

A

Appendix

A.1 Wind speeds for the Aeolotron campaign 2013

In this section, the reference wind speed curves for the 2013 Aeolotron campaign are depicted.

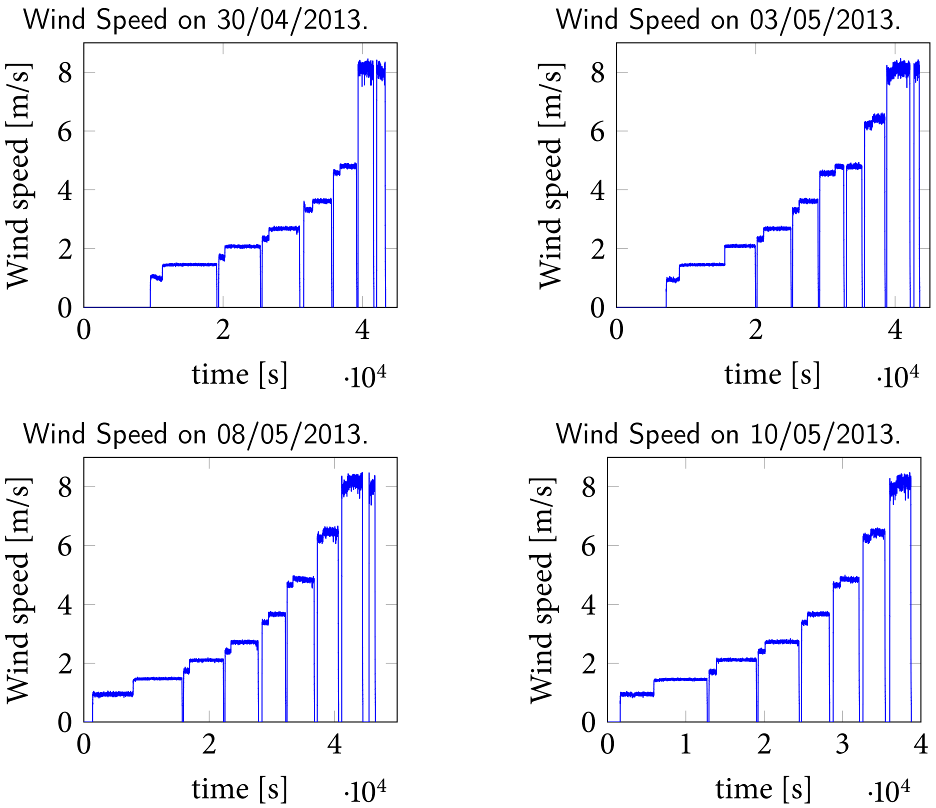

Figure A.1.: Wind speed on the different days of the Aeolotron campaign 2013.

A.2 Datasets

In this section, the entire dataset for mean square slope, transfer velocities and friction velocities for the 2013 Aeolotron campaign (section 6.1) and for the 2011 Aeolotron campaign is presented. f denotes the frequency at the wind generator, σ^2 is mean square slope. k_{600} is the gas transfer velocity for nitrous oxide (N_2O) scaled to that of CO_2 at 20 °C in fresh water as calculated by Krall [2013]; Krall et al. [2014]. Friction velocities were provided by Bopp and Jähne [2014]. Mean square slope data for the 2011 dataset is taken from Kiefhaber [2014]. Values marked by NaN are not available. Quantities preceded by Δ give the measurement error.

Table A.1.: Dataset for the 2013 Aeolotron campaign.

f	date	Surfactant	u_{ref}	$u_{\star,\text{water}}$	$\Delta u_{\star,\text{water}}$	k_{600}	Δk_{600}	σ^2	$\Delta\sigma^2$
[Hz]			[m/s]	[cm/s]	[cm/s]	[cm/h]	[cm/h]	[-]	[-]
5	30/04	1 mg/l Dextran	1,48	0,196	0,009	1,269	0,06345	0,0053	0,0015
7			2,20	0,195	0,009	2,066	0,1033	0,0102	0,0035
9			2,89	0,410	0,023	3,065	0,15325	0,0122	0,0043
12			3,88	0,547	0,034	5,134	0,2567	0,0147	0,0059
16			5,11	0,754	0,053	11,149	0,55745	0,0406	0,0126
22			6,77	1,197	0,094	25,607	1,28035	0,0815	0,0197
29			8,42	1,751	0,166	40,914	2,0457	0,1211	0,0263
5	03/05	1 mg/l Dextran	1,48	0,214	0,0112	1,557	0,07785	0,0059	0,0007
7			2,20	0,325	0,016	2,598	0,1299	0,012	0,0037
9			2,89	0,429	0,024	4,558	0,2279	0,0153	0,0052
12			3,88	0,557	0,035	7,945	0,39725	0,023	0,0087
16			5,11	0,759	0,053	15,528	0,7764	0,0524	0,0136
22			6,77	1,213	0,095	30,666	1,5333	0,0869	0,0216
29			8,42	1,777	0,168	47,024	2,3512	0,1262	0,0277
5	08/05	Full mix	1,48	NaN	NaN	0,657	0,03285	0,0017	0,0002
7			2,20	NaN	NaN	0,949	0,04745	0,0017	0,0001
9			2,89	0,313	0,016	1,515	0,07575	0,0017	0
12			3,88	0,424	0,024	2,2	0,11	0,0021	0,0008
16			5,11	0,719	0,049	5,709	0,28545	0,0166	0,01
16			5,11	0,719	0,049	7,094	0,3547	0,023	0,01
16			5,11	0,719	0,049	7,98	0,399	0,0276	0,01
16			5,11	0,719	0,049	8,637	0,43185	NaN	NaN
22			6,77	1,177	0,091	25,408	1,2704	0,0782	0,0202
29			8,42	1,742	0,164	42,128	2,1064	0,117	0,0268
5	10/05	Full mix	1,48	0,158	0,010	0,71	0,0355	0,0018	0
7			2,20	0,233	0,011	1,063	0,05315	0,0018	0
9			2,89	0,327	0,017	1,569	0,07845	0,0018	0
12			3,88	0,439	0,026	2,171	0,10855	0,0021	0,0007
16			5,11	0,706	0,048	5,921	0,29605	0,0183	0,01
16			5,11	0,706	0,048	6,973	0,34865	0,0233	0,01
16			5,11	0,706	0,048	7,398	0,3699	0,0265	0,01
16			5,11	0,706	0,048	7,746	0,3873	0,029	0,0141
22			6,77	1,189	0,093	26,059	1,30295	0,0832	0,0204
29			8,42	1,745	0,165	42,089	2,10445	0,1211	0,0274

Table A.2.: Dataset for the 2011 Aeolotron campaign.

f	date	Surfactant	u_{ref}	$u_{\star,\mathrm{water}}$	$\Delta u_{\star,\mathrm{water}}$	k_{600}	Δk_{600}	σ^2	$\Delta\sigma^2$
[Hz]			[m/s]	[cm/s]	[cm/s]	[cm/h]	[cm/h]	[-]	[-]
3	01/03	clean water	0,7333	0,11	NaN	0,598	0,028	0,0024	NaN
5			1,414	0,15	NaN	2,648	0,124	0,0073	NaN
7			2,056	0,24	NaN	3,922	0,186	0,0127	NaN
9			2,691	0,34	NaN	6,153	0,298	0,0163	NaN
12			3,619	0,52	NaN	9,419	0,466	0,0246	NaN
16			4,795	0,82	NaN	15,805	0,816	0,046	NaN
22			6,466	1,38	NaN	33,850	1,927	0,0782	NaN
29			8,251	2,14	NaN	53,262	3,871	0,1136	NaN
3	03/03	0.6 g Triton X-100	0,8	0,11	NaN	0,500	0,024	0,002	NaN
5			1,46	0,17	NaN	0,731	0,035	0,0019	NaN
7			2,091	0,25	NaN	1,096	0,053	0,0019	NaN
9			2,717	0,35	NaN	2,110	0,103	0,0076	NaN
12			3,65	0,53	NaN	3,205	0,157	0,0101	NaN
16			4,851	0,84	NaN	7,070	0,352	0,0205	NaN
22			6,502	1,39	NaN	24,042	1,274	0,0738	NaN
29			8,288	2,15	NaN	44,061	2,713	0,1144	NaN
5	08/03	3.0 g Triton X-100	1,463	NaN	NaN	0,738	0,037	0,0019	NaN
7			2,075	0,15	0,02	1,100	0,055	0,0019	NaN
9			2,695	0,28	0,03	1,618	0,082	0,0018	NaN
12			3,675	0,45	0,03	2,207	0,113	0,0018	NaN
16			4,927	0,66	0,02	2,995	0,156	0,0018	NaN
22			6,625	1,06	0,09	11,275	0,618	0,0351	NaN
29			8,372	1,72	0,24	31,019	1,962	0,1013	NaN
5			1,438	NaN	NaN	0,756	0,036	0,0017	NaN
7	10/03	3.0 g Triton X-100	2,074	0,15	0,02	1,139	0,055	0,0017	NaN
9			2,718	0,28	0,03	1,655	0,080	0,0017	NaN
12			3,659	0,45	0,03	2,582	0,126	0,0045	NaN
16			4,898	0,66	0,02	3,829	0,189	0,0065	NaN
22			6,604	1,06	0,09	11,734	0,606	0,0387	NaN
29			8,369	1,72	0,24	33,266	1,958	0,0997	NaN

A.3 Uncorrelated Mean Square Slope Timeseries

In this section, the uncorrelated mean square slope time series as described in section 9.2 are presented. Note the different scaling of the vertical axis. The black line gives mean square slope data, the red line gives a running mean with a window size of 150 s and the orange lines give the standard deviation.

Figure A.2.: Mean Square Slope plotted over time for different values of u_{ref}. Data of 30/04/2013 (1 mg/l Dextran).

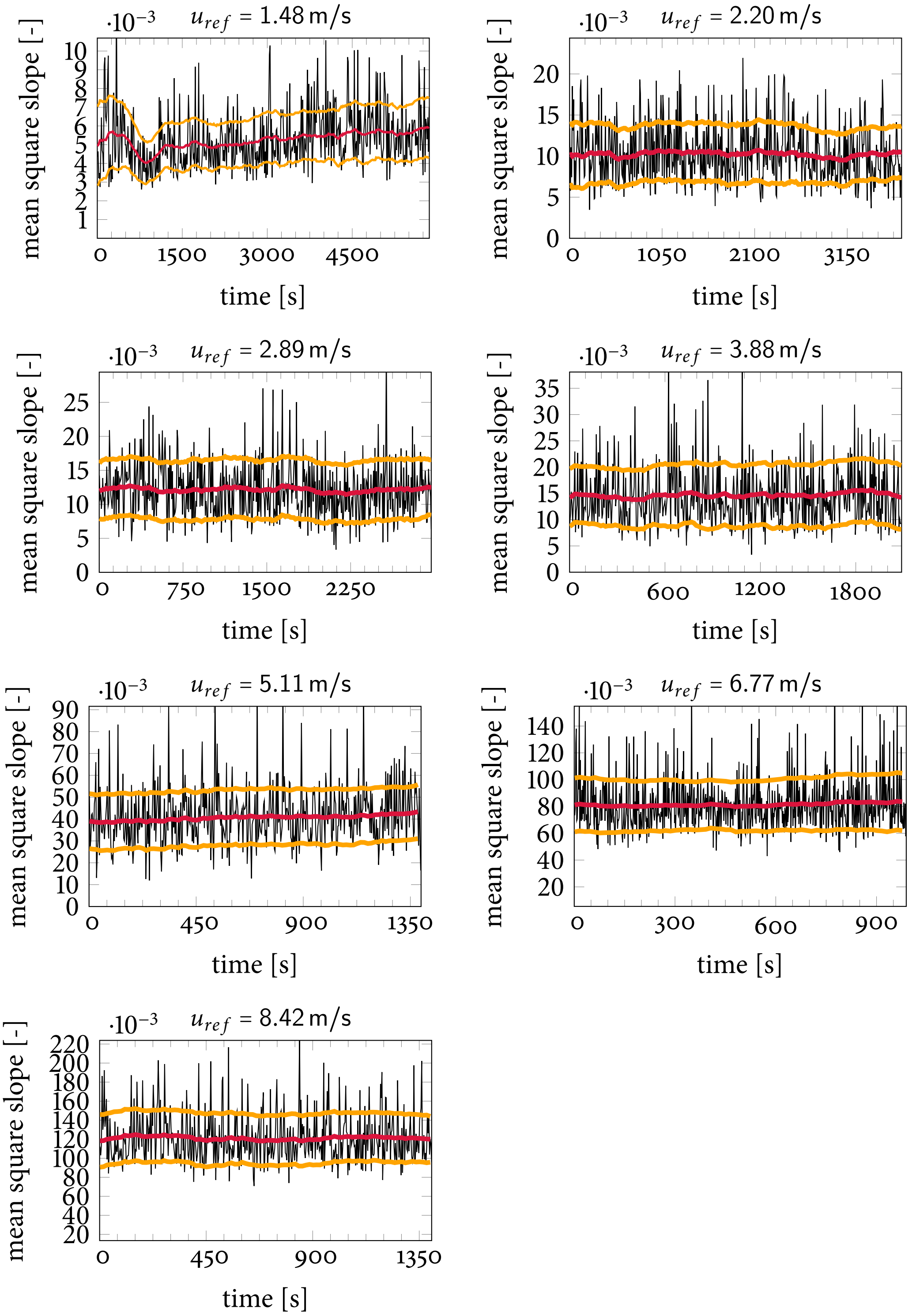

Figure A.4.: Mean Square Slope plotted over time for different values of u_{ref}. Data of 03/05/2013 (2 mg/l Dextran).

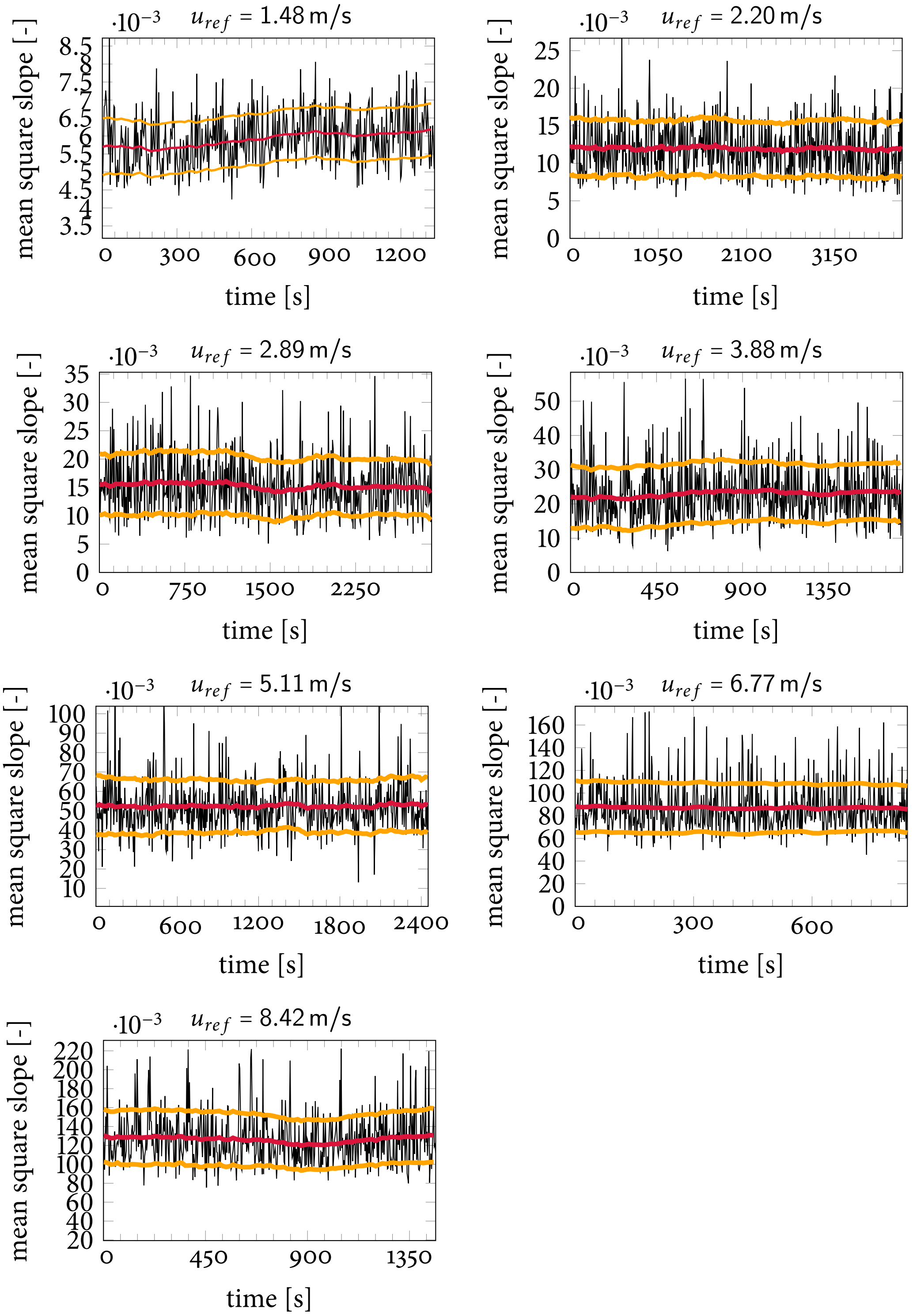

Figure A.6.: Mean Square Slope plotted over time for different values of u_{ref}. Data of 08/05/2013 (full mix).

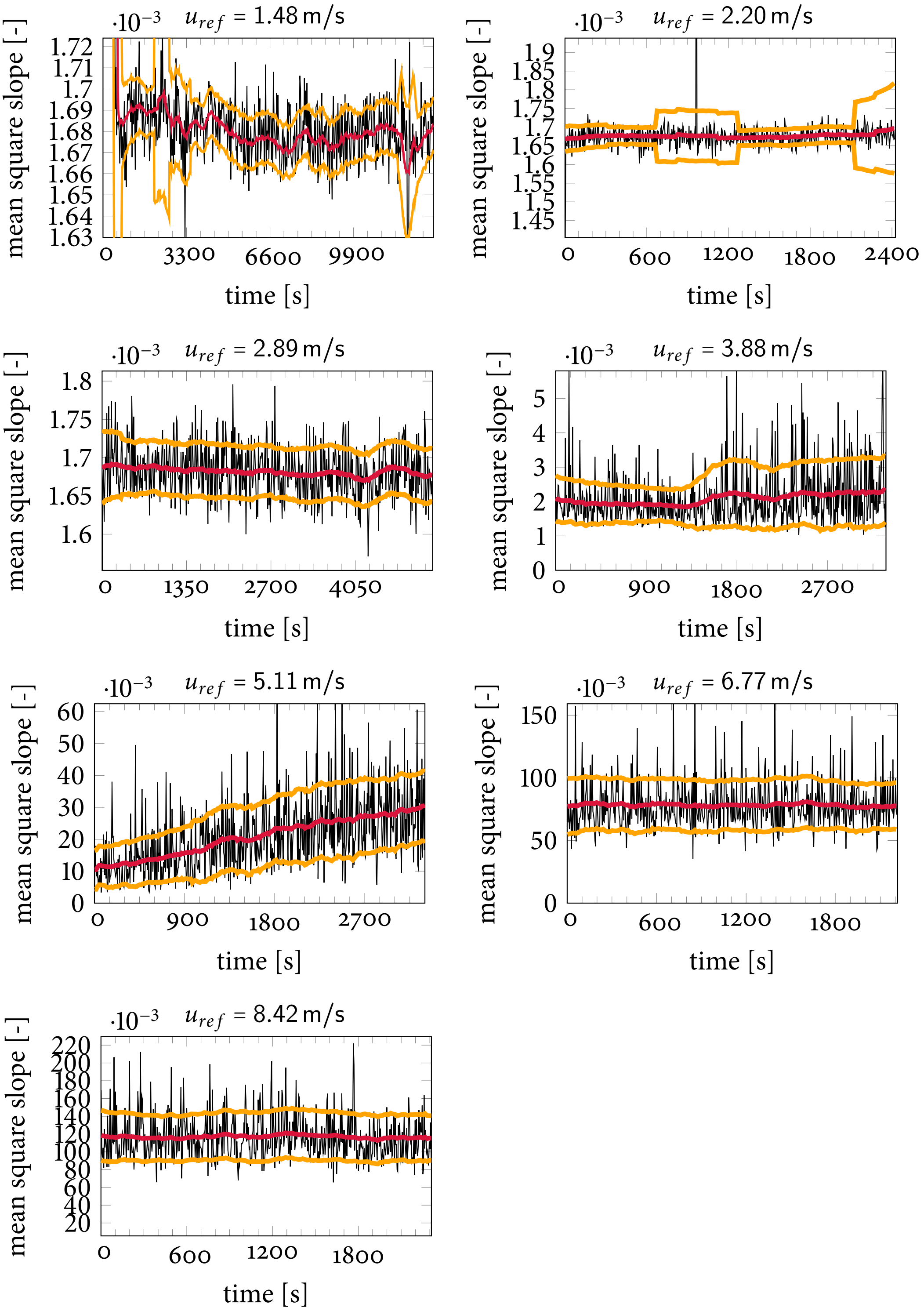

Figure A.8.: Mean Square Slope plotted over time for different values of u_{ref}. Data of 10/05/2013 (full mix).

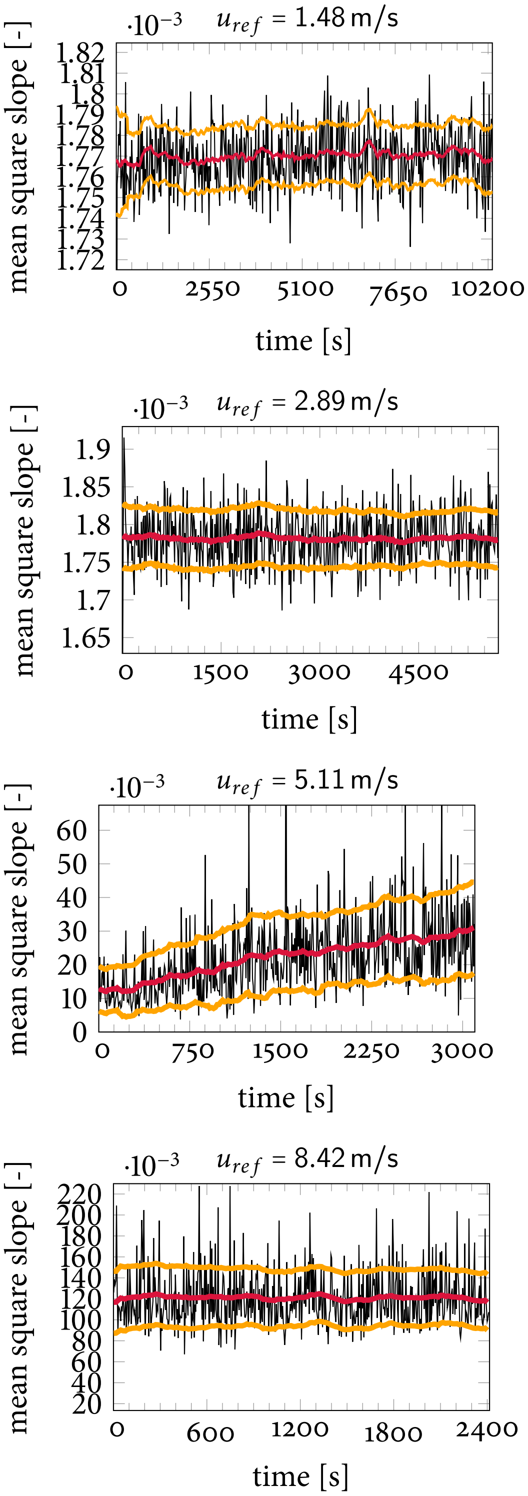

A.4 Correlated Mean Square Slope Timeseries

In this section, the correlated mean square slope time series as described in section 9.2 are presented. Note the different scaling of the vertical axis.

Figure A.10.: Mean Square Slope plotted over time for different values of u_{ref}. Data of 30/04/2013 (1 mg/l Dextran).

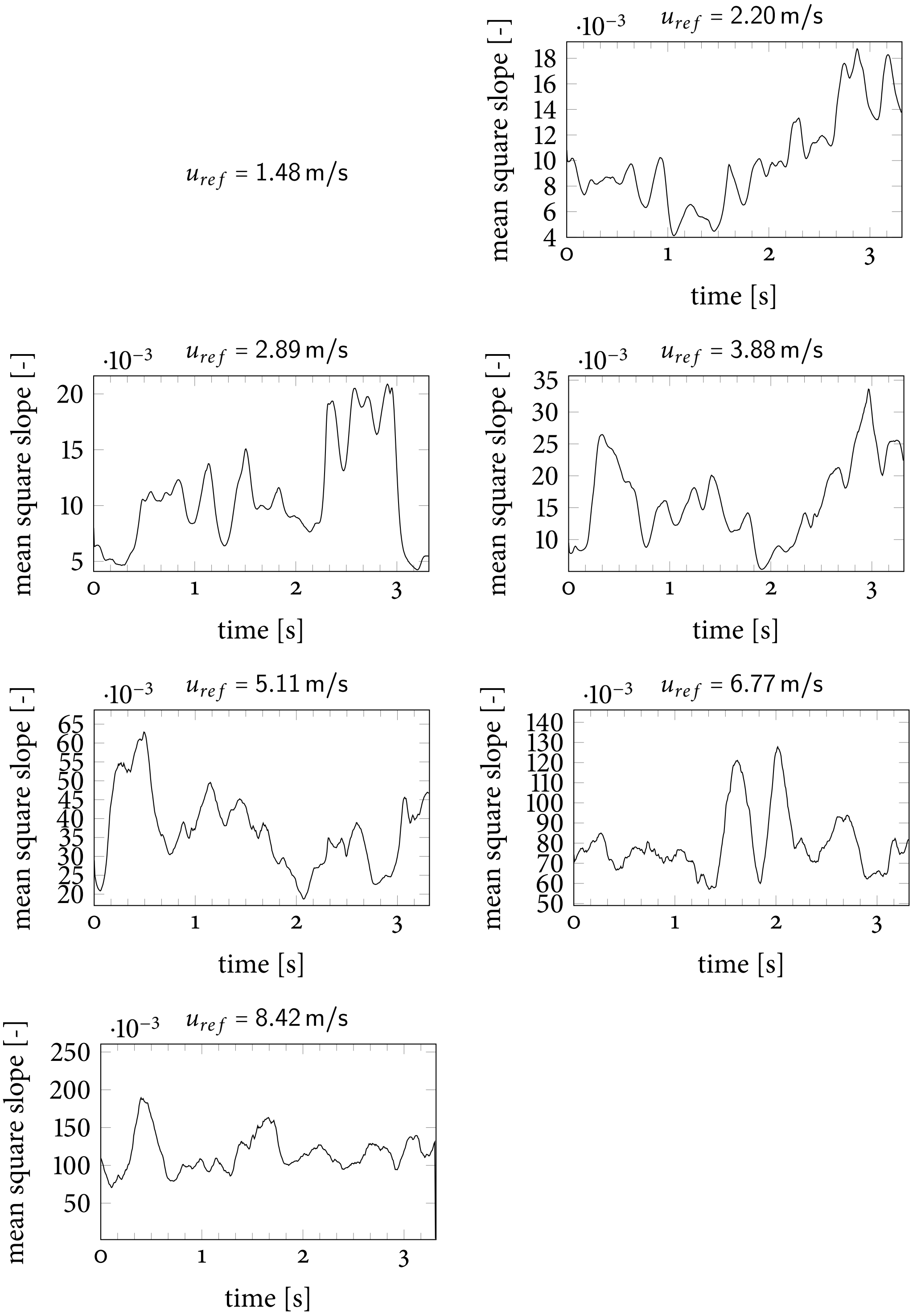

Figure A.12.: Mean Square Slope plotted over time for different values of u_{ref}. Data of 03/05/2013 (2 mg/l Dextran).

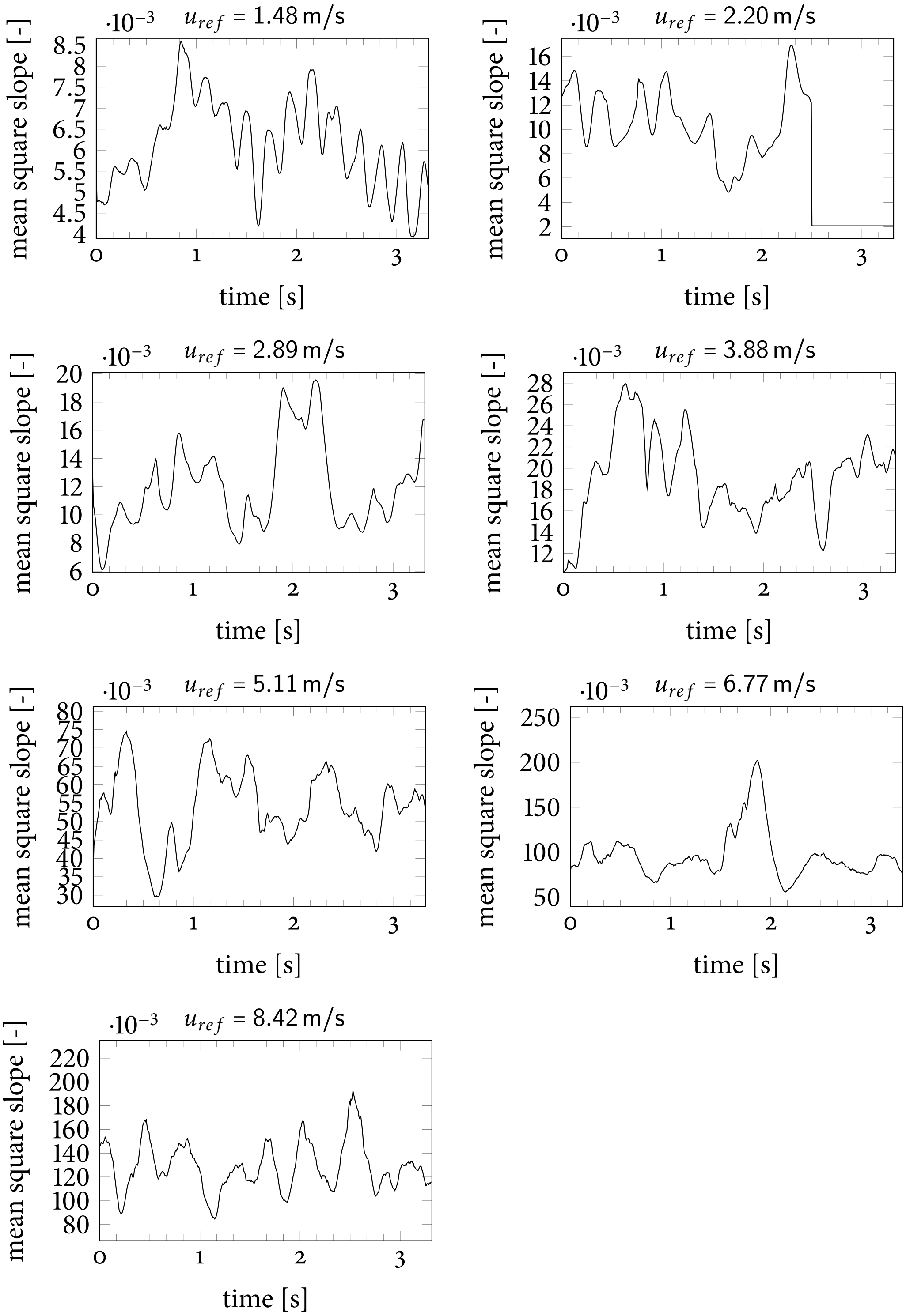

Figure A.14.: Mean Square Slope plotted over time for different values of u_{ref}. Data of 08/05/2013 (full mix).

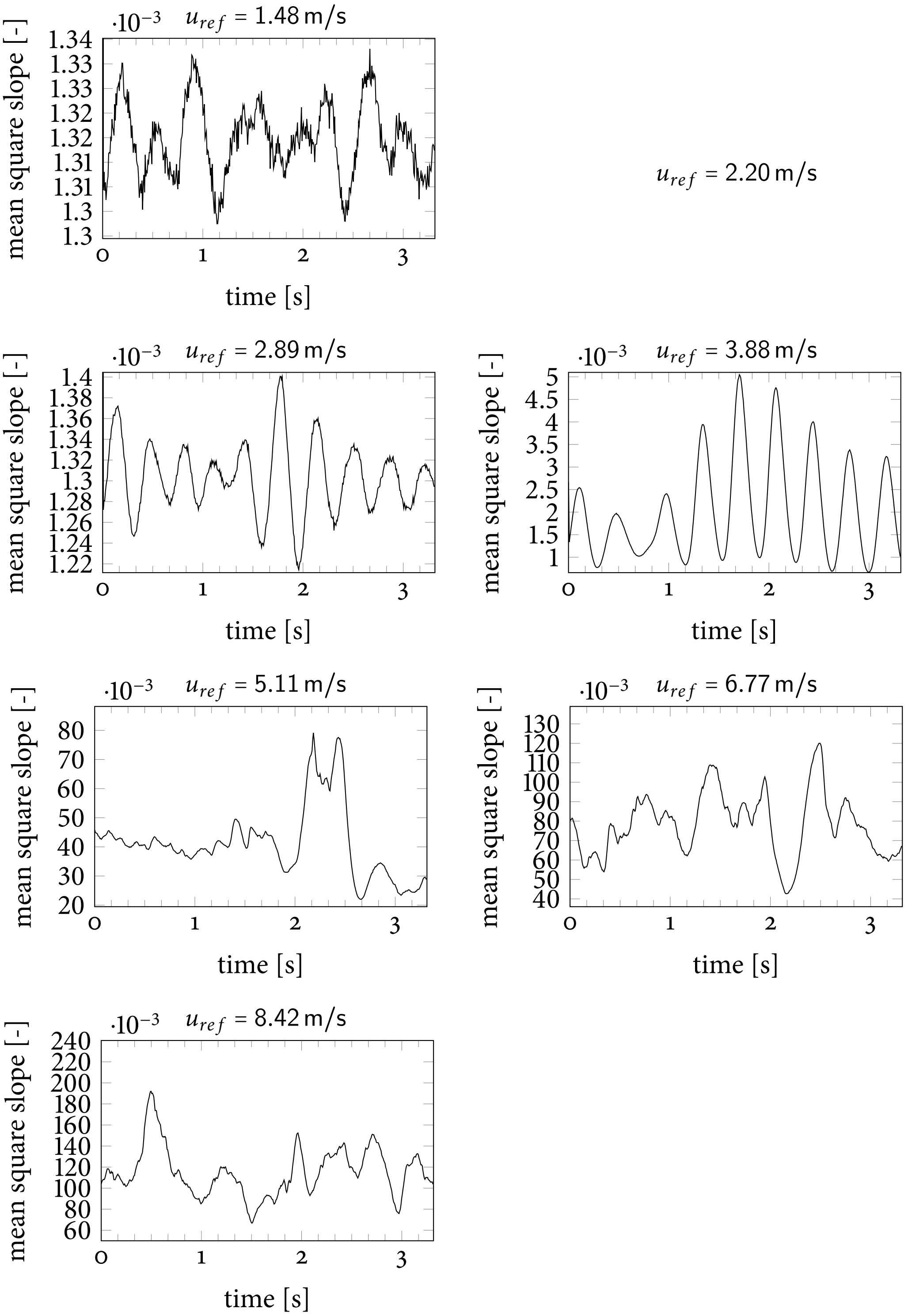

Figure A.16.: Mean Square Slope plotted over time for different values of u_{ref}. Data of 10/05/2013 (full mix).

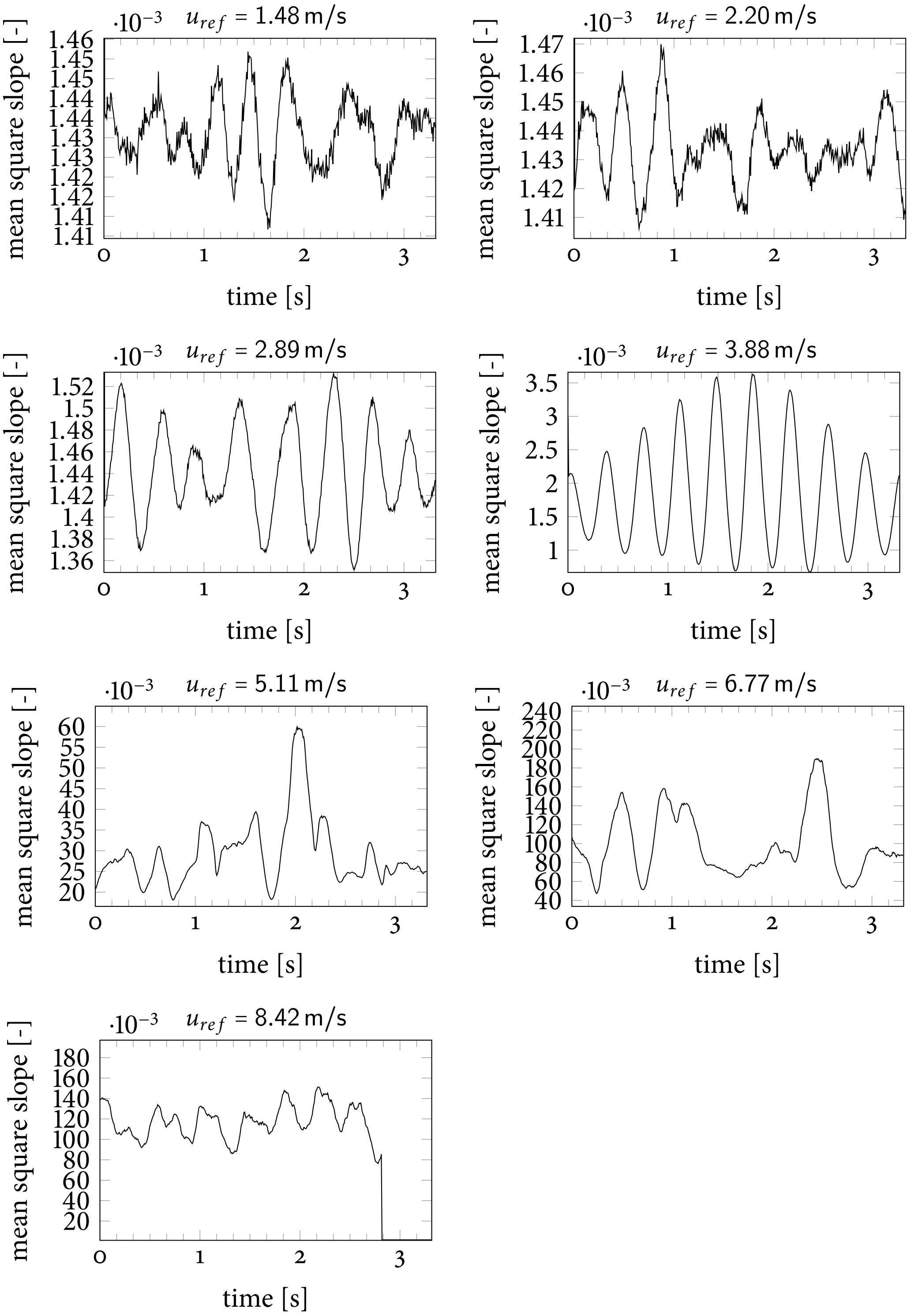

A.5 Omnidirectional Saturation Spectra

In this section, omnidirectional saturation spectra as described in section 9.4 are presented. The color code for the wind speeds is the same as in Figure 9.11.

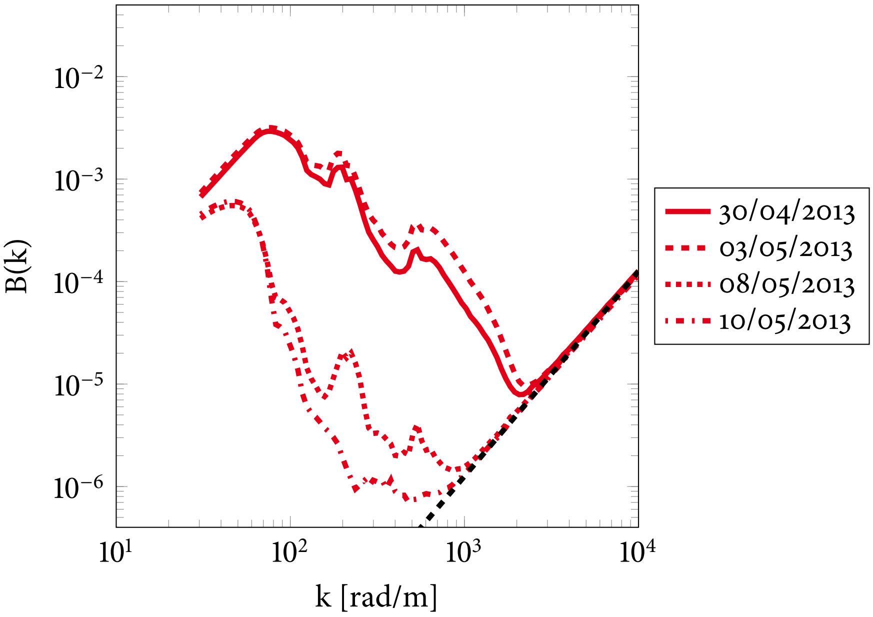

Figure A.18.: Omnidirectional saturation spectra $B(k) = S(k) \cdot k^2$ plotted over k for $u_{ref} = 1.48\,\mathrm{m/s}$

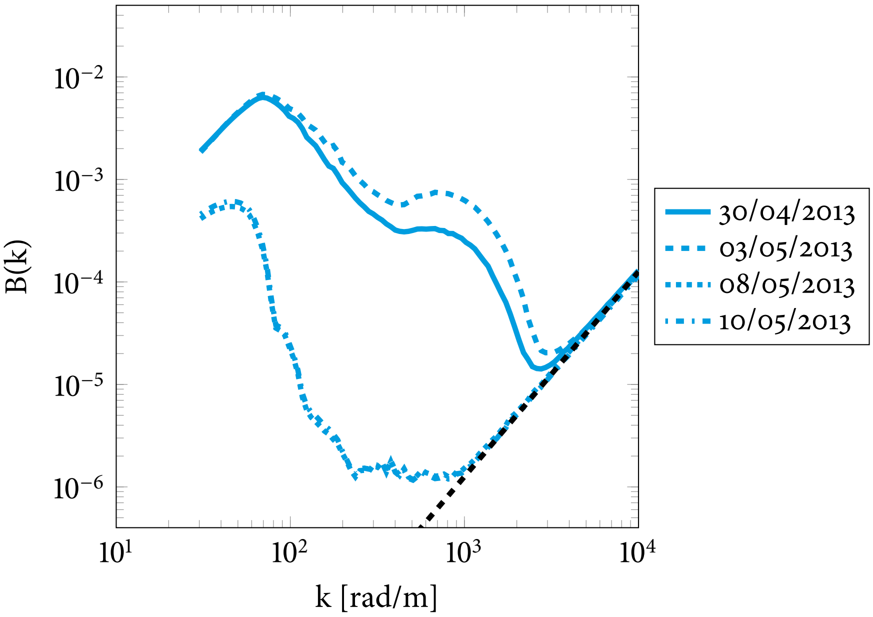

Figure A.19.: Omnidirectional saturation spectra $B(k) = S(k) \cdot k^2$ plotted over k for $u_{ref} = 2.20\,\mathrm{m/s}$

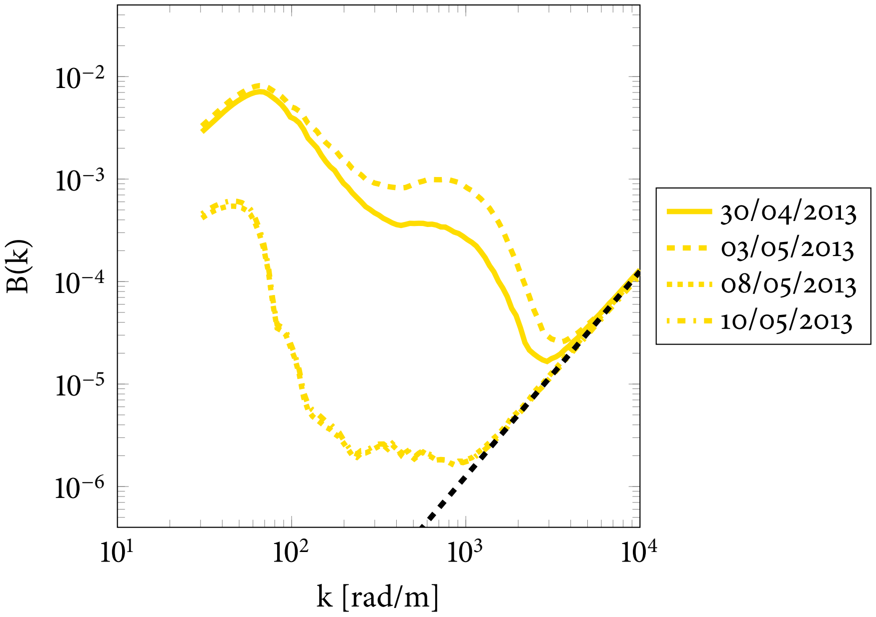

Figure A.20.: Omnidirectional saturation spectra $B(k) = S(k) \cdot k^2$ plotted over k for $u_{ref} = 2.89\,\mathrm{m/s}$

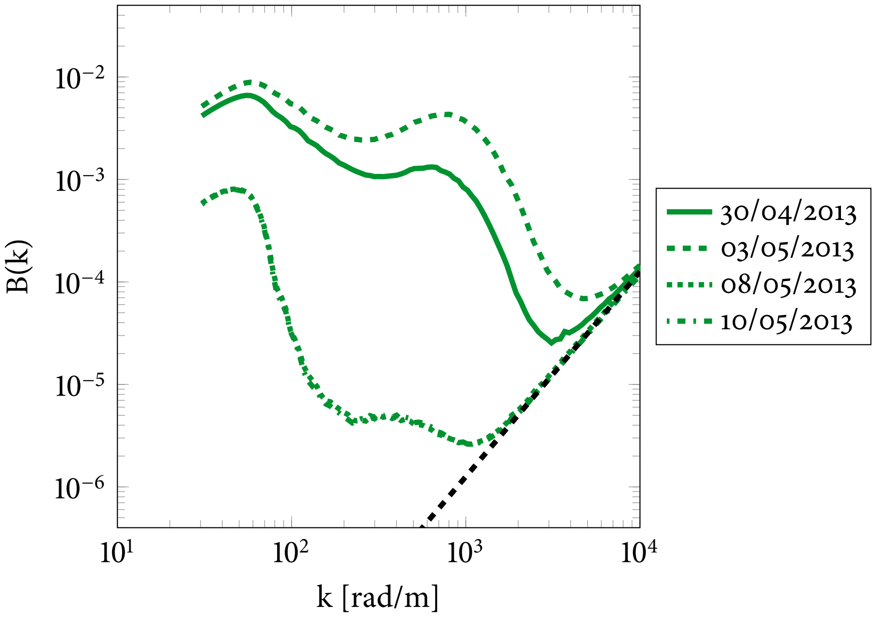

Figure A.21.: Omnidirectional saturation spectra $B(k) = S(k) \cdot k^2$ plotted over k for $u_{ref} = 3.88\,\mathrm{m/s}$

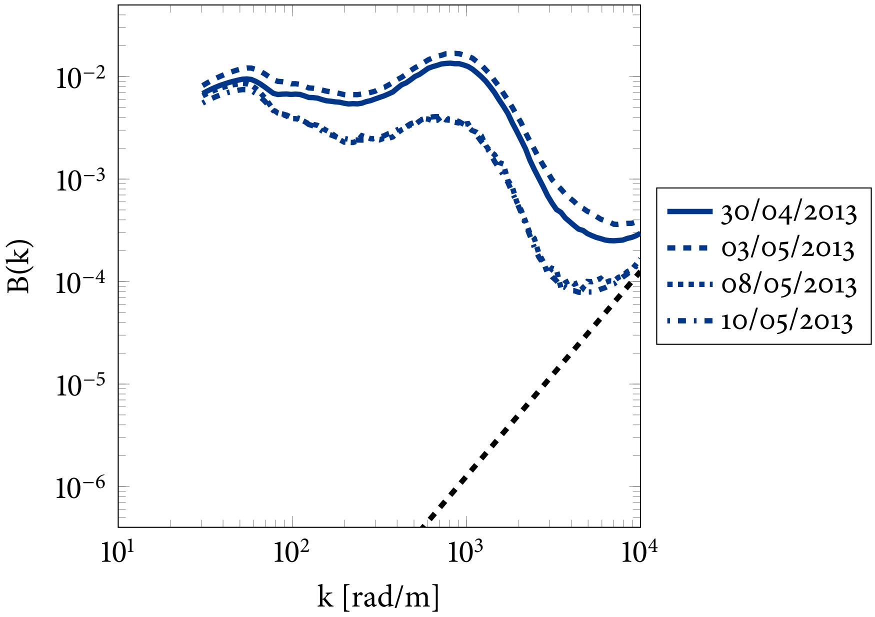

Figure A.22.: Omnidirectional saturation spectra $B(k) = S(k) \cdot k^2$ plotted over k for $u_{ref} = 5.11\,\mathrm{m/s}$

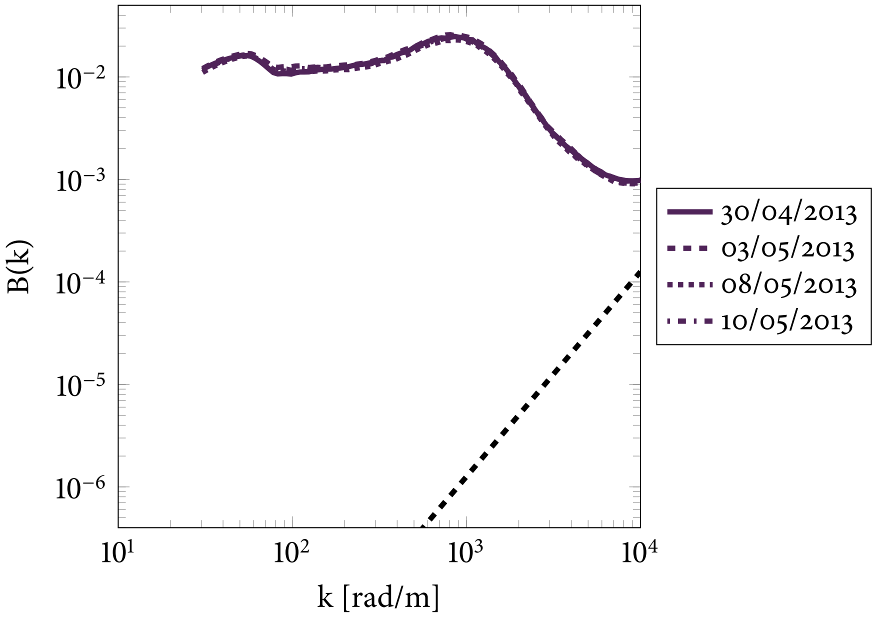

Figure A.23.: Omnidirectional saturation spectra $B(k) = S(k) \cdot k^2$ plotted over k for $u_{ref} = 6.77\,\mathrm{m/s}$

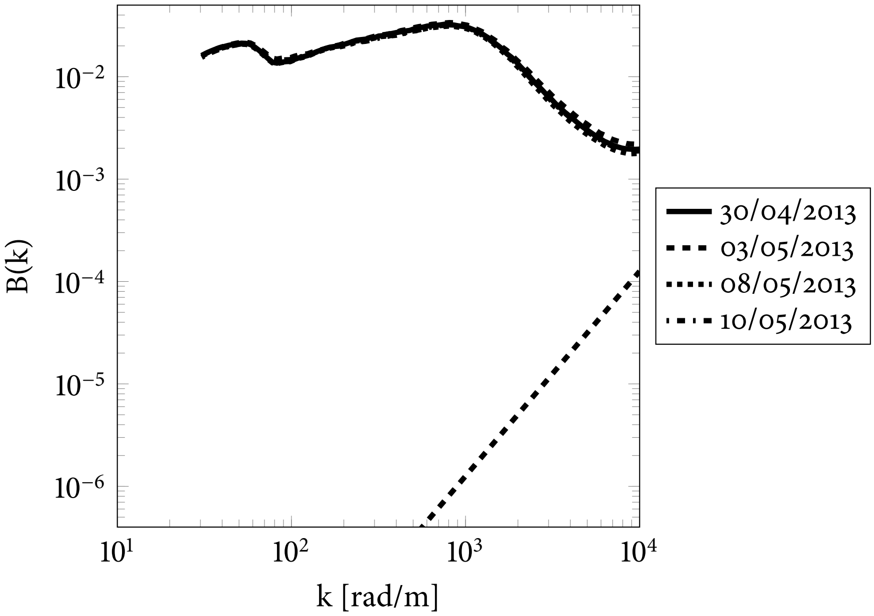

Figure A.24.: Omnidirectional saturation spectra $B(k) = S(k) \cdot k^2$ plotted over k for $u_{ref} = 8.42\,\mathrm{m/s}$

Erklärung:

Ich versichere, dass ich diese Arbeit selbstständig verfasst habe und keine anderen als die angegebenen Quellen und Hilfsmittel benutzt habe.

Heidelberg, den (Datum) ....